

# **DEFECTS AND GROWTH PROCESSES AT IONIC AND OXIDE CRYSTAL SURFACES STUDIED BY ATOMIC FORCE MICROSCOPY**

THÈSE N° 1811 (1998)

PRÉSENTÉE AU DÉPARTEMENT DE PHYSIQUE

ÉCOLE POLYTECHNIQUE FÉDÉRALE DE LAUSANNE

POUR L'OBTENTION DU GRADE DE DOCTEUR ÈS SCIENCES

PAR

**Alexander MENCK**

Diplom-Physiker, Universität Konstanz, Allemagne  
de nationalité allemande

acceptée sur proposition du jury:

Prof. K. Kern, directeur de thèse  
Prof. W. Benoit, rapporteur  
Dr N. Burnham, rapporteur  
Prof. J. Jupille, rapporteur  
Prof. O. Marti, rapporteur

Lausanne, EPFL  
1998

# Version abrégée

Cette thèse présente le développement et l'application de la microscopie à force atomique (AFM) à température variable à l'étude de défauts cristallins ainsi qu'à la croissance de métaux sur des surfaces des cristaux ioniques et d'oxydes cristallins. L'influence de la contrainte sur la création de défauts à la surface d'un cristal de bromure de potassium (KBr) a été examinée par l'AFM à l'air. Les surfaces clivées faces (100) présentent de larges terrasses (100 nm à 1  $\mu$ m) sans défauts, séparées par des marches monoatomiques. Par application d'une contrainte compressive, la structure de cette surface change dramatiquement. Un nombre croissant de marches apparaît perpendiculairement à la direction de la contrainte appliquée. Sous contraintes très élevées, l'apparition de marches parallèles à cette direction est aussi observée. Ce phénomène est attribué au mouvement (est probablement à la création) de dislocations de volume. Ces défauts glissent sur les plans {110} et créent des marches à la surface. On en déduit, que la densité des dislocations dans le volume et la contrainte appliquée déterminent la densité des marches à la surface.

La surface de l'oxyde de magnésium clivé à l'air présente, contrairement au KBr, une surface contaminée, ainsi qu'on peut le voir par microscopie à force atomique dans l'ultra haut vide. La densité de marches est plus grande que celle du KBr sans application de contrainte. La largeur des terrasses est typiquement comprise entre 20 nm et 100 nm. Cette densité étant due au clivage (la contrainte requise et la densité de dislocations sont probablement plus grande comparé au KBr), il est impossible de réduire le nombre de marches.

Les contaminants (essentiellement du carbone) ont été efficacement enlevés grâce à un traitement combiné de clivage sous atmosphère protectrice d'argon et de recuit sous pression partielle élevée d'oxygène dans l'ultra haut vide. De telles surfaces sont propres et conviennent parfaitement pour la déposition de métaux. Les premières études systématiques de la croissance de moins d'une monocouche de métal sur une surface isolante ont été réalisées

par microscopie à force atomique.

La croissance à trois dimensions d'îlots de palladium a été observée dans la gamme de température de 300 K à 750 K. La gamme de 300 K à 570 K est particulièrement intéressante, car la nucléation des îlots se produit aux défauts, ce qui se manifeste par un plateau dans le diagramme du logarithme de la densité d'îlots ( $\ln n_x$ ) en fonction de  $1/T$ . On peut donc en déduire une densité de  $6 \times 10^{12}$  defects/cm<sup>2</sup> pour une surface de MgO clivé sous atmosphère d'argon. A plus haute température, le logarithme de la densité d'îlots ( $\ln n_x$ ) est linéaire en fonction de  $1/T$ . Pourtant, la pente ( $(0.63 \pm 0.05)$  eV) ne peut pas être interprété immédiatement comme étant la barrière de diffusion car les défauts ont une influence non-négligeable. A 800 K, la croissance de palladium sur MgO est montré à deux dimensions avec une contribution croissante de la reévaporation.

La déposition d'argent dans la gamme de température de 300 K à 550 K est complètement différente. On n'observe pas la nucléation aux défauts, par contre une variation linéaire du logarithme de la densité d'îlots ( $n_x$ ) en fonction de  $1/T$  a été observée. L'interprétation de la pente de ce diagramme ( $(83 \pm 7)$  meV) n'est de nouveau pas évidente, car les défauts sont présents autant que pour la croissance de palladium. Pourtant, l'influence des défauts sur la croissance d'argent est beaucoup plus faible comparé au cas du palladium. C'est une indication que l'énergie de adsorption et d'interaction avec les défauts est beaucoup plus faible pour l'argent comparé au palladium provoquant très probablement une mobilité plus grande de l'argent sur la surface de MgO.

Pour les deux métaux, l'interaction avec le substrat est tellement faible, que l'application de la microscopie à force atomique en mode "non-contact" à haute résolution est essentielle pour la mesure de tels clusters déposés.

# Abstract

In this thesis we describe the development and application of variable temperature atomic force microscopy for the investigation of defects and metal deposition on ionic and oxide crystal surfaces.

The influence of strain on defect creation of a potassium bromide crystal was investigated by AFM in air. The cleavage faces ( $(100)$ -surfaces) revealed under ambient conditions large (100 nm to 1  $\mu\text{m}$ ), defect-free terraces, typically separated by monatomic steps. This surface undergoes a drastic change upon the application of a compressive strain. With increasing strain, an increasing number of steps perpendicular to the strain direction appear. At very high strain, steps in strain direction appear, as well. The appearance of these steps can be explained by the movement (and presumably creation) of bulk dislocations. These defects glide on slip planes ( $\{110\}$ ) and create steps at the surface. It is concluded that mostly the density of bulk dislocations and the amount of strain applied to an ionic crystal determines the step density at the surface.

Atomic force microscopy data of the magnesium oxide surface in ultra-high vacuum reveals, in contrast to KBr, a contaminated surface when cleaved in air. The step density is higher directly after the cleavage, typical terrace widths are of the order of 20 -100 nm. As this density originates from the cleavage (a higher stress is required compared to KBr and the initial dislocation density in the bulk may be higher) the number of steps cannot be reduced.

The contaminations (mainly carbon) were effectively removed by a combination of cleavage under argon atmosphere and heating in elevated partial pressure of oxygen in UHV. The thus prepared surfaces were found to be clean and appropriate for metal deposition. With these surfaces, we performed the first systematic study of submonolayer growth of metals on insulators by variable temperature AFM.

Upon palladium deposition in the range of 300 K to 750 K, the growth of three-dimensional islands was observed. Of particular interest is a defect

nucleation regime between 300 K to 570 K, from which a defect density on the MgO, cleaved under argon atmosphere, of  $6 \times 10^{12}$  defects/cm<sup>2</sup> can be deduced. At higher temperatures, an Arrhenius behavior of the logarithm of the island density ( $n_x$ ) versus  $1/T$  is obtained. The slope of this plot is  $(0.63 \pm 0.05)$  eV, the interpretation as a diffusion energy, however, is not straightforward as the defects play a major role in island nucleation. At 800 K, palladium grows in a more two-dimensional fashion but reevaporation becomes increasingly important at such high temperatures.

Silver deposition in the temperature range from 300 K to 550 K revealed a completely different behavior. No defect nucleation was visible by a plateau in the Arrhenius plot instead a linear variation of the island density ( $\ln n_x$ ) with  $1/T$  was obtained. Nevertheless, the slope of this line ( $(83 \pm 7)$  meV) cannot be directly interpreted, because the influence of the defects, which are also present as we know from the palladium deposition, still need clarification in the case of silver. Obviously the behavior of palladium and silver upon deposition on MgO(100) is basically different, with the silver being by far less influenced by the defects present at the surface. These results indicate a smaller adsorption and defect interaction energy for silver on MgO(100) than for palladium and presumably a higher mobility for silver atoms on this surface.

For both of these metals, the interaction with the substrate is weak enough such that the implementation of high-resolution non-contact AFM is crucial for successfully imaging such deposits.

# Contents

<b>1</b>	<b>Introduction</b>	<b>1</b>
<b>2</b>	<b>Atomic Force Microscopy</b>	<b>5</b>
2.1	Forces in Atomic Force Microscopy . . . . .	5
2.1.1	Short range forces . . . . .	5
2.1.2	Van der Waals forces . . . . .	6
2.1.3	Long range electrostatic forces . . . . .	7
2.1.4	Capillary forces . . . . .	8
2.2	The atomic force microscope . . . . .	9
2.2.1	Laser beam deflection (LBD) detection technique . . .	10
2.2.2	Piezoresistive detection . . . . .	13
2.2.3	Modes of operation . . . . .	15
<b>3</b>	<b>Experimental</b>	<b>23</b>
3.1	The LBD beetle-type AFM . . . . .	24
3.1.1	The AFM Head . . . . .	24
3.1.2	Electronics . . . . .	28
3.1.3	Mechanical Stability . . . . .	28
3.1.4	Performance . . . . .	31
3.2	The UHV-AFM experimental setup . . . . .	31
3.2.1	The AFM-FTIR ultrahigh vacuum chamber . . . . .	33
3.2.2	The VT-AFM . . . . .	38
<b>4</b>	<b>Observation of slip steps on the KBr(100) surface</b>	<b>47</b>
4.1	Dislocations . . . . .	47
4.2	Observation of dislocations . . . . .	54
<b>5</b>	<b>The MgO(100) surface</b>	<b>61</b>
5.1	Characterization of MgO(100) . . . . .	61
5.2	Preparation of the MgO(100)-surface . . . . .	66
5.3	Charge phenomena on MgO(100) . . . . .	69

<b>6</b>	<b>Metal nucleation and growth on MgO(100)</b>	<b>73</b>
6.1	Metal growth on metaloxides . . . . .	73
6.2	Nucleation theory . . . . .	77
6.3	Palladium nucleation and growth . . . . .	82
6.4	Silver nucleation and growth . . . . .	92
<b>7</b>	<b>Outlook</b>	<b>97</b>
	<b>References</b>	<b>99</b>
	<b>Curriculum vitae</b>	<b>107</b>
	<b>Remerciements</b>	<b>109</b>

# Remerciements

Un grand merci à tous les membres de l'institut de physique expérimentale pour la bonne atmosphère de notre institut dans laquelle j'ai eu l'opportunité de réaliser ce travail de doctorat. En particulier, j'aimerais remercier tout ceux, qui ont contribué à l'élaboration de ce projet:

- le professeur Klaus Kern, qui m'a donné l'opportunité de effectuer ce travail dans son groupe pour son soutien pendant toute cette periode.

- les différents assistants et post-docs: avec Harri Brune j'ai souvent eu l'occasion de discuter les plans de construction et les problèmes techniques qui arrivent au cours d'un tel projet. Pendant les dernières jours de rédaction ses conseils ont été particulièrement précieux. Johannes Barth s'est chargé de relire le manuscrit et a grandement contribué à améliorer sa qualité. Elisabeth Kampshoff avec son bonne humeur (presque) constante, a créé une atmosphère amicale au labo et a participé activement au montage de l'appareil. Ensuite, Johannes Trost et Günter Haas ont beaucoup contribué à la mise au point de l'expérience. Je souhaite plein succès à Günter, qui a pris la relève.

Je tiens aussi à remercier l'équipe de l'atelier qui a contribué très fortement au succès du projet. Un merci particulier à Philippe Zurcher qui a fait la plupart des pièces et à André Guisolan, pour son engagement et sa disponibilité tout au long du projet.

Je voudrais aussi remercier Claire-Lise Bandelier qui a réalisé un grand nombre des figures de ce manuscrit.

Finalement, j'aimerais remercier tout ceux qui ont créé une ambiance agréable et amicale, pas seulement au labo mais aussi dans la vie quotidienne. En particulier, j'aimerais mentionner Ornella Cavalleri et Andreas Hirstein mes collègues de bureau.





# Chapter 1

## Introduction

The demand for effective and inexpensive catalysts is high, not only for environmental reasons, e.g. in the automotive industry, but also for industrial processes. Mainly d metals are catalytically active; the hydrogen and carbon monoxide oxidation over metals of the platinum group are perhaps the most famous example of such a catalytic process. To expose these metals in small quantities most effectively to the reactants, usually finely dispersed metal particles on a support with an extremely high surface to volume ratio are used. Frequently, it is the combination of support and metal, which enhances the catalytic activity, and the responsible processes for the catalytic activity remain to be clarified. Size effects are supposed to play a major role as well as electronic interaction between support and deposit and often defects are important in the catalytic activity [1-3].

Therefore, it is of great interest to obtain better insight into the structure and defect properties of support surfaces like metaloxides ( $\text{MgO}$ ,  $\text{Al}_2\text{O}_3$ ,  $\text{SiO}_2$  ... ) and unveil the resulting morphology of small, finely dispersed metal particles. The knowledge about the basic laws, which govern these processes, will contribute to a better understanding of catalytic activity in general and will open the way towards a controlled tailoring of novel catalysts [4].

There are different approaches to this task. Real catalysts are taken and examined under idealized conditions for their activity and to characterize their properties. From a surface science point of view these methods, however, include too many parameters which complicates the identification of the most important elementary processes. On the other hand, the systems can be simplified to examine single crystal surfaces of the catalytically active material and study adsorption of reactants. This has been done e.g. for the Cu/Pd system [5] as a model for a bimetallic catalyst, which revealed information on the microscopic structure and the associated CO adsorption

phenomena. In this approach, however, the experimental situation is quite far away from real catalysis conditions.

The objective of this thesis is the tailoring and characterization of model catalysts, that are realistic. These model catalysts have to be accessible with standard surface science techniques. The development of the atomic force microscope (AFM) [6] enables us to utilize the typical non-conducting metaloxide supports used in catalysis, because it is the ideal tool for high resolution microscopy on insulating substrates. The model systems are (single crystal) metaloxide substrates with a (submonolayer) deposit of finely dispersed precious metals.

Growth of metals on insulating substrates is less studied than metal-on-metal epitaxy, because many surface science techniques utilize electrons and hence charge an insulating substrate. To overcome this problem, a combined variable temperature AFM and fourier transform infrared spectroscopy (FTIR) setup has been designed. These methods offer access to complementary aspects: the AFM provides structural information on the nanometer scale and the FTIR integral chemical information. Both techniques are applicable to insulating surfaces and furthermore offer the possibility to work in an elevated pressure range (mbar), which allows the study of chemical reactions under realistic conditions. As a wide variety of growth structures on a surface are not accessible at room temperatures, a variable temperature setup similar to now widely used scanning tunneling microscopes was designed [7, 8].

From the beginning, atomic force microscopy initiated extensive research due to its capability to visualize non-conducting surfaces at an atomic scale and the possibility to measure various forces with sub-nanonewton precision [9]. However, it was soon obvious, that an impact in basic surface science research comparable to STM is more difficult to obtain due to a slightly lower resolution capability and the sometimes perturbing character of the measurement. Nevertheless, the AFM became the more important tool in process control and other industrial tasks, because it opened access to technological important insulating surfaces like oxidized silicon in the semiconductor industry. For the most sophisticated lithographic techniques which made possible structures down to  $0.18\text{ }\mu\text{m}$  the AFM is the ideal imaging tool beyond optical microscopy.

The development of the non-contact mode in AFM offered a better access to delicate samples due to the drastically reduced tip-sample interaction and real atomic resolution in AFM [10]. The recent piezolever technique enables easier use in UHV conditions. We employed this technique for the design of a

variable temperature AFM, which now offers measurements in a temperature range from 100 K to 500 K.

In chapter 2 of this thesis, atomic force microscopy is described. Included is a discussion of the forces between an AFM tip and a surface, their measurement and what limits have to be respected. Both of the operational modes used in this thesis, contact mode operation, and in more detail, non-contact mode operation are explained.

In chapter 3 the experimental setups that have been used are described. The beetle-type AFM we designed employed the laser beam deflection detection technique. From its operation in air we obtained valuable information for the design of the UHV-AFM, which is equipped with the piezolever technique. The entire UHV system containing the AFM and the FTIR setup is introduced.

In chapter 4 an experiment concerning the surface modification of the ionic crystal potassium bromide (KBr), subjected to an external compressive stress is presented. Dislocation movement with an appearance of slip steps at the surface was found as a stress relief mechanism.

Chapter 5 comprises the preparation technique we applied for the (100)-cleavage faces of magnesium oxide (MgO). In contrast to the KBr(100) surface, MgO(100) is highly reactive under ambient conditions. A suitable preparation technique in ultrahigh vacuum is presented and the surface quality verified by AFM and Auger electron spectroscopy.

Finally, chapter 6 presents the results obtained for palladium and silver growth on the (100)-surface of MgO in the submonolayer range. The study of the influence of substrate temperature and the deposition flux reveals important differences between these metals, which are associated with their respective adsorption energies and their behavior in the presence of defects on the surface. The influence of the defects is discussed and how the results can be reconciled with nucleation theory is examined.



# Chapter 2

## Atomic Force Microscopy

In this chapter, general considerations concerning atomic force microscopy (AFM) will be given. The different forces playing a role will be addressed followed by a description of how measurements of such small forces are technically realized. The two most established imaging modes in atomic force microscopy, contact and non-contact mode, will be described in some detail.

### 2.1 Forces in Atomic Force Microscopy

Depending on the type of sample and the environment, different forces acting between the sample and the AFM tip have to be taken into account. Generally long-range attractive van der Waals forces and short-range forces due to an overlap of electronic wavefunctions and electrostatic repulsion of ions at a very short distance of tip and sample are present. If the surface or the tip is charged or local charges are present, long-range electrostatic forces play an important role. In an ambient environment capillary forces due to adsorbed water may become even a dominating force contribution.

#### 2.1.1 Short range forces

Short range forces are the most important force contribution when the AFM tip is very close to the sample surface. The origin of these forces is the overlap of the electronic wavefunctions of the AFM tip and the sample and the coulombic repulsion of the ionic cores.

The overlap of electronic wavefunctions is the origin of two opposite force contributions depending on the type of sample:

1. The overlap is responsible for covalent or metallic bonding and consequently causes strong attractive forces. These forces may even prevent

from successful contact mode AFM measurements as seen in the example of the Si(111) 7x7 surface. Only covering the tip with a thin PTFE film enabled imaging of this surface as neither the fluorine nor the carbon atoms of PTFE are able to bind covalently to the dangling Si bonds [11].

2. The overlap originates a repulsive force, if electrons have to be lifted to energetically unfavorable levels to fulfill the Pauli exclusion principle when the tip is approaching the sample.

More pronounced is the electrostatic repulsion contribution to the overall force due to the ionic cores. This repulsion contributes more to the force corrugation than interactions of the electronic wavefunctions which additionally are heavily distorted [12].

The repulsive interaction has a very steep characteristics and can be modeled either by an exponential with a decrease length of typically 0.2 Å or a power law with an exponent of -12.

### 2.1.2 Van der Waals forces

The origin of van der Waals forces is the dipole-induced dipole interaction of neutral atoms and molecules or macroscopic bodies. Instantaneous moments of otherwise nonpolar atoms induce polarity in neighboring atoms which results in an attractive force<sup>1</sup>. The classical London equation [13] describes the interaction energy between two nonpolar molecules at a distance  $z$ :

$$U_n(z) = -\frac{3}{4} \frac{\alpha^2 h \nu}{(4\pi\epsilon_0)^2 z^6} = -\frac{C_n}{z^6}, \quad (2.1)$$

where  $\alpha$  is the polarizability,  $\nu$  a characteristic absorption frequency (typically in the UV-regime),  $h$  Planck's constant and  $\epsilon_0$  the dielectric constant in vacuum. In a distance of 5 to 100 nm retardation effects become dominant. In this case the interaction energy is [14]

$$U_r(z) = -\frac{23hc\alpha^2}{8\pi^2(4\pi\epsilon_0)^2 z^7} = -\frac{C_r}{z^7}. \quad (2.2)$$

and often referred to as the Casimir interaction. The interaction time is becoming longer than the typical time of fluctuation of the dipole which causes the change of the exponent in the power law.

---

<sup>1</sup>The simplest way to understand this phenomenon is the case of an hydrogen atom in front of a flat plate. The circulating electron generates a fluctuating dipole moment which interacts with its antiparallel image moment attractively.

Neglecting many body interactions by assuming additivity of the van der Waals force, the nonretarded force between a sphere, representing an AFM tip, and a plane, representing a sample, is given by

$$F_n = -AR/z^2$$

, where  $A$  is the Hamaker constant. For the retarded case

$$F_r = -2\pi BR/(3z^3)$$

is obtained, where  $B$  is the retarded van der Waals constant, hence both power laws have a quite weak distance characteristics compared to the short range forces. In the above equations the constants  $A$  and  $B$  have to be determined. They depend on the dielectric constants of the tip, the immersion medium and the sample. Van der Waals forces are typically in the range of 1 to 20 nN. Assuming a tip radius of 100 nm and a tip-sample distance of 1 nm, Goodman and Garcia [15] calculated 1.2 nN for a SiO<sub>2</sub> tip and a graphite sample and 19 nN for a diamond tip and a AgBr sample.

### 2.1.3 Long range electrostatic forces

As typical tips are made of conducting materials forces of this type usually should not influence measurements by atomic force microscopy. However, charged insulating materials create image charges at the tip. A special case are the piezolevers used for the imaging process in our UHV microscope which are always biased and thereby always interact with image charges or real charge patches on insulating samples. When working with ionic crystals as potassium bromide and magnesium oxide the question arises if the separated ions of opposite charge present at these surfaces can be distinguished by the AFM. Calculations for the surfaces of LiF(100) and MgO(100) support this possibility [16] but an ideal monatomic tip and a very close tip-sample distance would be necessary.

So far, only Giessibl and Binnig were able to resolve both types of ions on KBr(100) in UHV at 4.2 K [17] successfully. However, they make the van der Waals interaction responsible for the imaging mechanism rather than electrostatic interactions. Additionally, in the KBr crystals, the potassium and the bromine ions have comparable ionic radii which facilitates resolution of both species. Other results reported for ionic crystals always resolved one of the two species only [18, 19].

Electrostatic forces also occur if an insulating sample carries a net charge. These are strong long range forces which can exceed by far van der Waals



forces. They can be used for keeping the tip far off the sample and enable imaging of very delicate samples [20,21]. For topographic images of a surface, such forces are undesirable, because they create a larger tip-sample distance decreasing spatial resolution. If the charge is distributed unequally over the surface, they even create artificially topography-like features if they are not extracted by a special setup.

The force  $F_{el}$  between the tip and the sample consists of two components: A part due to charges present on an insulating sample and a capacitive part due to the capacitor constituted by the tip and the sample.

The first one is described by [9]

$$F_{charge} = q_t E_z.$$

$q_t$  is the induced charge and has two contributions:

$$q_t = -(q_s + CV)$$

, where  $q_s$  is the induced charge on the tip by the surface charge distribution and the term  $CV$  originates from the voltage  $V$  and the capacitance  $C$  between the tip and the sample.

The latter one is:

$$F_{capacity} = \frac{1}{2} \frac{\partial(CV^2)}{\partial z}$$

The total force is then described by the sum of these two contributions:

$$F_{total} = -(q_s + CV)E_z + \frac{1}{2}V^2 \frac{\partial C}{\partial z} \quad (2.3)$$

This equation offers the possibility to distinguish charge forces from other forces. Changing the polarity of an external voltage changes the sign of the charge force contribution. If the external voltage is modulated  $V = V_0 + V_1 \sin \omega t$ , the capacitance contribution can be measured separately at  $2\omega$ .

### 2.1.4 Capillary forces

Under ambient conditions AFM measurements are strongly influenced by the presence of water vapor. Surfaces are covered with a thin water film, which can reach a thickness of several monolayers. When the AFM tip comes into contact with the surface, a meniscus is formed which strongly attracts the tip. The interaction is dominated by the Laplace pressure and strongly depends

on the contact area. A rough estimate of the maximum capillary force is given by [9]

$$F_{max} \approx -4\pi R\gamma.$$

To avoid these forces which can be as high as 100 nN, measurements must be performed in liquids or in vacuum. Interestingly, only low humidity causes severe problems for successful imaging whereas it has been reported that the resolution improves with increasing humidity because friction and adhesion are reduced by the adsorbed water film [22].

## 2.2 The atomic force microscope

Like other scanning probe techniques, atomic force microscope (AFM) utilizes the near-field interaction of a sharp tip and a sample to provide high resolution topographic images. Whereas the first instrument working with this technique, the scanning tunneling microscope (STM), senses the tunneling current between a sharp tip and a conducting surface, the AFM is sensitive to the force field either at or close to the surface. Thus the AFM is not restricted to conducting samples and apart from the possibility to map the topography of all kinds of samples its most important property is the capability to investigate forces originating from adhesion [23], surface charges [24–26], magnetic interactions [27] and friction [28].

The principle of operation is shown in Fig. 2.1. A tip which is attached to a soft cantilever is scanned at a surface by means of piezoelectric elements<sup>2</sup>. Due to the force interaction between tip and sample the cantilever is deflected from its initial position upon scanning. This deflection can be detected and is either kept constant to provide images recorded at a constant force or is directly used as an image of the surface<sup>3</sup>. Supposing that the force interaction does not vary at different positions at the surfaces, the topography of the sample is recorded. This assumption is generally made when imaging surfaces but does not hold at all if the lateral variation of forces due to e.g. magnetism or charges is of interest. (See 2.1.3)

The most difficult part to be realized for AFM is the detection of the deflection of the cantilever and the fabrication of the cantilever itself. The

---

<sup>2</sup>The most widely applied is the single piezotube with quartered electrodes, even if there are still other types of geometries used [29].

<sup>3</sup>This is the static measurement of forces which is nearly exclusively applied to measurements when the tip is in contact with the sample. Non-contact mode measurements are mainly dynamic measurements and are thus sensitive to force gradients (See 2.2.3)

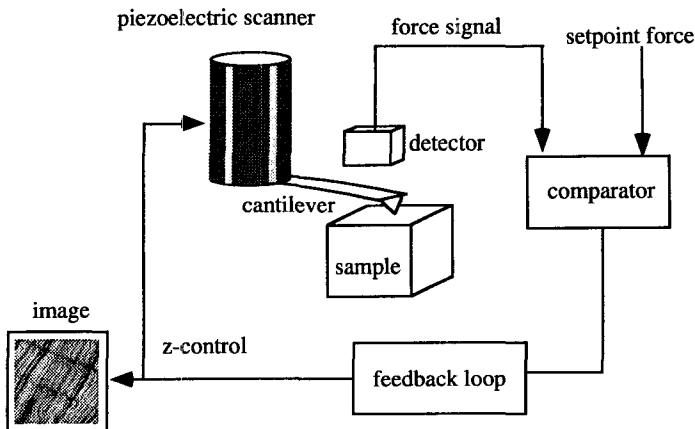


Figure 2.1: Principle of operation of the atomic force microscope.

first AFM [6] was directly inspired by the STM principle and used a tunneling tip on the backside of a thin conducting cantilever to measure the deflection. The cantilever itself consisted of a thin aluminium foil to which a diamond shard was glued. The shard acted as a tip. Other kinds of detection schemes have been developed later, like capacitive detection, interferometric detection, deflection of a laser beam [9] and piezoresistive detection [30, 31].

Microfabricated cantilevers (mainly made of silicon or siliconnitride) are now commercially available for many purposes and make homemade ones obsolete. I will focus on the laser beam deflection technique, which is the most widely used to date, and on the piezoresistive detection, which is one of the most promising newer developments in the field simplifying especially the application of AFM in UHV environment.

### 2.2.1 Laser beam deflection (LBD) detection technique

The angular movement of a surface can be detected by the reflection of a light beam from its backside. This principle is well known and widely applied. For example, the torsion balance is based on this principle [32], which e.g. has been used to measure the Einstein-de-Haas Effect and the equivalence of

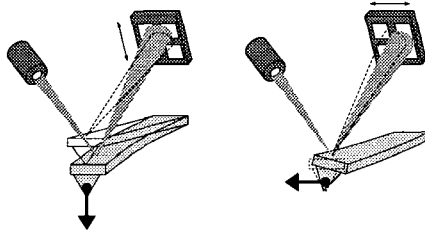


Figure 2.2: Principle of simultaneous detection of lateral and normal forces by the laser beam deflection detection technique (after [35])

inertial and gravitational mass. Not surprisingly, this principle has been applied to the detection of the deflection of an AFM cantilever by G. Meyer and N. M. Amer [33] and S. Alexander *et al.* [34]. In the original setup a HeNe laser beam was focused on a tiny mirror glued to the backside of the cantilever. The reflected beam was guided to a position sensitive detector (PSD) which consisted of a photodiode split in two segments. Bending the lever by an angle  $\alpha$  provokes a displacement on the PSD of

$$X = 2\alpha L = 3\frac{L}{l}\delta z$$

where  $L$  is the length of the light path and  $l$  the length of the cantilever [35]. This first approach used a 2-segment photo diode to sense the one dimensional bending of the cantilever normal to the surface. A straightforward extension was the introduction of a 4-segment photodiode by G. Meyer and N.M. Amer [18] and O. Marti *et al.* [36] which enabled a two-dimensional detection including now lateral bending of the cantilever.

### Sensitivity

The sensitivity of the beam deflection can be modeled assuming a rectangular beam profile with a uniform distribution of the light intensity. The change in intensity due to a deflection of  $\delta\beta$  is then

$$\delta I = 2\frac{\delta\beta}{\beta_0}I_{tot} \quad (2.4)$$

where  $\beta_0$  is the divergence and  $I_{tot}$  the total intensity of the beam. The sensitivity thus increases with the light intensity reflected from the cantilever and decreases with the divergence of the beam. The ideal case is a focused beam which matches the cantilever width exactly to give the highest reflected

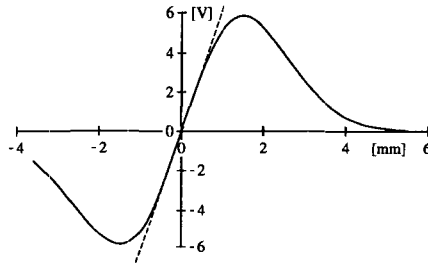


Figure 2.3: Measured signal of the difference signal as function of the position of the laser beam on the photodiode. From [38].

intensity at the lowest beam divergence. Furthermore, as the TEM(00) mode of a gaussian laser beam fulfills the condition of the smallest possible divergence at a given focus, it is the optimal light source for the beam deflection technique<sup>4</sup>. The measured signal from the PSD, which is obtained upon displacing the laser beam on the photodiode is given in Fig. 2.3. The working area is given by the approximately linear region.

### Noise sources

Specific noise sources of the beam deflection technique are due to the laser light.

1. The laser light is exerting a light pressure on the backside of the cantilevers. A perfectly constant light beam would only provoke a force offset, which is easy to correct for. Thus, only intensity fluctuations (e.g. due to mode switches) generate noise, which is about 0.2 fN for 0.1% intensity fluctuations of a 300  $\mu$ W laser diode [35].
2. As typical cantilevers are coated at their backside to enhance reflectivity, a bimetallic effect occurs when they are heated up by the laser light. This effect can be as high as 20 nN/mW laser power in vacuum. Once again it is only the fluctuation of the laser power, which generates noise. Under the same conditions as mentioned above, 6 pN are obtained [35].

---

<sup>4</sup>Howald *et al.* notice that edge emitting LED's, which also allow a sufficient focusing of the light beam, are even better light sources for this detection technique. This is ascribed to a drastically lowered  $1/f$  noise and reduced interference effects on the large scale due to their much shorter coherence length [37].

3. The ultimate limit in the LBD detection scheme is the shot noise limit which originates in the discrete characteristics of the photons. This generates a noise in the force measurements as low as  $2 \cdot 10^{-18}$  N [35].

Summing up these terms and adding noise contributions of thermal noise (see 2.2.3), which is not specific for this detection scheme, the noise in a LBD system can be considered to be as small as  $0.1 \text{ \AA}$  in a static measurement and  $10^{-4} \text{ \AA}/\sqrt{\text{Hz}}$  [9, 33] in dynamic measurements.

## 2.2.2 Piezoresistive detection

Even if laser beam deflection is the most widely applied method to date at least under ambient conditions, it requires mechanical components for alignment of the beam path. However, in ultrahigh vacuum (UHV) some inconveniences appear. Either the entire optical adjustment facilities are located outside the chamber, with huge disadvantages for the vibration damping, or the necessity of aligning optical components in UHV appears [37, 39]. Alternatively, the microscope is adjusted outside the chamber and is introduced e.g. by a load-lock. A rigorously stiff setup avoids further adjustment in UHV [40, 41].

Nevertheless, a sensor completely integrated within the cantilever would be the most elegant approach to sense forces in UHV. One of the most promising developments in this field, besides integrated capacitive cantilevers [42] or piezoelectric cantilevers [43], is the piezoresistive cantilever. Invented by M. Tortonese [30] for the detection of normal forces, it has later been extended to the detection of lateral forces as well [44]. The piezolevers we used (Auto-probe VP piezolevers, Park Scientific Instruments, Sunnyvale, CA) are based on the original design of M. Tortonese, which is described in the following.

These piezolevers are microfabricated from silicon. The tip is formed by standard silicon etching procedures; subsequently the cantilever is doped by boron (boron rich layer is about  $1 \mu\text{m}$  thick) and covered by silicon oxide. The boron-doped p-type Si layer provides the necessary piezoresistive effect far from the neutral axis of the cantilever thus the maximum resistance change upon bending is obtained.

### Sensitivity

The sensitivity of a piezoresistive cantilever is given by the fractional resistance change in dependence on the deflection of the cantilever. For a cantilever which consists of two legs connected by a triangular top region (cf.

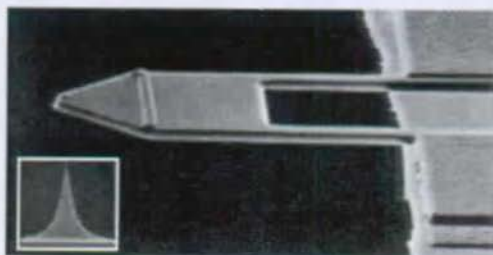


Figure 2.4: Micrograph of a piezolever [30]

Fig. 2.4) it is found, assuming that the top region does not contribute to the resistance,

$$\frac{\Delta R}{R} = \beta \frac{3\pi_L E t b (L_1 + L_2)}{4 \left( (L_1^3 - L_2^3) b + 3L_2^3 w \right)} \delta z, \quad (2.5)$$

where  $R$  is the resistance of the cantilever and  $\Delta R$  is the resistance change due to a deflection  $\delta z$  at the free end of the cantilever.  $\pi_L$  is the longitudinal piezoresistive coefficient of the cantilever and the factor  $\beta$  takes into account, that the piezoresistor is not confined to the surface of the cantilever.  $L_1$  is the overall length of the cantilever,  $L_2$  the length of the triangular top region, and  $b$  is the overall width of the lever [30].

The fractional change  $\frac{\Delta R}{R}$  is measured by means of a wheatstone bridge.

### Noise sources

The yet undetermined detection limit for the deflection of the piezolever is not only given by its sensitivity but also by the specific noise sources. The mechanical thermal noise is expected to be the same as in the case of LBD detection. Intrinsic to the piezolever is Johnson noise due to thermal motion of electrons in a resistor which is given by

$$V_n = \sqrt{4kTR\delta f}, \quad (2.6)$$

where  $V_n$  is the thermal electric noise,  $k$  the Boltzmann constant,  $T$  the temperature and  $\delta f$  the bandwidth of the measurement. Another noise source is  $1/f$  noise which becomes dominant if the voltage in the wheatstone bridge is increased. Tortonesi [31] specifies the noise in a 10 Hz to 1 kHz bandwidth at 5 V bridge bias for a lever length of 200  $\mu\text{m}$  and a thickness of 5  $\mu\text{m}$  to about 0.1  $\text{\AA}$ , which is about the same as for the LBD detection.

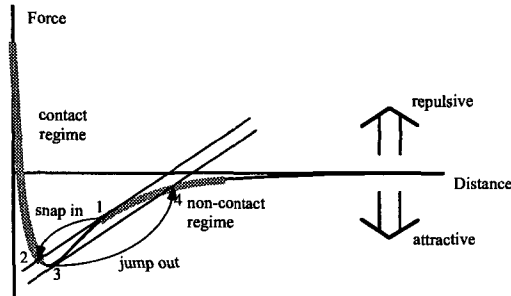


Figure 2.5: Schematic of the force acting on an AFM cantilever.

### 2.2.3 Modes of operation

In atomic force microscopy two different modes of operation are distinguished: the contact mode and the non-contact mode. From the theoretical point of view this distinction is quite arbitrary as one should be able to measure the force between the probe tip and the sample at any distance in the same way. Moreover, when does contact really occur at this nanometric scale? Another definition for these modes is to call the contact mode repulsive mode as the tip is in the repulsive regime of the tip-surface potential and the non-contact mode attractive mode. However, repulsive forces may be present in the non-contact mode, too.

The definition contact mode and non-contact mode originates from the experimentally verified fact that virtually all levers reach a point where no stabilization of the force is possible and they snap into the regime of the short range repulsive forces mentioned in 2.1.

A simple representation of the force the tip experiences in a surface potential is shown in Fig. 2.5, deduced from a Lennard-Jones type potential. The straight line represents Hooke's law for the cantilever. The marked regions refer to the contact and non-contact regime of operation. Between the points 1 and 2 there is a instable region, where the tip jumps into contact. A hysteresis is expected, since the instability with tip retraction occurs at the point 3. Only a cantilever with a force constant higher than the maximum force gradient of the potential will be able to overcome the effect of jump into contact.



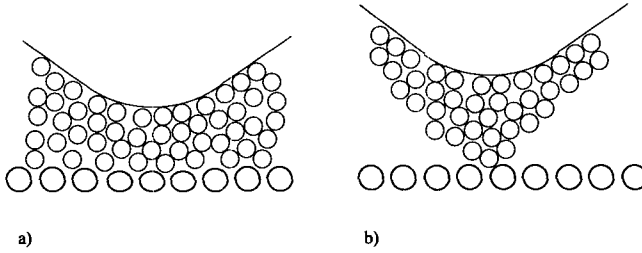


Figure 2.6: Models of an AFM tip in contact with the surface. a) A large contact zone is formed and the surface may even be deformed by a blunt tip. b) Ideal case, where a single atom forms the tip.

### Contact mode operation

In Figure 2.6 the situation of an AFM tip being in contact with the sample is sketched. The adhesion force and the external force applied via the cantilever are balanced by the short range repulsion. (See 2.1)

Typically, a contact zone is formed which is much larger than a single atom. The radius of this zone depends strongly on the external force applied to the cantilever, the adhesion and the elastic properties of sample and probe. Following a theory of Johnson, Kendall and Roberts, Israelachvili [45] calculated the radius of contact,  $a$ , between a sphere of radius  $R$  pressed by an external force  $F$  to a surface with a compressive constant  $K$  and an interface energy  $\gamma$  to

$$a^3 = \frac{R}{K} (F + 6\pi R\gamma + \sqrt{12\pi R\gamma F + (6\pi R\gamma)^2}). \quad (2.7)$$

The principle of operation in contact mode has been shown above in Fig. 2.1. The force detected by the cantilever is compared to a setpoint force. A feedback loop provides the voltage which is applied to a piezoelectric element to match the detected force with the setpoint force. If the feedback loop responds fast enough the variation of the force, this voltage provides the height information of the sample. This is called the *constant force mode*. Another possibility is to keep the distance between the cantilever and the sample constant and record the changes in force as a height information. This is only useful for very flat surfaces and enables a high scanning speed. Otherwise very high forces may be applied to the surface accidentally. This way of operation the microscope is called the *constant height mode*.

The contact mode provides in general the best resolution due to the steep characteristics of the interaction. But there are some limitations: The most important one is that the measurement may become destructive on soft samples. Highly reactive surfaces may form bonds to the cantilever (e.g. on the Si(111) 7x7 reconstruction [11]) and render measurements in contact mode impossible. To avoid these problems the contact mode has been modified to reduce the problems which are mainly caused by lateral forces<sup>5</sup>. Operating modes like tapping mode (Digital Instruments, Santa Barbara, CA, USA) or intermittent contact mode (Park Scientific Instruments, Sunnyvale, CA, USA) are now commercially exploited to overcome this disadvantage.

Another disadvantage occurs on atomic scale measurements. Whereas atomic resolution has been claimed to be obtained very early on layered materials [46] it was stated later that these results were not obtained by a single atom at the end of the tip for two reasons:

- The forces applied to obtain atomic resolution were by far higher than a single single atom can withstand;
- Nonperiodic features like point defects or steps were not resolved.

For these layered materials, even the shearing of flakes was discussed as responsible for the imaging process. Later on, atomic resolution on ionic crystals and resolution of defects like steps and point defects was reported [17]. Mainly the phase-locked multitip scenario [47] seemed to be responsible for resolution of atomic corrugation. In this explanation, many tip atoms which adapt the periodicity of the surface are responsible for a pseudo-atomic resolution (Fig. 2.6).

### Non-contact mode operation

The only convincing way to overcome the mentioned disadvantages is the non-contact mode. In non-contact mode the tip is kept in the attractive range of the surface potential just before the jump into contact. Principally, this could be a static measurement as well, but the forces acting at the increased distance are so small that a dynamic measurement has to be applied<sup>6</sup>. Dynamic measurements base on the fact that an oscillator changes its resonant frequency when subjected to a force gradient. Two different dynamic

---

<sup>5</sup>Nevertheless, the capability to measure lateral forces on a nanometric scale is one of the most important capabilities of AFM with LBD detection scheme.

<sup>6</sup>To measure small forces, a compliant cantilever must be used. But the more compliant the cantilever the larger the region of instability [35].

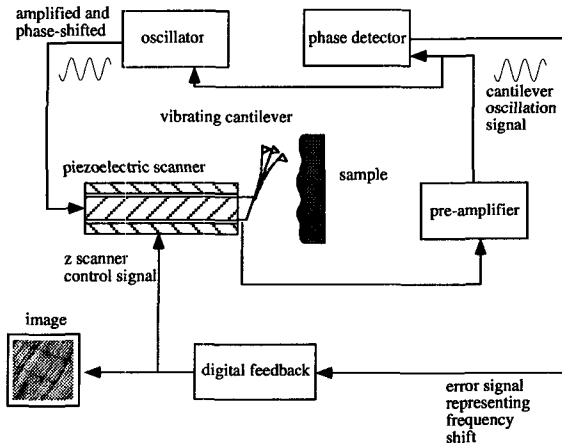


Figure 2.7: Principle of dynamic non-contact detection

measurement methods exist: The amplitude modulation (AM) technique and the frequency modulation (FM) technique.

With the first technique, the amplitude of the lever signal is measured at a given frequency close to the resonant frequency by a lock-in amplifier. As the frequency changes the amplitude at the set frequency decreases and serves as feedback signal. The main disadvantage of this method is the small bandwidth which can be obtained and which decreases as the quality of the oscillator increases. In UHV the quality of the oscillation of the cantilever is usually very high ( $Q \approx 10^5$ ), thus this method is not well suited.

For this reason the frequency modulation (FM) technique has been developed [48]. In FM non-contact mode, the cantilever is driven at a fixed amplitude of vibration, and its changes in vibration frequency are detected. The advantage of the method is that the frequency is instantaneously modulated by variations in the force gradient acting on the cantilever, in contrast to the amplitude. The principle of operation is shown in Fig. 2.7. The basic operation is not changed compared to the static contact AFM technique - an error signal serves as control parameter for a feedback loop which is acting on the z-drive of the piezoelectric scanner. Here the error signal is the frequency shift of the cantilever. The essential components for the frequency modulation technique are the oscillator and the phase detector.

1. The oscillator itself consists of a feedback loop. It compares the am-

plitude of the cantilever oscillation signal from the pre-amplifier to a reference amplitude setting. The difference of the two amplitudes is multiplied by a gain factor and used to produce a signal that is sent to the piezoelectric scanner to oscillate the scanner and therefore the cantilever. To compensate for the phase difference between the cantilever oscillation signal from the pre-amplifier and the output signal to the piezoelectric scanner a phase shift may be introduced. It is important to note that the oscillator does not affect the frequency of the cantilever. It sends a signal of the *same* frequency to the cantilever to make it oscillate at the set amplitude. This frequency is given by the properties of the cantilever and the force gradient that is acting on it.

2. The phase detector has the following functions: It is used for setting the reference frequency analogous to the setpoint in contact mode AFM. It detects the input cantilever oscillation signal and compares its frequency to the reference. From the difference of these signals an error signal is created which serves as signal for the microscope feedback loop.

In the phase detector the signal is passed through a tuneable bandpass filter which is set to the reference frequency. A characteristic property of a bandpass filter is that it introduces a frequency-dependent phase shift to any signal that does not match this frequency. Thus, if the bandpass filter is set to the resonant frequency of the cantilever any shift in the cantilever oscillation frequency (due to changes in the force gradient experienced by the tip) produces a phase shift in the output of the band pass. The shifted and the unshifted, original signal are then passed through a phase comparator which outputs a phase difference. This difference reflects the shift in oscillation frequency due to changes in the force gradient and serves as error signal in the z-feedback loop. The error signal which is created in this way is displayed in Figures 2.8 and 2.9, respectively. Around the setpoint frequency an approximately linear regime is obtained which is the working range for the frequency shift, comparable to the linear regime of the PSD output in the static LBD measurement (Figure 2.3).

The non-contact mode thus maps contours of a constant force gradient. This is generally considered as the topographic information. Nevertheless, other interactions than pure van der Waals interaction may interfere and have to be separated carefully from the true topographic information (see e.g. 2.1.3), providing even valuable additional information.

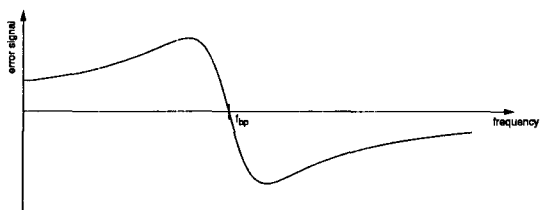


Figure 2.8: Output of the phase detector. The bandpass is tuned to  $f_{bp}$ ; the input signal is a sine wave generated with a function generator.

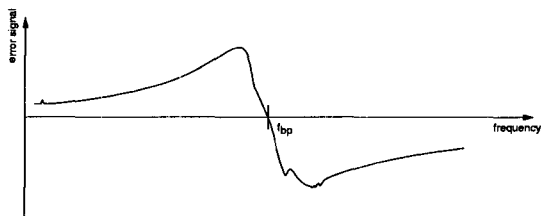


Figure 2.9: Output of the phase detector. The bandpass is tuned to  $f_{bp}$ ; the input signal comes from the oscillating cantilever.

### Resolution limits

As the cantilever is free to vibrate in non-contact measurements, thermal noise is the essential limiting factor for the resolution. According to the equipartition theorem, every degree of freedom is associated with the thermal energy  $\frac{1}{2}k_B T$  ( $k_B$ : Boltzman's constant). The cantilever has two degrees of freedom, one for the potential and one for the kinetic energy. We only detect the kinetic one, thus the average thermal vibration amplitude  $z_{osc}$  is given by

$$\frac{1}{2}k\langle z_{osc}^2 \rangle = \frac{1}{2}k_B T. \quad (2.8)$$

The measurement is performed in a certain bandwidth  $B$ . The thermal noise has to be calculated in this bandwidth by means of the cantilever response function and the thermal white noise ( $m$ : mass of the cantilever,  $\omega_0$ : resonant frequency)

$$\Psi_{th}(\omega) = 4m\omega_0 k_B T / Q. \quad (2.9)$$

The thermal white noise decreases as the quality  $Q$  increases, high- $Q$  cantilevers have less noise off resonance which reduces the noise in non contact measurements. The thermal oscillation amplitude on resonance  $\omega = \omega_0$  is

$$\langle z_{osc}^2 \rangle = \frac{4k_B T Q B}{k\omega_0} \quad (2.10)$$

and off resonance  $\omega \neq \omega_0$

$$\langle z_{osc}^2 \rangle = \frac{4k_B T B}{Qk\omega_0}. \quad (2.11)$$

Thus for high  $Q$  cantilevers the noise is centered around the resonant frequency. Consequently, for measurements where the bandwidth  $B$  is far below the resonant frequency, like in contact mode, thermal noise is negligible. The smallest detectable amplitude of oscillation for a signal-to-noise ratio of one is

$$\delta z_{min} = \sqrt{\frac{4k_B T B}{k\omega_0 Q}} \quad (2.12)$$

and the smallest detectable force gradient is

$$\frac{\partial F}{\partial z}_{min} = \sqrt{\frac{4kk_B T B}{k\omega_0 Q \langle z_{osc}^2 \rangle}}. \quad (2.13)$$

Equation (2.12) shows that high  $Q$  and low  $k$  cantilevers are preferable for high resolution measurements. In UHV  $Q$ -factors up to  $10^5$  have been measured; this is why UHV is the ideal environment for non-contact mode measurements. On the other hand, cantilevers have to be stiff (typically  $k \geq 10 \text{ N/m}$ ) to avoid snapping in. Due to these restrictions atomic resolution has been reported relatively late for non-contact AFM [10]. But there are additional limitations. Unlike STM, where the exponential distance characteristics of the tunneling current favors a protruding atom by far with respect to all other tip atoms, in non-contact mode AFM the interaction is much less distance dependent, which makes atomic resolution much more difficult to obtain.

## Chapter 3

### Experimental

In this chapter, I will describe the setup of two beetle-type AFMs. The first one is a microscope using the laser beam deflection technique to detect the cantilever deflection and was used under ambient conditions; for the second one the piezolever technique is employed to simplify operation in ultrahigh vacuum (UHV). Exemplary data illustrate the performance of these instruments. The principle of the beetle-type setup is shown in Fig. 3.1 [49, 50]. The microscope body rests with three piezotube legs on a sample holder with helical ramps. By applying appropriate voltages to the piezolegs, the microscope can move, either circularly, which enables the approach on the ramps, or linearly in every direction in order to examine different surface regions.

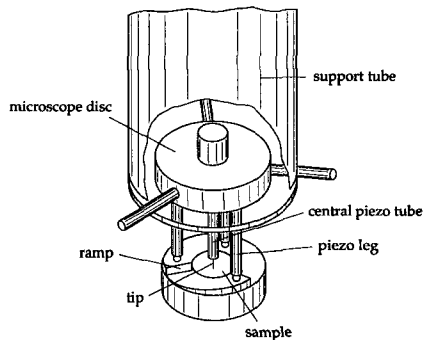


Figure 3.1: Sketch of the “beetle-type” STM. The body of the STM is placed on a circular ramp. The coarse approach between the tip and the sample is achieved by a clockwise rotation of the STM over a circular ramp.



We chose the beetle-type design since it compensates to first order thermal drift of the tip-to-sample distance. The setup is rather compact which yields high mechanical eigenfrequencies and thus a low sensitivity to external vibrations. In addition small distances of the reflected beam result in low drifts of the force setpoint. A further advantage for us was compatibility to the design of our variable temperature STMs [8]. The first AFM we designed in this geometry was the one employing the laser beam deflection technique. We have used the experiences gained with this instrument to develop an AFM employing the piezoresistive detection scheme for further simplifying the application to variable temperature and ultrahigh vacuum.

### 3.1 The LBD beetle-type AFM

The setup of our LBD-AFM consists of a very compact scan head which rests with its three outer piezolegs on the sample holder as shown in Fig.3.1. A comparable setup is the one of Dai *et al.* [51]. Wiechers [41] has recently reported the construction of a beetle-type AFM where the geometry is such that the sample lies on three piezolegs and the microscope body is at rest, the same as originally designed by Besocke [49].

All optical components necessary for the beam deflection method together with mechanical adjustment facilities have been integrated into a scan head of 40 mm diameter.

#### 3.1.1 The AFM Head

A schematic drawing and a photograph of the beetle-type AFM are shown in Figs. 3.2 and 3.3 respectively. The microscope stands upon ruby balls, which are glued to the ends of the three outer piezos, on a triple helix sample holder. The sample holder provides the three ramps for coarse inertial approach and is made of anodized Al in order to obtain hard surfaces for the sliding motion of the ruby balls. (For UHV e.g. polished Mo can be used.)

The cantilever is fixed to the central piezo. The microscope head comprises 4 disks. Each of them carries one optical component of the beam deflection technique. Their lateral positions with respect to each other are well defined by leaf springs that connect successive disks. Their respective distance and tilt can be adjusted via three screws which are under preload by the leaf springs. The uppermost disk (1) carries the light source (16). For operation in air it is most appropriate to mount the laser diode (e.g. HITACHI HL7806G,  $P_0=5$  mW,  $\lambda=780$  nm) directly onto the disc of the AFM

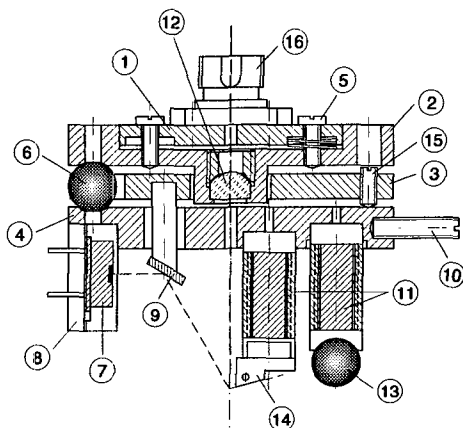


Figure 3.2: Section of the LBD-AFM (scale approx. 2:1).

head. (See the photograph) For UHV applications, the laser diode must be placed outside the vacuum chamber since it would likely be destroyed during bake out. In this case a single mode fiber is used to transmit the light to the AFM head. Its end is the light source ( $\varnothing 5 \mu\text{m}$ ). For tests in air we used a "pigtailed" laser diode (diode HITACHI HL7812G,  $\lambda=780 \text{ nm}$ , pigtailed by Seastar Optics Inc., Canada, power at the fiber end 3 mW). The fiber is typically glued to a UHV feedthrough and therefore attached to the chamber. For practical reasons it is convenient to be able to disconnect the microscope from the chamber. Therefore we chose a FC/PC connector between the light emitting fiber end and the uppermost disk of the AFM. (See drawing for this version of the disk) This connection guarantees a well-defined lateral and vertical position of the fiber end so that disconnecting and reconnecting of the fiber requires only minor readjustment of the optics. In front of the light source, a lens (12) ( $f=5 \text{ mm}$ , "best form", Melles Griot, Darmstadt, Germany) is mounted rigidly onto the second disk (2). It generates an image of the light source (4 times enlarged) onto the backside of the cantilever. The diameter of the resulting spot can be adjusted by varying the distance of the light source, i.e. disk 1, with respect to this lens, i.e. disk 2, by turning three focus screws (5). The smallest obtainable spot diameter



Figure 3.3: Photograph of the AFM. The AFM stands on the sample holder which is mounted on a stack of copper plates. In this configuration used for operation in air, a laser diode is directly mounted as a light source.

is about  $20\text{ }\mu\text{m}$ , which is less than the width of commercially available cantilevers ( $20\text{--}40\text{ }\mu\text{m}$ ). The position where the laser spot hits the cantilever can be adjusted by tilting the whole assembly comprising light source and lens, i.e. disk 2, with respect to disk 4, to which the piezos and the cantilever are mounted. This is achieved by two screws (not visible in Fig. 3.2) which define a plane together with the stainless steel ball (6). Finally the beam, after being reflected from the cantilever, must be positioned onto the center of the four quadrant photo-diode (SFH244S, Siemens (7)) at zero force. This adjustment has been divided into coarse and fine parts in order to have the necessary precision and to be able to use several levers on a multilever chip without moving it in its holder: The detector (7) can be moved by  $\pm 1\text{ mm}$  in  $x$  and  $y$  before it is clamped on the brim of its housing (TO39) into a chassis (8) mounted to disk 4. Once the coarse position of the detector has been fixed, a fine adjustment can be done by tilting the intermediate disk (3) of the microscope which carries a mirror (9) that reflects the beam onto the detector by two screws (15). Tilt of the mirror in two orthogonal directions enables adjustment of both normal and lateral forces. A further possibility for coarse adjustment of the normal force consists in varying the height of disk 3.

These possibilities for adjusting the optical components have proven to make the different adjustment tasks, such as focusing, hitting the backside of

the lever, and guiding the reflected beam onto the middle of the position sensitive detector, sufficiently independent. This allows a stepwise refinement to quickly maximize the performance of the beam deflection method for each lever. The construction of the mechanical components and their connection by leaf springs turned out to be sufficiently stiff to avoid mechanical vibrations below the first eigenmode of the piezo tubes (11). (See below) For sample and tip exchange the whole microscope can be lifted from the sample holder on three screws (10) radially fixed to disk 2. We use micro-fabricated cantilevers made of  $\text{Si}_3\text{Ni}_4$  (STMS-06AU, Park Scientific Instruments, Sunnyvale, CA, USA) with typical force constants of 0.01-0.50 N/m. The cantilever is attached by means of a small spring (W wire) to a small support piece glued to the end of the inner piezo tube. The angle of the cantilever with respect to the horizontal is  $15^\circ$ . The outer electrodes of the piezotubes (EBL No.1, Staveley Sensors, East Hartford, CT, USA) are segmented into quarters. The three outer piezolegs are used for inertial coarse approach and lateral displacement [50]. The outer piezos can also be used for scanning which, however, limits the scan speed due to the inertia of the microscope body. Therefore we usually prefer to scan the tip with the inner piezo. Nevertheless, this causes virtual force changes due to the variation of the angle of the lever upon bending of the piezotube. In addition, since the probe tip is mounted off axis with respect to the piezotube, the height change during the scanning movement has to be compensated by the feedback and causes a tilt of the image. Both effects can be circumvented by bending the piezotube in an S-shape, which can be achieved by subdividing the four electrodes into two pieces each, to which opposite voltages are applied [52]. The coupling of the fast scanning movement, which we chose to be perpendicular to the plane of the beam, to the force signal has been found to be negligible. The vertical displacement of the cantilever is accomplished via the inner electrode of the central piezo tube.

The sample holder is fixed on the upper plate of a conventional stack of copper plates interconnected with viton U's which act as soft, damped springs. This stack efficiently suppresses external vibrations at frequencies higher than the eigenmodes of the individual plates (30-50 Hz). In order to damp vibrations of the building (10-50 Hz), where the transmission of the stack is high, the entire stack resides on a massive stone plate which itself is placed on laser feet damped by compressed air. The mechanical stiffness of the microscope, however, is sufficiently high to allow reliable operation ( $\delta z_{\text{peak to peak}} \leq 0.2 \text{ \AA}$ ) without the air suspension of the table.

### 3.1.2 Electronics

We used a commercial power supply for the laser diode (Type LD-2000, Seastar Optics Inc.) operated at constant current. The current signal from the four quadrants of the position sensitive detector is measured with four I/V converters located close to the microscope (conversion  $10^5 \Omega$ , bandwidth 30 kHz). The vertical and horizontal differences of the signals obtained from the four quadrants are proportional to the normal and lateral force, respectively. For adjustment also the sum of all quadrants, i.e., a signal proportional to the total intensity shining on the detector, is determined. The difference signal for the normal force is compared to a setpoint. This error signal is then amplified with a gain of 0-1000 (speed of the feedback loop) and subsequently integrated ( $4.82 \text{ k}\Omega$ ,  $3.3 \mu\text{F}$ ). The output of the integrator is post amplified (220 V amplifier, using hybrid circuits PA88A, APEX Microtechnology Corporation, Arizona) and then connected to the z-electrode of the central piezotube. The resulting vertical range is 660 nm. The scanning movement and data acquisition is done via commercially available electronics (formerly Besocke delta phi GmbH, now Carl Zeiss Jena). To increase the scan range of the microscope we amplified the x and y signals which results in a maximum scan range of  $3 \mu\text{m}$  at  $\pm 220 \text{ V}$  (high voltage amplifiers identical to those used for z). A PC serves to record the z-signal. Due to the limited resolution of the ADC employed, this is mostly done in the so-called "differential mode" where a 30 Hz (330 Hz) highpass filter of first order is put in series with the ADC. The corresponding recorded images appear as if illuminated from the left.

### 3.1.3 Mechanical Stability

Figures 3.4 and 3.5 represent typical noise spectra taken with the AFM placed on the sample holder. In Fig. 3.4 we show the vibration spectrum recorded with a lock-in amplifier connected to one of the electrodes of the outer piezotubes while a bending motion has been excited by the reference output at the inner piezotube (sinus signal with 10 V amplitude). Thus, the microscope head is vibrated due to the inertia of the inner piezo and the tip holder and the corresponding amplitude is measured as a piezoelectric voltage at one of the legs. The lowest considerable eigenfrequency is at 9.6 kHz and thus satisfactorily high. This shows that the size of our microscope is a good compromise between, on the one hand, the size required for all optical components and an easy-to-operate optical adjustment, and, on the other hand, the desired minimization to obtain high mechanical stiffness. In order to

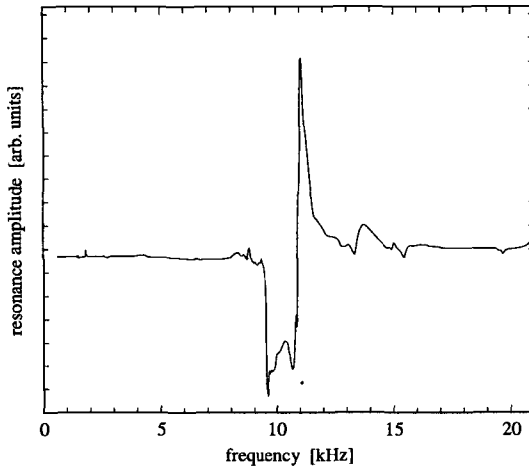


Figure 3.4: Noise spectrum in the range of 200 Hz to 20 kHz. Excitation at the inner piezo tube and mechanical response at one of the outer piezos with the microscope placed on the sample holder.

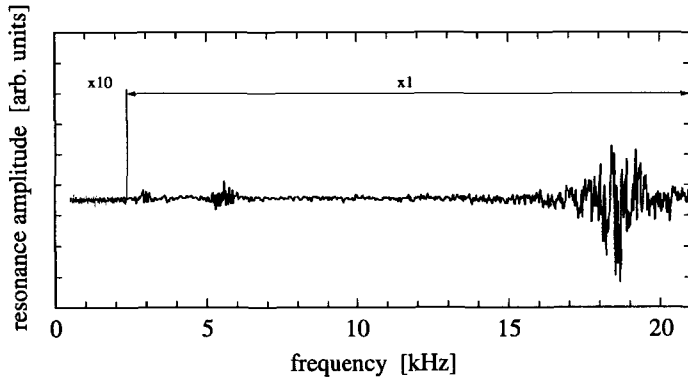


Figure 3.5: Noise spectrum of the force signal in the range of 200 Hz and 20 kHz with the cantilever far away from the sample.

identify the part of the mechanics responsible for this lowest eigenmode, we performed calculations for the bending modes of the disks. These, however, lie far above 10 kHz. In contrast, the lowest eigenmode of the piezotubes themselves seems to be within the frequency range of interest. The resonant frequency of a piezotube can be estimated as follows: A flexible shaft of no mass which is clamped on one side, i.e. a cantilever beam modeling the piezotube, has on its free end a spring constant of  $k = 3EI/l^3$ , with  $E$  being the modulus of elasticity,  $I$  the surface moment of inertia, and  $l$  the lever's length (page 158 of [53]). The fundamental mode of a weightless cantilever beam with a mass  $M$  attached to its free end is

$$\omega_1 = \sqrt{3}\sqrt{EI/Ml^3}. \quad (3.1)$$

That of a cantilever of mass  $m$ , on the other hand, is

$$\omega_2 = 3.515\sqrt{EI/ml^3} \quad (3.2)$$

(p. 223, [53]). Using Dunkerley's formula (p. 302, [53]) the frequency of a cantilever beam of mass  $m$  with a mass  $M$  attached to its free end can be written as

$$\omega^2 = \frac{\omega_1^2 \omega_2^2}{\omega_1^2 + \omega_2^2} \frac{IE}{l^3} \frac{3 \times 3.515^2}{3m + 3.515^2 M}. \quad (3.3)$$

The surface moment of inertia of a tube upon bending is

$$I = \pi 4(R^4 - r^4),$$

where  $R$  and  $r$  are the outer and inner radii, respectively. With the dimensions of our piezotubes ( $R = 0.125''$ ,  $r = 0.115''$ ,  $l = 0.61''$ ,  $E = 8.1 \times 10^{10}$  N/m<sup>2</sup>, and a density of  $7.5 \times 10^3$  kg/m<sup>3</sup>) and a mass at the piezo end of  $M = 0.33$  g, corresponding to that of the tip holder, we obtain  $f = 10.6$  kHz from (3.3). This is close to the lowest eigenmode we measured, which is thus very likely due to a resonance of the inner piezo. This interpretation is supported by the fact that we measure a slightly lower fundamental mode when the microscope is lifted from the sample holder. Then the three legs are free to vibrate at their ends to which the ruby balls are glued. Since the mass of the ruby balls is slightly greater than that of the tip holder, this is expected to lead to a slightly lower eigenfrequency as observed.

In order to characterize the mechanical stability of the positions of the optical components and the coupling of external vibrations to the cantilever, we measured the noise spectrum of the force signal. The AFM tip was far

away from the sample and the only excitation was external noise such as sound and vibrations of the building. This spectrum (Fig. 3.5) is flat apart from the resonance of the cantilever at about 16 kHz, which indicates that external noise sources are damped efficiently by the setup. The fundamental mode of the piezotubes is not excited in this configuration. As expected this changes when the feedback is operating. Then the fundamental mode limits the speed of the feedback loop to values below 10 kHz.

### 3.1.4 Performance

The performance of the AFM is demonstrated by the data presented in Figs. 3.6 and 3.7, where typical images of the KBr(100) cleavage plane are reproduced. In figure 3.6 a large scale constant force image is shown. Monatomic steps can be resolved clearly; they are 3.3 Å in height. In the center of the image screw dislocations emerge, which are the starting points of curved steps. As the surface is subjected to stress during the cleavage, the appearance of such defects is not surprising.

The AFM image in Fig. 3.7 shows a screw dislocation at higher magnification. The apparent width of the step is about 10 nm, which is due to the finite radius of curvature of the tip and also a rough estimation of the minimum distance to distinguish subsequent monatomic steps. A detail taken on the terrace is reproduced in the inset in Fig. 3.7. The atomic rows of the KBr lattice are clearly resolved; the resolution perpendicular to these rows is less prominent. Nevertheless, the square lattice, which is typically attributed to the bromine ions [17] due to their larger ionic radius, can clearly be resolved. The images were taken at a repulsive force of several nano-Newtons. The net force acting on the tip must be much higher, because force-distance-curves yield an adhesion force of 30 nN. Thus, images of this type cannot be used as a proof of true lateral resolution, as forces are much higher than a single atom at the tip apex can withstand. The resolution of the lattice is due to a so-called "phase-locked-multitip" [47] (cf. 2.2.3). The AFM routinely yields atomic resolution also on substrates with lower corrugation amplitudes as, e.g., HOPG ( $\delta z_{typ.} = 0.2$  Å). Therefore we estimate the vertical stability of the beetle type AFM to be less than  $0.2 \text{ Å}_{peak \text{ to peak}}$  in a 10 kHz bandwidth.

## 3.2 The UHV-AFM experimental setup

The LBD AFM of the beetle type described in Sect. 3.1 has one important disadvantage for use in ultrahigh vacuum: The optical pathway is pread-



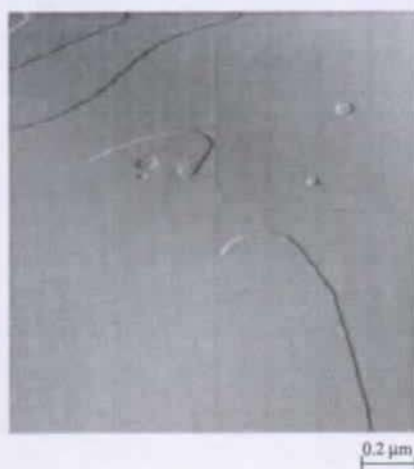


Figure 3.6:  $1.5\ \mu\text{m} \times 1.5\ \mu\text{m}$  image of a KBr(100) surface after cleavage in air. The image is taken in the differential mode; the surface appears illuminated from the left.



Figure 3.7:  $350\ \text{nm} \times 350\ \text{nm}$  section of Fig. 3.6. The inset shows the atomically resolved (100) lattice of the KBr surface ( $50\ \text{\AA} \times 50\ \text{\AA}$ ). Images taken in the differential mode.

justed and cannot be altered from the outside when it is mounted in vacuum. Unfortunately, tip exchange is quite often required in AFM, not only when accidentally breaking a cantilever, but also to use cantilevers with different characteristics. Furthermore the response of the levers during bake out of the UHV-system is not well known and misalignment is likely to occur, which would make measurements virtually impossible. This problem can only be solved with *in-situ* adjustment facilities or a detection scheme with all adjustable parameters outside the UHV-chamber. This task is quite difficult to accomplish for a microscope of small size which is not fixed within the chamber. This led us to the application of the new piezolever technique described in 2.2.2. In this section, I will first describe the setup of the whole combined AFM-FTIR (fourier transform infrared) chamber and secondly the AFM with *in-situ* tip exchange mechanism.

### 3.2.1 The AFM-FTIR ultrahigh vacuum chamber

The UHV chamber of the AFM is based on the combined STM-FTIR chamber which was previously designed [5]. The current chamber was modified in several major ways:

1. The sample was more effectively decoupled from the flow cryostat and other external vibration during measurement by posing it on a vibration damping stack [54].
2. A load-lock was attached to the chamber, in order to introduce cleaved samples.
3. Consequently, the sample manipulator was completely re-designed for a sample exchange mechanism.
4. A variable temperature AFM was designed and attached to the UHV system.

The entire system is shown schematically in Fig. 3.8. It consists of two chambers, in the following called “preparation chamber” and “AFM/FTIR chamber”<sup>1</sup>. The main reason for splitting up the chamber in two parts is to provide separate pumping for the AFM/FTIR chamber. This will be necessary when high pressure ( $p = 10^{-3}$  mbar) experiments will be carried out to come closer to real catalysis conditions. This separation is already useful for preparation

---

<sup>1</sup>This denomination is historical: originally all preparation facilities were installed in one chamber and the STM/FTIR facilities in the other.

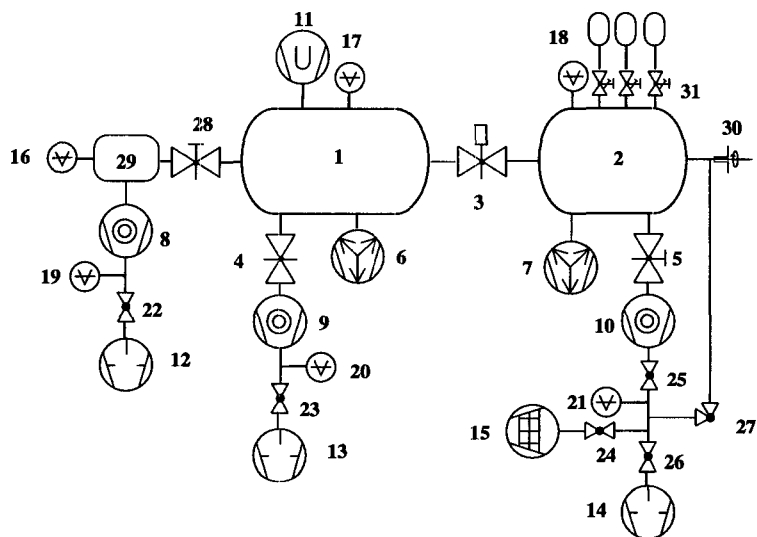


Figure 3.8: Sketch of the vacuum system: 1: preparation chamber; 2: AFM/FTIR chamber; 3,4,5,28: gate valves; 6: ion pump (240 l/s); 7: ion pump (120 l/s); 8,10: turbomolecular pumps (50 l/s); 9: turbomolecular pump (340 l/s); 11: titanium sublimation pump; 12,13,14: rotary vane pumps; 15: LN sorption pump; 16,17,18: ionisation gauge heads, 19,20,21: pirani gauge heads; 22,23,24,25,26,27: seal valves; 29: fast-entry load lock; 30: differentially pumped rotary feedthrough; 31: leak valves.

of the MgO(100) surface at considerably high pressure. The whole chamber is suspended with springs from the ceiling of the laboratory for decoupling from low frequency building vibrations.

The AFM/FTIR chamber is equipped with several gas inlets, which allow for backfilling the chamber with CO, water and oxygen. All the gas bottles are fixed by very short lines to the chamber, which are cleaned via pumping through the chamber before bakeout. The CO gas is of 4.7N purity (Messer Griesheim) and serves as probe molecule in the fourier transform infrared spectroscopy experiments. Water (millipore quality) is prepared in a small glass reservoir by freezing it while pumping. All impurities with a lower melting point than water are pumped in this way.

Oxygen (4.5N purity, Linde) is introduced via a simple gas doser consisting of a glass tube glued to a bored flange which has exactly the diameter of the sample. By means of z-translation, the tube can be approached to the

sample until it fits its external diameter. When the chamber is backfilled by means of this doser, the partial pressure at the sample thus is substantially higher than the background pressure. In general, an overpressure of 10-100 is achieved. This lowers the contamination of the whole chamber when high  $O_2$  partial pressures are required for  $MgO(100)$  preparation. Furthermore the AFM/FTIR chamber is equipped with a Knudsen cell for silver evaporation and a quadrupole mass spectrometer.

The FTIR spectrometer (Galaxy 6020, Mattson Instruments) and the infrared optics are situated in two dry-air purged chambers. They are linked to the AFM/FTIR chamber by home-made KBr windows [5]. The only modification to the existing setup is the adaption to a transmission geometry which is suitable for the transparent metaloxide samples to be studied.

The preparation chamber links the load-lock and the AFM/FTIR chamber. Here the sample transfer takes place. Two viewports provide good visual access. The chamber is equipped with an Auger electron spectrometer with cylindrical mirror analyser, an ion gun with fixed ion energy (800 eV) and a palladium source, which consists of a Pd rod heated by electron bombardment (Omicron Vakuumphysik, Taunusstein, Germany).

The fast entry load-lock is a double cross with a quick access door. Cleaved samples are fixed to a fork on a long travel manipulator, which introduces the sample vertically into the preparation chamber. If purged by liquid nitrogen, a pressure below  $1 \cdot 10^{-6}$  mbar is obtained after pumping half an hour. During the sample transfer the pressure in the main chamber rises to  $5 \cdot 10^{-9}$  mbar.

### Sample Manipulator

A long travel x-y-z manipulator (600 mm travel range, VG Instruments) moves the sample along the main axis of the UHV system; the sample can be rotated around the manipulator axis. A drawing of the manipulator head and the sample dock is shown in Fig. 3.9. A supporting beam (2) is fixed to the manipulator tube (1), a pyramidal centering plate (which is not seen in Fig. 3.9) is fixed on the opposite side. The supporting beam carries the base plate of the sample holder (3). For AFM measurements this base plate is decoupled from the manipulator tube which transmits vibrations. For decoupling a bolt (4), which normally serves as locking element, can be turned in the following way: By means of a linear/rotary feedthrough the screw (5) can be turned. The bolt is forced to follow the movement of the screw by a spring (6) pressing it from underneath until it is locked in the "open" or the "closed" position, respectively, by stops (7). The supporting beam (2) then

is lowered on a stack of copper plates separated by U's made of viton. On the topmost plate (8), its position is centered by three conical supports (9) with the corresponding holes in the base plate of the sample holder (10).

The sample dock is designed for the following purposes:

1. The sample must be attached safely to the sample dock while providing the possibility of a sample transfer.
2. Decoupling from the manipulator tube must be possible for AFM measurement.
3. Heating to high temperatures and cooling must be possible.
4. For transmission infrared spectroscopy, a sufficiently large area of the sample must be kept clear.

The sample ( $\varnothing$  22-24 mm) is fixed by means of leaf springs in a circular sample holder. The top of the sample holder provides the helical ramps for the coarse approach of the microscope. At its sides there are grooves for the fork of the sample transfer manipulator and for the fixing spring (11) at the sample dock. The sample is always transferred in its holder. The sample dock itself is a copper plate which is fixed on its base by three pairs of screws (12). One screw of each pair is making the connection with low heat flow, the second screw pushes the first on to yield in a vibrationless connection [55]. A copper braid (13) attached to the head of a liquid helium/nitrogen flow cryostat (14) provides cooling of the sample dock and the sample. The sample is heated by a filament (15) mounted by means of four ceramic posts (16) at the backside of the sample holder, either simply by radiation or by electron bombardment, which provides high heating power limited by the power supply to about 300 W. The filament setup partially blocks the light path for the infrared beam, when tilting the sample with respect to the infrared beam<sup>2</sup>. A boron nitride heater (Advanced Ceramics, tectra, Germany) is foreseen as a less obstructive alternative heating source.

Measuring the temperature of an insulating sample by a thermocouple is always difficult, as one cannot measure directly the thermovoltage of a thermocouple across the sample as in the case of metals. Thus two interconnected wires of a thermoelement pair have to be used, but this results in a thermovoltage even for bad contact to the sample (e.g. after transfer). For

---

<sup>2</sup>This tilt is necessary if a probe molecule has its dipole moment perpendicular to the surface. In that case, the infrared beam cannot excite the molecule if the E-field is parallel to the surface.

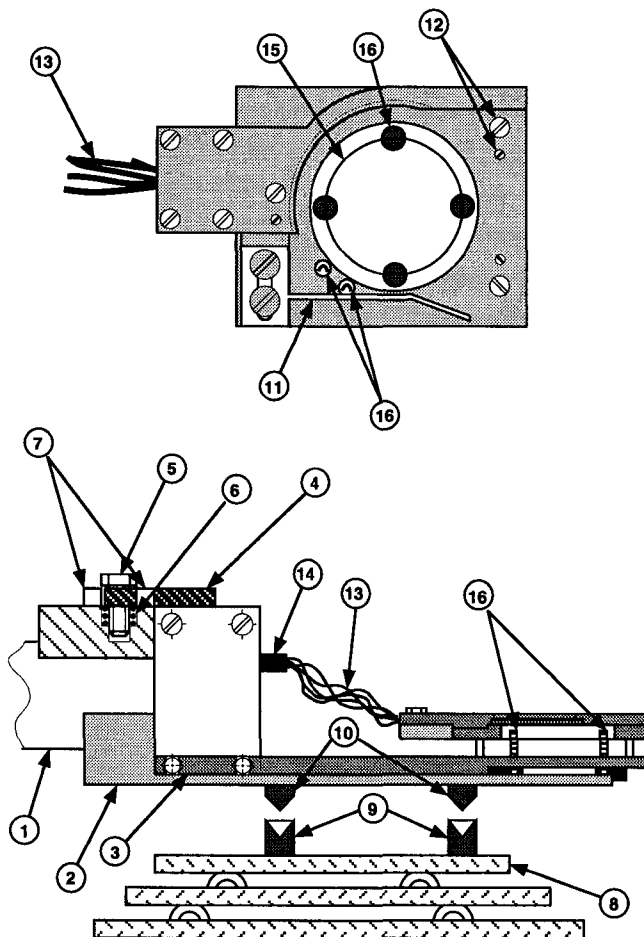


Figure 3.9: Sideview of the sample manipulator (bottom) and topview of the sample dock (top). (1) manipulator tube; (2) supporting beam; (3) base plate of the sample holder; (4) locking bolt; (5) locking screw; (6) spring; (7) stops for (5); (8) vibration damping stack; (9) conical supports with negatives (10); (11) leaf spring; (12) pair of fixing screws; (13) copper braid; (14) cryostat; (15) filament; (16) filament post.

simplicity, in our case two separated wires of a Ni/NiCr pair (17) which are guided by a two-hole alumina ceramics, are pushed to the sample holder and thus provide its exact temperature. As thermal conductivity is poor for insulating samples, the temperature reading of this thermocouple was calibrated in the high temperature regime (300 K - 1000 K) by a thermoelement glued to the surface of a test sample equivalent to those used for the experiments. Low temperatures below are more difficult to calibrate, because the system response upon cooling is much slower than that upon heating due to the limited cooling power. Hence, even once the flow cryostat has attained LN (or LHe) temperature, the actual sample temperature drifts. Calibration was similarly performed, nevertheless the error may be up to 20 K.

### 3.2.2 The VT-AFM

The atomic force microscope designed to work in ultrahigh vacuum and at variable temperature is also of the beetle-type already explained in Chapter 3.1. But even if the setup of our LBD-AFM was quite promising in its performance and handling under ambient conditions, we decided to employ the quite recent piezolever detection technique (c.f. 2.2.2) for the UHV version for the following reasons:

1. The piezolever technique is unsurpassed in its compactness. All optical components are obsolete and no mechanical adjustment is required in vacuum. Tip exchange is comparably simple to realize.
2. The piezolever technique is a quite new technique, hence interesting in itself. Even if low temperature operation exists and a high temperature version of the standard Autoprobe VP (Park Scientific Instruments, Sunnyvale, USA) exists now, the behavior of the piezolevers in a wide temperature range still has to be studied.

A schematic drawing of the AFM is shown in Fig. 3.10. The three outer piezotubes are glued to a disk made of aluminum, which is basically the AFM-head (1). The microscope is resting on ruby balls (2) which provide smooth sliding on the molybdenum ramp of the sample holder. The outer piezotubes (8) are used only for the sample approach or coarse positioning. To extend the scanning range of the inner piezotube, they may also provide an additional offset. The cantilever is carried by a special holder (5), which is attached magnetically to the center piezotube. The original holders of the Autoprobe VP instrument are used, which provide not only mechanical but also electrical contact for the piezolever. As additional feature they have a

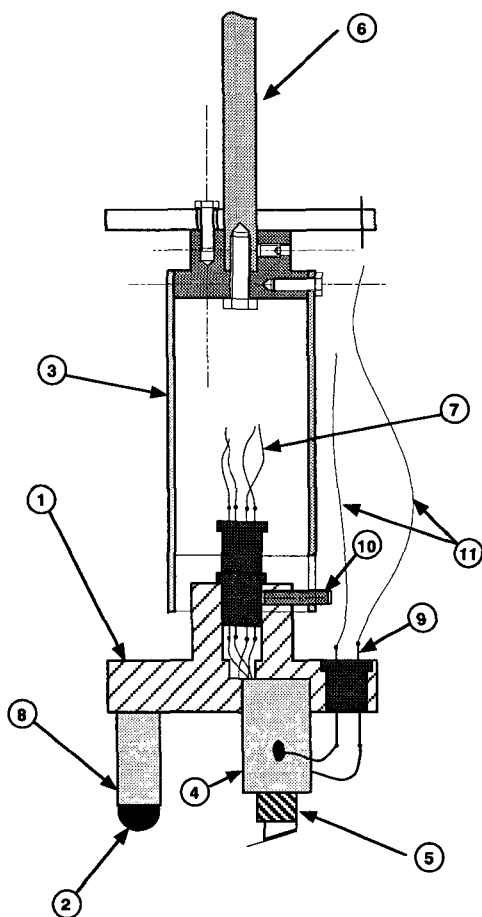


Figure 3.10: Sideview of the UHV-AFM. (1) AFM body; (2) ruby ball; (3) support tube; (4) central piezotube; (5) tip holder; (6) bar of xyz-manipulator; (7) signal wires; (8) external piezotube; (9) connectors; (10) supporting pins; (11) piezo voltage wires.



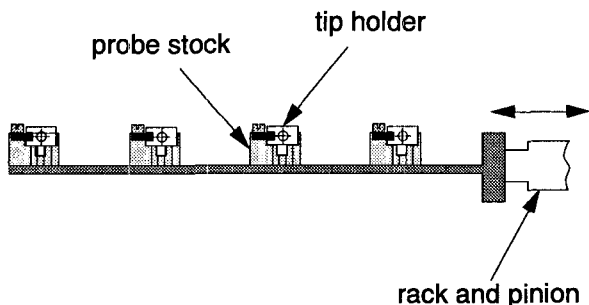


Figure 3.11: Sideview of the probe tip stock.

third contact for a tunneling tip, the AFM thus can easily be used as STM<sup>3</sup>. The center piezotube is used for the scanning movement. As this tube has to fit to the tip holder, its diameter is larger than that of the external ones ( $\varnothing_{ext}=0.125''$  for the external piezos;  $\varnothing_{ext}=0.375''$  for the central piezotube). All piezos are made of EBL No.1 material (Staveley Sensors, East Hartford, USA), because this material has a low change of the piezoelectric coefficients with the temperature. The piezotube is mounted off center in such a way, that the cantilever tip is always centered with respect to the microscope axis. The advantage of always having a centered tip is more important than the disadvantage of the loss in symmetry and hence in temperature compensation capability. The whole AFM is picked up by a tube (3), which is connected via a bar (6) to a x,y,z-translator. This tube shields the signal wires (7) from the piezolever. All other wires ( $50\text{ }\mu\text{m}$ ) (11) end at both sides in tiny plugs which facilitates replacement or unmounting the AFM for repair. Its supporting pins (10) fit into grooves where it is safely kept during tip exchange.

The tip exchange mechanism consists of a rack-and-pinion (r&p) linear manipulator with a probe stock. A groove at the side of the tip holders fits smoothly into a protrusion in the probe stock fixing them in the right position. By means of the r&p drive the tip is positioned under the center piezotube of the microscope which is lowered to pick up the lever. Fine tuning of the microscope position is achieved by its x,y,z-translator.

The control of the instrument is mainly done by the commercial electronics (Park Scientific Instruments). Herein, the signal from the piezolever is measured in a wheatstone-bridge outside the UHV-chamber. Feedback and

<sup>3</sup>The capability of the piezolevers to work as tunneling tip has been demonstrated in [10].

data acquisition are entirely digital. Both operation in contact and non-contact mode is possible. The non-contact mode operation is described in Sect. 2.2.3. The driving signal for the oscillation is superimposed on the z-signal of the center piezotube, whereas less coupling of these signal would be obtained when a supplementary piezoelement would be employed for exciting the cantilever. The scan-range we obtain with our instrument is  $2.4\text{ }\mu\text{m}$  in x- and y- direction and  $0.25\text{ }\mu\text{m}$  in z-direction.

Mechanical stability of the instrument is expected to be comparable to that of the LBD-AFM 3.1.3. The inner piezo tube, which is thicker than the one used in the LBD-AFM should even increase the resonant frequency. However, most comparable measurements performed on different STMs show resonances far below those we observed (1000 - 1500 Hz typically) [40, 56]. Nevertheless, the results obtained with the LBD-AFM are convincing, that this question is not crucial for the performance of the instrument, because excellent resolution capability has been proven.

### Performance and limits

First results we obtained with the AFM served for calibration of the scan range and to explore the accessible temperature range in the variable temperature application.

The temperature range was explored in the limit from 150 K to 450 K. The lower temperature limit was given by noise introduced from the LN-flux; by using LHe this temperature can be reduced further. The high temperature application is expected to be limited only by the piezolevers which stop oscillating at about 600 K [57]. The variable temperature operation in contact mode is only perturbed by the important drift in resistance of the piezolever with the temperature. This drift may even exceed the effect of bending the piezolever. However, as the mass and the heat capacity of the piezolever is low, equilibrium conditions are obtained within minutes. Exemplary data taken at low and high temperature are given in Figs. 3.15 and 5.4.

Unfortunately, we didn't obtain atomic resolution on the MgO(100) at least in the way we succeeded with the LBD-AFM on the KBr(100) surface. This might be for the following two reasons

1. The piezolever technique does not provide a very stable dc-signal. This creates low frequency electronic noise which prevents atomic resolution. In non-contact mode, which is intrinsically a dynamic method, achieving atomic resolution is still very difficult and a time consuming process.

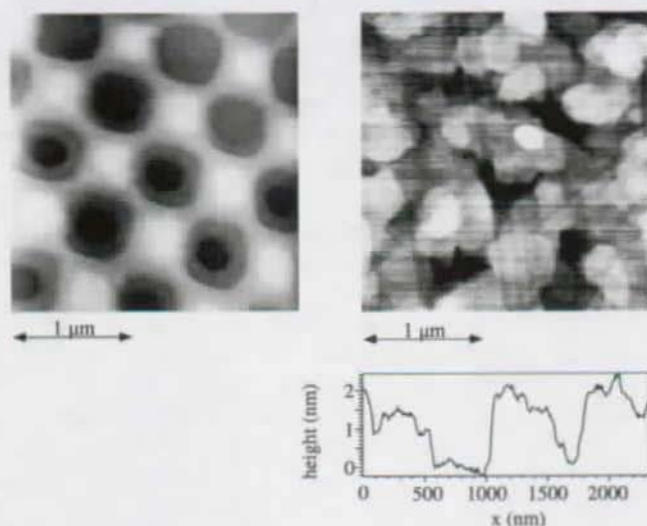


Figure 3.12: a) Calibration grating with a periodicity of  $1\ \mu\text{m}$ . b) Gold film evaporated on mica. Several monatomic steps are visible on the terraces.

2. Low frequency noise can be circumvented by high scanning speed. However, in the ultrahigh vacuum AFM, this approach introduced noise which is probably due to a rattling motion of the beetle-type scan head reported for STM designs [40,56]. Due to its aluminum body, the UHV-AFM is lighter than the LBD-AFM, which may explain the different behavior of these microscopes.

The total noise level was estimated in the following way. The tip was approached under normal scanning conditions and an image was recorded *with the scanner switched off*. The image obtained in this way directly represents the noise in the bandwidth of a typical measurement. From these pictures, the noise level was estimated to  $\approx 1\ \text{\AA}_{\text{rms}}$  in contact mode as well as in non-contact mode. Figure 3.12 a) shows a grating with a periodicity of  $1\ \mu\text{m}$ , which served as a calibration for the  $x,y$  range of the scanner. As this is a large scale scan calibration, error remains due to hysteresis and creep of the piezo tubes.

A gold film evaporated on mica (Fig. 3.12 b)), which is covered with a self assembled monolayer of thiol molecules was used for calibration of the  $z$ -scan. By comparing the different terrace levels, the monatomic step

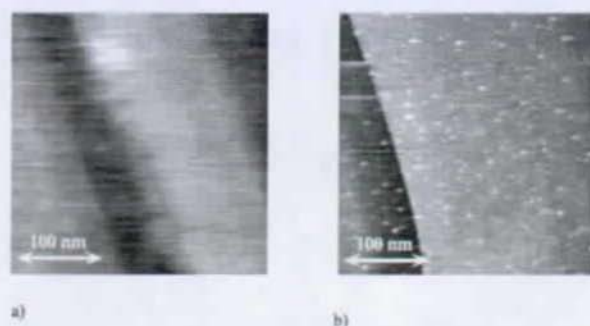


Figure 3.13: Comparison between contact and non-contact mode. a) The contact mode image on the left hand side does not resolve Pd clusters. b) The non-contact image on the right hand side exhibits small Pd clusters (Pd coverage: 0.02 ML).

(height=2.4 Å) can be identified. The calibration was confirmed later on the MgO(100) surface within an error of about 10-20%.

As our microscope is capable of measuring in both contact and non contact mode the application of these modes to the systems examined in the framework of this thesis is investigated.

A contact AFM measurement is not necessarily undisturbing if we take into account, that forces up to several hundreds of nanonewtons may be applied. For the systems of metal clusters on oxide surfaces, the question arises, if these clusters can withstand the forces exerted. Additionally, due to tip-surface interactions the clusters might stick to the tip rather than resting at the sample. The dragging of soft materials by the AFM tip is a well known phenomenon and is often used for so-called nanostructuring experiments with AFM. It is also known that a STM tip plunged into a surface binds to the surface and by withdrawing a neck is created which also takes away material from the surface. In the limit of high forces, this happens in an AFM experiment, too.

For the case of palladium clusters on magnesium oxide, the effect of the tip contact to the surface is shown in Fig. 3.13.

The MgO(100) surface is covered with a small amount of Pd. In the contact AFM image no clusters are resolved. The resolution seems to be obstructed by streaky features in the image. In the non-contact AFM image, however, small Pd clusters are well resolved, because the interaction force between the tip and the sample is drastically reduced. Presumably the lateral force of the tip wipes away the clusters. This phenomenon is demonstrated

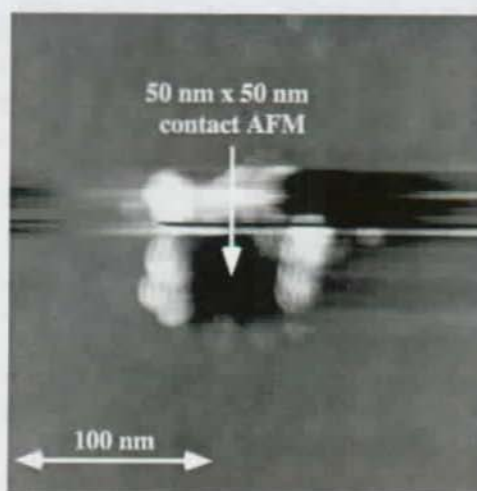


Figure 3.14: 240 nm x 240 nm non-contact image of 0.1 ML Pd on MgO(100). In the center of the image, a 50 nm x 50 nm area was previously scanned in contact mode at an external force of 200 nN.

in Fig. 3.14. In the center of the image, a small area was scanned in contact mode. Afterwards the same area was imaged on a larger scale by non-contact AFM revealing the material deposited in the previous image.

In contrast, the adhesion between the tip and a complete metal film is not high enough to prevent imaging in contact mode, as seen in Fig. 3.15. A Pd film grown at elevated temperature is covering nearly the entire MgO surface. This time, the AFM tip is unable to attack the surface and consequently the film is successfully imaged.

Thus, non-contact mode AFM is the appropriate way to image delicate systems as they are small clusters deposited on metaloxide surfaces. Contact mode is nevertheless useful. There are several reasons why contact mode is still the preferred imaging mode in AFM:

1. Contact mode AFM measurements are faster than non-contact measurements. Typically, the scan speed is several lines per second in a contact AFM experiment, whereas it is one line per second or less in a non-contact AFM experiment. The bandwidth is limited by the feedback of the cantilever oscillation.
2. On sufficiently hard materials with big corrugations contact AFM offers



Figure 3.15: 2 ML Pd on MgO(100) evaporated at 800 K, imaged at 200 K in the contact mode

better resolution. The tip experiences a much steeper force characteristic than in non-contact mode.

3. Contact AFM is much easier to handle than non contact (nc) AFM. The goal of nc AFM is to approach the tip as close as possible to the surface, hence approaching the point of instability. (See fig. 2.5) To work close to an unstable point is not a very comfortable situation. Besides, when employing the piezolevers, it was noticed that their quality has to be yet improved. The production yield is quite low and not every cantilever has really good oscillation characteristics, but they always work well in contact mode measurements.

Finally, the value of the information obtained in a scanning probe microscopy experiment depends strongly on the tip shape and the creation of tip artifacts. There are effects of asymmetric or multiple tips, which can strongly influence the quality of the images. But even a tip that does not exhibit these kind of features, always induces tip shape artifacts. The imaged structure is in fact dependent on the real sample and the tip. This depends strongly on the interaction characteristics. Ideally, only the outmost protrusion of the tip should take part in the imaging process. Atoms further away from the surface should not significantly contribute. In that case, the best image condition is obtained. Unfortunately, in a non-contact AFM experiment the distance dependence of the interaction is quite weak. Hence a large area of



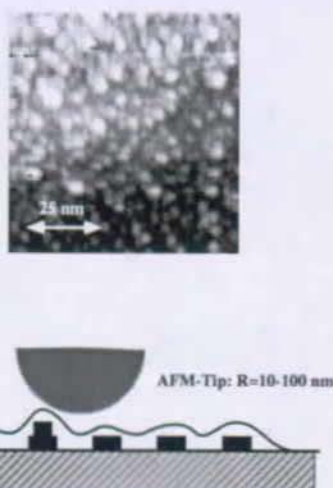


Figure 3.16: Non-contact AFM image of 0.14 ML Pd. Cluster size is overestimated, the whole surface seems to be covered. The situation is represented schematically at the bottom.

the tip interacts with the sample; small features get quite broad and the resolution is limited. This is especially important, if structures with a high aspect ratio should be distinguished in close vicinity because the tip does not penetrate to the surface. The situation is demonstrated in Fig. 3.16, where a low coverage of Pd on the MgO surface is largely overestimated in a non-contact mode measurement. The tip with a minimal specified radius of 100 Å, which may be much larger under real conditions smears out the clusters. This renders information on cluster size and shape difficult to obtain on this scale.

## Chapter 4

# Observation of slip steps on the KBr(100) surface

Heteroepitaxial thin film growth is frequently influenced by strain effects due to the lattice mismatch of substrate and film material. This may favor incommensurate structures or a variety of strain relief mechanisms which reflect the balance of the favorable bonding of the evaporated atoms to specific substrate sites and the unfavorable accumulation of strain in pseudomorphically grown films.

To investigate these phenomena in detail it would be particularly interesting to tune the amount of strain accumulated in a thin film. If it is possible to slightly modify atom positions on a surface, which has been shown for example in the lifting of the chevron reconstruction on Au(111) by straining a thin crystal [58], strain effects on an evaporated film could be studied systematically. However, plastic deformation may prevent from such modifications. The strain exerted on the crystal will then provoke a movement of dislocations to the surface, a process which might be visualized by the appearance of monatomic steps on the surface.

In this chapter a brief overview on the concept of dislocations will be given; thereafter observations of dislocation gliding will be presented followed by an explanation in terms of the slip system active in ionic crystals.

### 4.1 Dislocations

Plasticity of single crystals is one of the macroscopic properties of solids, which is caused by crystal imperfections. For instance, plastic deformations of crystals occur by atomic planes sliding over each other. A new type of crystal defects, the dislocations, were introduced from attempts to reconcile



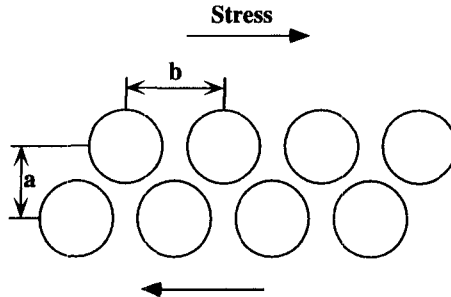


Figure 4.1: Model for the estimation of the critical shear stress for slip motion.

theoretical and experimental facts about the shear stress which is required to enable this sliding. If we consider a perfect crystal lattice, the shear stress that is necessary to slide two atomic planes relative to each other can easily be calculated. It consists of a collective movement of all atoms in a plane to a new lattice position. The one-dimensional situation is represented in Fig. 4.1. Frenkel calculated this shear stress by assuming that a sinusoidal shear force is necessary to move the top row of atoms across the bottom row:

$$\tau = \frac{Gb}{2\pi a} \sin \frac{2\pi x}{b}. \quad (4.1)$$

$\tau$  is the applied shear stress,  $G$  is the shear modulus,  $b$  is the lattice constant in the direction of the shear stress,  $a$  is the spacing of the atomic rows and  $x$  the elongation of the atoms from their equilibrium position. The value of  $\tau$  in equation (4.1) reaches a maximum value during movement from 0 to  $b$ , which is the *theoretical critical shear stress*. It must be overcome in order to initiate the plane slide movement:

$$\tau_{th} = \frac{b}{a} \frac{G}{2\pi} \quad (4.2)$$

Since  $b \approx a$ , this theoretical value is of the order of the shear modulus  $G$ . At the time first experiments on the plasticity of crystals were performed, this was in striking difference to the observed experimental values ( $10^{-4}$  to  $10^{-8}G$ ), which was accounted for by the introduction of the concept of dislocations. Nowadays, nearly dislocation-free crystals exist, exhibiting a strength close to the theoretical value from eq. (4.2) emphasizing again that it is the lack in crystal perfection that was responsible for the low values observed at the time.

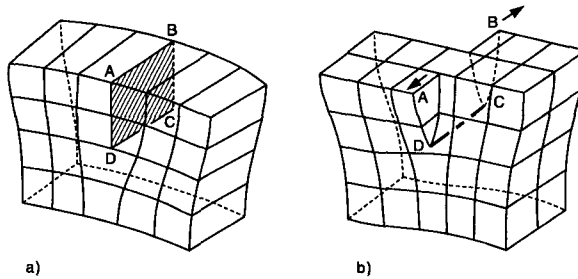


Figure 4.2: a) Representation of an edge dislocation by introducing an extra half-plane ABCD. b) Representation of a screw dislocation.

Other evidence for the existence of dislocations came from experimental observations of crystal growth rates in a supersaturated vapor. At a low degree of supersaturation, growth occurs preferentially at imperfections of the crystal. This leads finally to the creation of perfect terraces. Further growth then has to take place by nucleation on flat crystal faces, which is much more difficult. Nucleation theory predicts that for growth to occur at the observed rates a supersaturation of  $\approx 50\%$  would be required, whereas a supersaturation of only 1% is necessary in an experiment. This contradiction was resolved when it was demonstrated that crystal dislocations result in the formation of steps at the surface which act as preferential nucleation sites, thus facilitating the growth process [59].

## Geometry of dislocations

Two basic types of dislocations exist, the *edge* and the *screw* dislocation. General dislocations can consist of a mixture of different edge and screw dislocations. Only the basic geometries will be addressed here. If we imagine a crystal where a half-plane of bonds between adjacent planes is broken, a new half-plane can be introduced. (See Fig. 4.2) This leaves an imperfection in the crystal at the end of the newly introduced half-plane which disappears at large distances. The imperfection is the emergence of a dislocation. The line introduced by the extra half-plane is called a positive edge dislocation and is symbolized by a  $\perp$ . The opposite, a negative edge dislocation, would be obtained if the extra half-plane is inserted below.

A screw dislocation is obtained if the crystal is moved backwards at one side of the breaking line with respect to the other side, which leads to a

configuration comparable to a spiral staircase. Screw dislocations are defined by the sense of the spiral looking downwards the dislocation line: If the helix advances one plane when a clockwise circuit is done, the screw dislocation is referred to as a right-handed screw dislocation, in the opposite case it is referred to as a left-handed one (see Fig. 4.2).

All types of dislocations are best defined by their Burgers vectors. It is obtained by closing a atom-to-atom path around the dislocation line in the undisturbed part of the lattice. If the same circuit is reproduced in the perfect lattice of the crystal an additional vector, the Burgers vector remains<sup>1</sup>.

A Burgers vector has the following properties:

- For a single edge dislocation it is evident that the Burgers vector is always perpendicular to the dislocation line. For a single screw dislocation the opposite is true, the Burgers vector is parallel to the dislocation line. In general, Burgers vectors may include every possible angle with the dislocation line of a mixed edge and screw character.
- Burgers vectors can never end inside a perfect crystal, but at the surface or at grain boundaries. Thus dislocations must either form closed loops or end in other dislocations. The conditions fulfilled by the Burgers vectors in that case is

$$\sum_1^n b_i = 0. \quad (4.3)$$

The fundamental Burgers vectors possible in simple lattices are the shortest lattice vectors. The dislocation defined by these Burgers vectors are called perfect or unit dislocations. In the case of a bcc lattice it is the vector  $\vec{b} = 1/2a[111]$ , for a fcc lattice the vector  $\vec{b} = 1/2a[110]$ , where  $a$  is the lattice constant.

The dislocation movement sketched in Fig. 4.3 is crucial for the understanding why a relatively small amount of shear stress is sufficient to move a dislocation, which finally deforms the crystal and is responsible for its plasticity. Far away from the dislocation line the lattice is perfect, but closer to it the atoms are considerably displaced from their equilibrium positions. If we consider atom 1, only a small displacement relative to atom 2 and 3,

---

<sup>1</sup>In this way the orientation of the Burgers vector remains undefined. The mostly applied convention is to close the Burgers circuit clockwise, when looking downward the dislocation line from the emerging point. An exception is the case when looking at several dislocations, which meet in a node. In that case, the circuit is closed clockwise when looking outward the nodal point. This is necessary in order to fulfill equation (4.3).

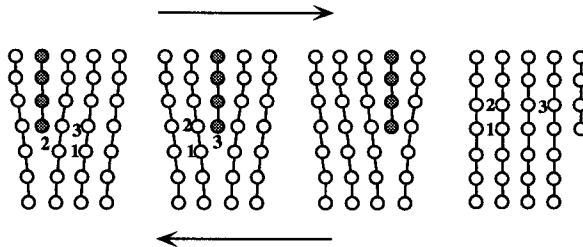


Figure 4.3: Movement of a dislocation due to the shear stress indicated by arrows.

hence a very small shear stress compared to the situation in a perfect lattice, would change the position of the extra half-plane, which is emerging initially at atom 2 and afterwards at atom 3. Consequently, if this occurs, the dislocation moves by one atomic row. This movement can go on until it ends at a surface, a grain boundary or another dislocation. This movement is called slip of the dislocation, the plane in which it takes place is referred to as the slip plane. The importance of the Burgers vector as crucial parameter of a dislocation is seen in this movement: The neighboring atoms (1 and 3) are displaced with respect to each other when the dislocation glides past by one Burgers vector. The example additionally nicely reflects that *the movement of one dislocation produces a surface slip step equal to the Burgers vector in the direction of the dislocation line*. This enables the indirect evidence of bulk dislocations in a crystal by the steps created at the surface when subjected to shear stress.

## Dislocations in ionic crystals

Potassium bromide is an ionic crystal of the sodium chloride structure. The lattice is best described as a fcc-structure with a basis of the  $K^+$  ion at the  $\{0,0,0\}$  position and the  $Br^-$  ion at the  $\{1/2,0,0\}$  position. The shortest lattice vector is  $1/2[110]$  and this is the Burgers vector of the dislocations responsible for slip. The principal slip planes are the  $\{110\}$  planes. Slip motion is also observed on  $\{100\}$  planes and after high stresses and at high temperatures on  $\{111\}$  and  $\{112\}$  planes. The ideal edge dislocation in a KBr single crystal can be represented similarly to the simple dislocation of Fig. 4.2. In this case, however, the “extra half-plane” consists of two planes, one of positive ions and a second of negative ions (Fig. 4.4). Defects like vacancies or interstitials in ionic crystals generally exhibit special effects,

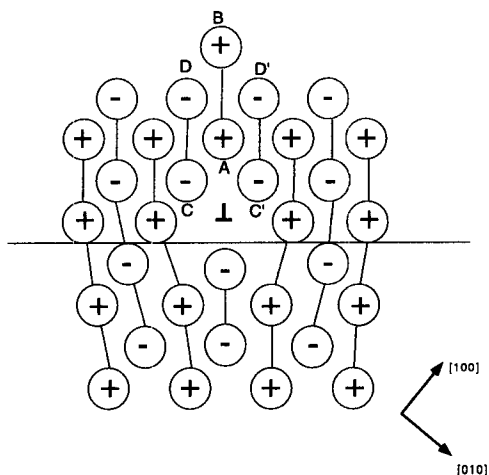


Figure 4.4: The “extra half-plane” consists of two planes A-B and either C-D or C'-D' in the case of ionic crystals of the rocksalt structure.

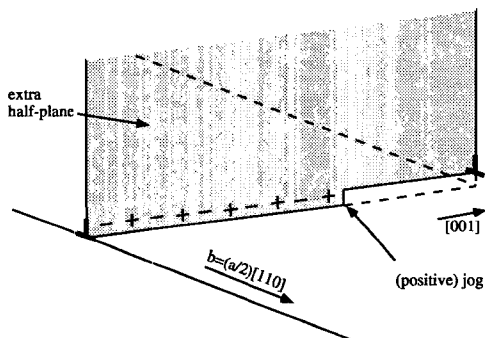


Figure 4.5: Positive jog in an edge dislocation on a  $(110)$  glide plane.

because electrostatic effects occur. Even if the  $1/2 [110] \{110\}$  dislocation is intrinsically uncharged, because the dislocation line is formed of alternating positive and negative ions it will become charged if defects like jogs (Fig. 4.5) occur in the dislocation line. The excess charge of a jog that ends in a positive ion is  $q = e/2$  and  $q = -e/2$  for a negative ion.

The emergence point of the dislocation on a  $(001)$ -type surface is charged,

too. Intuitively this is understandable since in its vicinity two rows of ions of alternating signs merge in ions of the same sign (rows C-D and C'-D' in Fig. 4.4). Careful examination of this geometry leads to a charge of  $q = -1/4e$  at the emergence point. On glide motions, the effective charge rests unchanged and moves along the slip plane.

Intrinsically charged dislocations may exist as well, e.g., if the usual edge dislocations with the Burgers vector  $1/2[110]$  ends in a  $\{111\}$  plane. A review of electrostatic effects on dislocations in ionic crystals is given in [60]:

1. In an ionic crystal, the ionic conductivity increases after deformation. This observation was explained in terms of excess charge carriers, which are in particular vacancies, formed as a result of intersection of dislocations.
2. During plastic deformation a transient electric current is produced. This current is attributed to motion of charged dislocations.
3. A crystal which is already bent can be further deformed by applying an electric field. Dislocations are displaced under the influence of the field.
4. The velocity of dislocation motion is found to be influenced by an electric field. Depending on the orientation of the field and the applied shear stress, the dislocation can be accelerated or decelerated.

If an ionic crystal of sodium chloride structure is subjected to a  $\langle 100 \rangle$  compressive strain, slip occurs at the beginning at one or more of the slip systems shown in Fig. 4.6, where the dislocation line is not parallel to the shear stress. In general, initially only one system is preferentially activated. Dislocation multiplication takes place to produce roughly the same number of dislocations moving in opposite directions. Additional slip systems become activated at a second stage at stronger deformations. The two slip systems of the  $\{110\}$  type that are parallel to the compressive strain do not contribute to slip of the dislocations. Finally, at higher deformations slip appears on  $\{100\}$ ,  $\{111\}$  and  $\{112\}$  planes, of which  $\{111\}$  is the least favorable due to the high electrostatic energy necessary for moving adjacent planes, which contain ions of opposite charge. As mentioned above, a moving dislocation produces a surface slip step equal to the Burgers vector in the direction of the dislocation line. Thus upon compressing the crystal, slip steps with the same direction as the dislocation line should trace the dislocations responsible for plasticity at the surface.

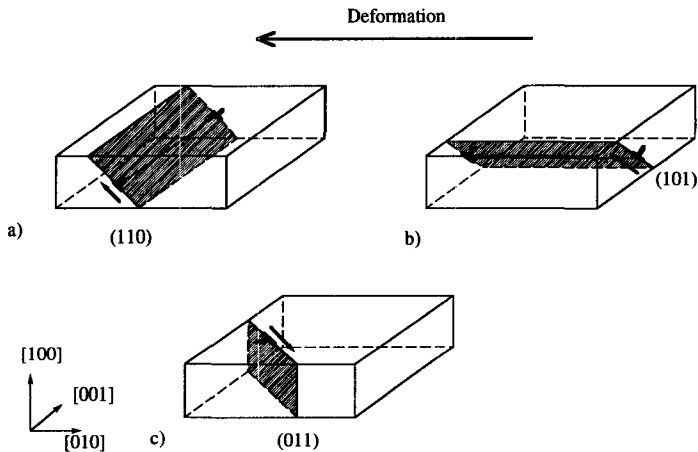


Figure 4.6: The six planes in which slip may occur (only one of the two perpendicular planes in each system is shown): a) surface steps will be obtained, b) no resolved shear stress with the given deformation direction, and c) no steps at the (100) surface will be obtained.

## 4.2 Observation of dislocations

At the time when the concept of dislocations was introduced to explain experimental observations in crystal plasticity, no experimental methods existed to observe dislocations and to study their properties. Later on, methods for direct observation were developed such as decoration, etching, x-ray diffraction and electron microscopy [61]. These methods made detailed observations of dislocations in all kind of materials possible and, by now, the geometry and physical properties of dislocations in metals, semiconductors, superconductors and ionic crystals are well examined [62]. To make slip steps visible on ionic crystals until now methods like optical microscopy or electron microscopy have been used [61, 63]. The first method suffers from its poor lateral resolution, even if monatomic steps can be resolved by interferometric methods; the second one requires more experimental effort: The steps must be decorated with gold, this structure has to be covered by carbon and afterwards the substrate must be dissolved for examination in an electron microscope. Furthermore, this procedure does not allow one to follow the modification of the surface while increasing the deformation. The newly developed scanning probe microscope techniques should be ideal for examina-

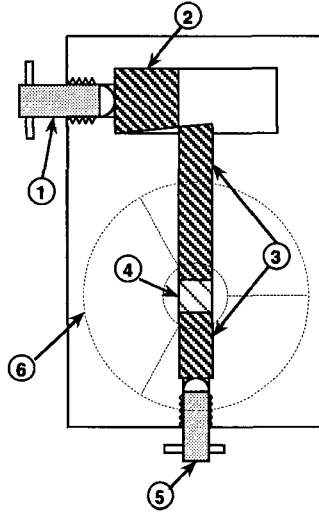


Figure 4.7: The strain stage: (1) fine adjustment screw, (2) inox wedge, (3) inox bars, (4) sample, (5) coarse adjustment screw, (6) ramp for microscope approach.

tions of slip steps on single crystal surfaces. Atomic force microscopy (AFM) and scanning tunneling microscopy (STM) are capable of resolving steps of monatomic height easily with very high lateral resolution. STM experiments have been performed on Si(111) [64] that reveal the appearance of slip steps on the surface due to the application of tensile stress at high temperatures, but no systematic examination of the dependence on the deformation has been reported. Low energy electron microscopy (LEEM) is also capable of resolving atomic steps. Slip steps occurring on the surface due to heating to 800°C and subsequent cooling have been observed and explained in the slip system of Si(100) and Si(111) samples [65].

Here we report observations of slip steps on KBr(100) as a function of the crystal deformation. In situ AFM provides a straightforward method for the observation of dislocation slip from the bulk.

The homebuilt “beetle-type” atomic force microscope used in this experiments is described in Sect. 3.1. A special strain stage was designed to apply the deformation to the sample. The setup of this stage is shown in Fig. 4.7. The sample is held between two inox bars. The first one (3) can be displaced by the screw on the bottom (5) to allow for coarse fixing of the sample. A



precision screw (1) moves the inox wedge (2), which provides a 1:20 transmission for the second bar (4), which applies the strain to the sample (7). The typical helical ramp (6) for the coarse approach of the microscope is fixed on top of the strain stage. The sample area is freely accessible from below for adjustment of the sample position in height and to avoid other constraints to the crystals then those from the two bars. The deformation of the crystal is measured via the precision screw. The minimum value, which can be obtained reproducibly is as small as  $dl/l = 1 \times 10^{-3}$  corresponding to a  $45^\circ$  turn of the screw. The maximum deformation which can be applied is  $dl/l = 0.1$ . To avoid contributions of the strain stage to the actual deformation of the crystal, it is entirely made of inox, which is several orders of magnitude stronger than the crystal. The sample (5 mm x 5 mm x  $\approx 2$  mm) is a (100) oriented KBr crystal cleaved from a bar (Korth Kristalle GmbH, Altenholz, Germany). It is mounted to the sample holder and gently fixed by the coarse adjustment. Then the surface is examined by AFM. If the terraces observed are large enough, it is used for further examinations. The crystal is deformed by turning the precision screw (1). During this deformation the microscope has to be lifted several micrometers, because an expansion of the crystal in z-direction perpendicular to the deformation is observed and may cause severe damage of tip and sample when resting in contact. Furthermore, after every deformation a certain relaxation time (typically several minutes) was necessary before AFM imaging was possible, presumably since charges transported to the surface by the moving dislocations have to be balanced.

## AFM observations on KBr(100)

Figure 3 shows a series of AFM-measurements done in the deformation regime  $dl/l=0 - 10^{-2}$ . In the first image terraces of 1 - 2  $\mu\text{m}$  can be observed, separated by a step of several atomic heights. This is typical for a well cleaved ionic crystal, but also terrace widths of only 200 - 500 nm are observed. It has been found that the surface quality strongly depends on the cleavage. Apparently, already during cleavage a very high and undefined stress is exerted to the sample. The observed steps are hence attributed to the same mechanism revealed later, when deforming the crystal in a controlled manner. It is unlikely that a misalignment is responsible for these initial steps, because there exist alternating regions with upward and downward steps. (Deformation experiments were only performed on surfaces with a high initial quality similar to those in Fig. 4.8 a)).

At a deformation of  $5 \times 10^{-3}$  monatomic steps in the [001] direction ap-

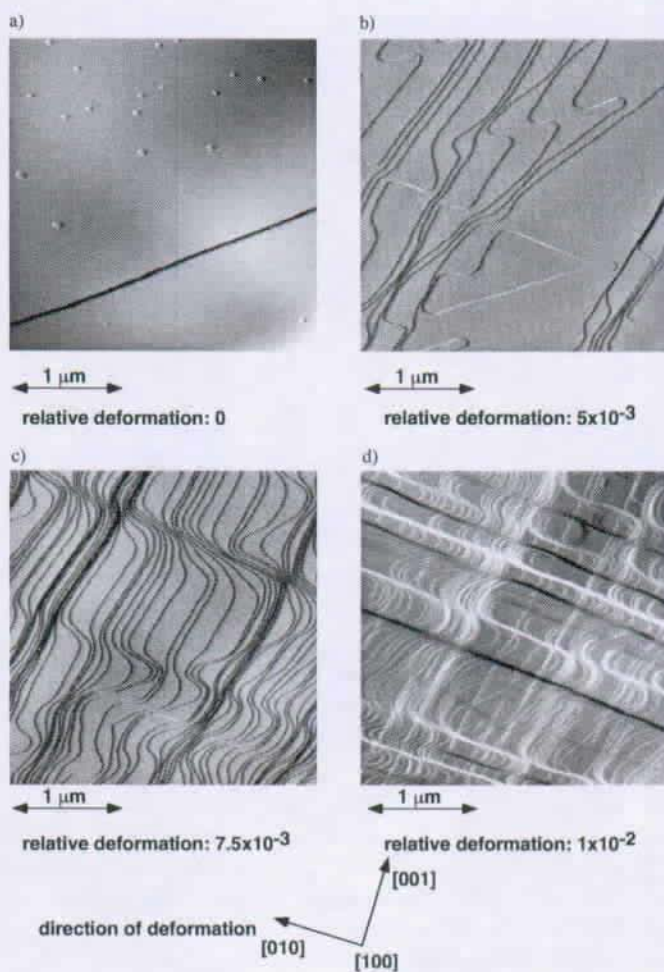


Figure 4.8: The (100) surface of KBr at different stages of crystal deformation.

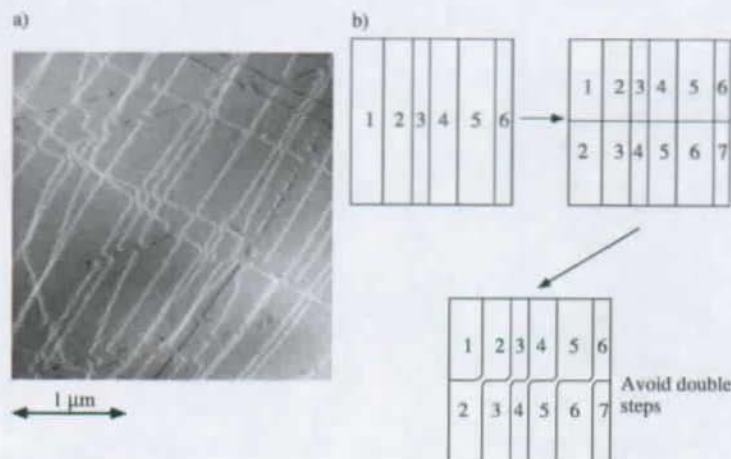


Figure 4.9: a)  $2.7 \mu\text{m} \times 2.7 \mu\text{m}$  image of KBr(100) at a relative deformation of  $5 \times 10^{-3}$  showing the absence of crossing steps. b) Schematic process of terrace coalescence [65].

pear, which is the direction perpendicular to the deformation. This effect becomes more pronounced if the deformation is increased to  $7.5 \times 10^{-3}$ . In conjunction with the increased step density, a typical 90 degree bending of steps occurs. The origin of these curved steps may be the slide of jogged dislocations. The jog would produce a kink in the steps, when the dislocation attains the surface. However, the steps are not curved from the beginning, hence a different process is suggested: When  $\{010\}$  steps are created followed by coalescence of terraces of equal height the observed pattern can be obtained (Fig. 4.9): For two crossing steps a height difference of two monatomic steps occurs at the intersecting point. If the mobility of surface atoms is high enough, material is transported from the highest to the lowest level, thus avoiding double steps. Similar processes have already been observed for example on Si(100) [65]. At the highest deformation applied, the maximum terrace width decreases to 50 nm - 100 nm and a significant step bunching occurs. Terrace coalescence results now in even circular steps and reaches a limit, because a minimum terrace width seems to be necessary for this process. Up to this deformation, the predominant formation of  $\{001\}$

and (less)  $[010]$  steps is observed. Nevertheless, strong deformation makes the formation of  $[011]$  steps possible. This is visible in the first two images, where the observed  $[110]$  steps are attributed to the high strain which may occur during cleaving.

This step creation thus confirms the glide of existent or created bulk dislocations to the surface of the KBr-crystal. As shown in Fig. 4.6, edge dislocations are expected to glide preferentially on the  $(110)$  - type planes which intersect the  $(100)$  surface in the  $[001]$  direction. This is the direction of most of the steps initially created during deformation. The observed steps in the  $[010]$  direction are more difficult to create: The model in Fig. 4.6 demonstrates that the dislocations, which would produce these steps upon glide, would not directly sense any resolved shear stress components. However, there might exist a small resolved shear stress on the  $(101)$  plane due to a possible misalignment of the setup, which enables glide on this slip system, too.

The question arises, if this mechanism is the only possible way to create the observed steps or if, e.g., the quite efficient mass transport suggested for coalescence may be responsible, too. It is well known that alkali halides are soluble in water and thus attacked by the water film present at all surfaces under ambient conditions, which may result in a step movement [66, 67]. In our experiments we observed that small islands, formed upon cleaving (Fig. 4.8 a)) disappear after several scans due to their mobility and tip - sample interaction. However, this is a very improbable reason, because we checked the sample on the same timescale without deformation and no drastic change in the surface morphology was observed.

In conclusion, the experiments demonstrate the observation of deformation effects on ionic crystals. The role of dislocation glide has been proven by direct observation of the slip steps at the  $(100)$ -surface. In this context it would be quite instructive to compare the results with experiments on crystals of a different lattice structure or on thin films to observe their behavior. Unfortunately only few suitable surfaces for AFM examinations under ambient conditions exist, so experiments under ultrahigh vacuum are suggested.



# Chapter 5

## The MgO(100) surface

In this chapter, the procedure we developed for the preparation of MgO(100) surfaces, well-suited for thin metal film deposition, will be outlined. For this purpose, firstly an overview of the different approaches to this problem known in literature will be given. Secondly, the procedure employed here will be explained and their advantages and drawbacks discussed. Finally, the influence of charging effects on the highly insulating MgO-crystal is explained on the basis of our AFM experiments.

### 5.1 Characterization of MgO(100)

Magnesium oxide crystallizes in the sodium chloride structure (Fig.5.1). This structure is best described by a cubic elementary cell with the  $\text{Mg}^{2+}$ -ion at the  $\{0,0,0\}$ -position and the  $\text{O}^{2-}$ -ion at the  $\{1/2,0,0\}$ -position. The lattice parameter for MgO is  $a=4.24 \text{ \AA}$  with the classical values of the bulk ionic radii

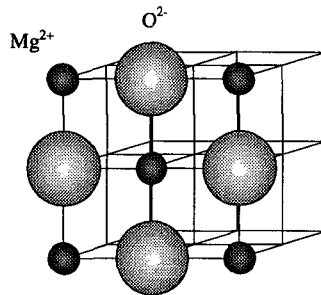


Figure 5.1: The sodium chloride structure of MgO

of  $r_{\text{Mg}}=1.46 \text{ \AA}$  and  $r_{\text{O}}=0.66 \text{ \AA}$  [68]. The cleavage plane of the MgO crystal is the (100) plane which is thus the best accessible surface for surface science experiments and consequently the most examined one. The (100)-surface exhibits a square lattice with alternating Mg- and O-ions. The distance between equally charged ions in the  $\{110\}$  direction is  $a/\sqrt{2}=2.91 \text{ \AA}$ . The height of a cleavage step corresponds to half of the lattice constant, which is  $2.06 \text{ \AA}$ . The MgO(100) samples employed for the present study were cleaved from a  $\varnothing 22.5 \text{ mm}$  bar (Kelpin Kristallhandel, Leimen, Germany). The major impurity is calcium at a concentration of 300 ppm or less.

It was discovered quite early that alkali halides allow epitaxial growth of numerous metals (Pd, Ag, Au ...) in a moderate vacuum, but not under ultrahigh vacuum conditions. MgO in contrast favors epitaxial growth even under UHV, which initiated extensive examination of this substrate [69]. These studies were performed either on surfaces which were cleaved in air and treated afterwards in UHV or on *in situ* under UHV cleaved crystals. Few comparisons between these methods are reported as mainly experimental restrictions hindered cleavage in UHV, thus care has to be taken when the quality of air-cleaved crystals is overestimated.

LEED measurements at MgO(100) UHV-cleaved crystals were performed as early as 1967 [69]. The suitability of the surface for thin film growth was examined over a wide temperature range. A sharp LEED ( $1\times 1$ ) pattern was observed and no degeneration with the beam exposure occurred. A more detailed LEED I/V study was carried out by Welten-Cook and Berndt [70] with the aim of verifying predicted relaxation or rumpling of the surface. They claim a high stability of the surface against exposure to the electron beam and ambient conditions. Consequently, they utilized an air-cleaved crystal that was cleaned by several annealing cycles at  $800^\circ\text{C}$  with a total exposure of  $6\times 10^{-5}$  Torr of oxygen to remove carbon contamination. They circumvented the problem of charging the sample at low energies. For electron energies exceeding 100 eV a sharp LEED pattern was obtained, which disappeared upon lowering the energy, due to charging of the surface. It was discovered that short 10 ms pulses at 200 eV were sufficient to decharge the surface and enable a 10 ms measuring time at lower energies. Apparently, the increase of the secondary electron yield at higher energies is responsible for this effect. The LEED data indicate a rumpling of 2% of the surface without any relaxation.

Further LEED investigations by He *et al.* [71] similarly reported a good surface structure. They employed an air-cleaved crystal that was annealed in UHV at  $340^\circ\text{C}$ . Urano *et al.* [72] finally compared a surface that was prepared

by cleaving a MgO bar in UHV with an air-cleaved crystal. The air-cleaved crystal was annealed in UHV at 800°C in an atmosphere of  $10^{-5}$  mbar oxygen until the carbon peak in Auger electron spectroscopy disappeared. They reported that both kinds of surface preparation resulted in a comparable surface quality and observed an outward relaxation of less than 2.5% without any rumpling.

Summing up these results, LEED experiments do not show a significant difference in surface quality for either UHV-cleaved or air-cleaved and subsequently UHV-treated crystals. The degree of relaxation and rumpling remains unclear, because these effects seem to depend on the exact preparation method and very contradictory results were obtained. For example, a sample that was heated to 1000°C in air and subsequently at 120°C in phosphoric acid showed a 15% inward relaxation in an ICISS experiment [73] in strong contrast to the LEED results. Nevertheless, in none of these experiments evidence for a surface reconstruction or faceting was found.

As LEED is insensitive to local defects and chemical modifications of the surface, other techniques have been employed to obtain this information. Helium atom diffraction experiments are very sensitive to local surface defects, because the elastically scattered intensity depends strongly on the surface quality. Rieder [74] performed such measurements with air-cleaved crystals and noticed the quite low elastically scattered intensity of 10%. He proposed that a high number of irregularities like steps, kinks and point defects were responsible for this observation and did not obtain any improvement after heating the sample at 450°C for several minutes.

Much better results were obtained in a more recent study of UHV-cleaved samples that were annealed in an oxygen atmosphere. The experiment revealed a sharp specular peak with an intensity of 35% [75]. A deterioration within a time-scale of several hours was observed and the initial surface quality can only be partially restored by an oxygen treatment. Hence the authors attribute carbon contamination to the decrease in elastically scattered intensity.

This observation is confirmed by a comparative study of air-cleaved and UHV cleaved crystals by Duriez *et al.* [76]. They employed helium diffraction as well as surface decoration and Auger electron spectroscopy. The helium diffraction results confirmed those cited before. A specular intensity of about 35-40% is obtained on the UHV-cleaved crystals. For the air-cleaved crystals, the scattering is almost completely diffuse, if they are not cleaned by an annealing in oxygen atmosphere. The number of defects is estimated by means of the surface decoration technique. On this behalf, palladium and



gold is evaporated onto the surfaces. Under certain conditions, these metals show a strong tendency to be trapped at defects like vacancies or steps. A number density of point defects on the terraces, which was roughly higher by a factor of ten for the air-cleaved compared to the UHV-cleaved samples, was deduced. The step density varied greatly on both types of samples, so it does not depend significantly on the preparation method.

The drastic increase of the number of point defects on a MgO(100) surface upon air exposure was also confirmed by infrared spectroscopy [77, 78]. The observed absorption peaks of CO<sub>2</sub>, used as a probe molecule, are extremely sharp when a freshly UHV-cleaved crystal serves as a sample. The peaks disappear on a timescale of several hours. At the same time, IR-absorption spectra of CO<sub>2</sub> probe molecules on an air-cleaved and an annealed surface (12 hours at 1123 K) are by far broader, indicating a smaller degree of order of the molecules on the surface. Hence it was inferred that these samples did not exhibit large defect free surface areas.

The origin of the defects and the carbon contamination, which are observed in almost every experiment dealing with air-cleaved crystals, is the attack of water vapor and dissociative chemisorption of CO<sub>2</sub>, respectively. The influence of water and CO<sub>2</sub> on MgO(100) surfaces has been studied by Onishi *et al.* [79]. Their UPS-measurements on samples exposed to 1000 L H<sub>2</sub>O at 298 K revealed the formation of hydroxides. They concluded dissociative chemisorption of H<sub>2</sub>O. This reaction takes place at the oxygen and magnesium sites of the perfect surface as well as at sites of lower coordination. The OH<sup>-</sup>-Ions bind to the magnesium and can be removed by heating to at least 1000 K [80]. CO<sub>2</sub> exposure at the same amount revealed the formation of CO<sub>3</sub><sup>2-</sup>-Ions by comparing the UPS-spectra with known sodium carbonate spectra.

Very recently, it has been proven that air-cleaved and oxygen annealed surfaces nevertheless provide excellent substrates for thin film deposition [81]. XPS-measurements confirmed the complete removal of the carbon contamination layer (less than 0.005 monolayers) and a layer-by-layer growth mode of silver was obtained.

There are limits to the annealing of the MgO crystal. The most important factor is that calcium segregation to the surface sets in at about 900°C. Calcium is the most prominent impurity in MgO crystals, standard material contains about 200-300 ppm<sup>1</sup>. This phenomenon has been observed by REELS, REM [82, 83], AES [84, 85] and low energy helium scattering [84].

---

<sup>1</sup>MgO crystal with only 40 ppm or less can be obtained, but are not commercially available.

The temperature of the onset has been estimated to be 900°C by the appearance of calcium in the AE spectra. REELS data indicate that calcium then starts to segregate preferentially to step sites, where the Ca/O ratio is about a factor of two higher than at the terraces. Finally, this process leads to the destruction of  $\langle 010 \rangle$ -type steps and produces steps running in  $\langle 011 \rangle$  directions, which was observed by REM. Furthermore line-like features running in this direction are observed. While the exact reason for these features is unclear, a strain relief mechanism as possible origin is suggested [82]. At higher temperatures (above  $\approx 1000^\circ\text{C}$ ) the amount of calcium at the surface is reduced again. Thus, the high-temperature annealing induces calcium segregation at the beginning, whereas by a further temperature rise magnesium segregation starts to dominate. This has been explained by an equilibrium segregation model of McCune and Wynblatt [84], who found additionally a decrease of the oxygen peak due to sputter erosion and electron bombardment damage, an observation which is confirmed by Lee *et al.* [86], who observed a decrease in oxygen intensity in AE spectra after prolonged argon ion sputtering.

Recently, AFM-experiments on the MgO(100) surface were performed. The first study, which was carried out under a dry nitrogen atmosphere, revealed the atomic lattice of the surface but did not notice any contamination on a larger scale [87]. The following study, performed under ambient conditions, showed a surface with a high step density, comparable to that obtained by the surface decoration experiments [88]. After storage under ambient conditions for a longer period a large number of huge islands was observed. An experiment with an air-cleaved and subsequently annealed crystal in UHV was reported in [89]. The authors found a stepped but clean surface, with the striking observation that no sharp step pattern with flat terraces was obtained. Furthermore, atomic resolution, which was routinely achieved on other substrates, was not obtained on MgO. A study, which compares polished to acid-etched and oxygen annealed MgO(100) surfaces concludes from contact AFM measurements, that the second preparation method provides suitable samples. Nevertheless, the steps at the surface are not very straight but exhibit many kinks and are not very sharp as well. The terraces reveal a quite high rms roughness of 1.3 Å. In contrast to the work cited above, this group succeeded in atomic scale imaging of the  $\text{O}^{2-}$ -ion rows with a spacing of 3 Å [90].

These many results are to some extent contradictory, nevertheless several general implications can be deduced: First of all, the best surface preparation method is the cleavage *in-situ* under ultrahigh vacuum conditions. If air-

cleaved crystals have to be used for experimental reasons, these samples have to be post-treated in ultrahigh vacuum. The cleavage must be performed under the flow of a dry, inert gas and annealing cycles under a high pressure ( $\approx 10^{-5}$  mbar) of oxygen have to be added until no carbon contamination can be detected. The temperature during annealing should not be excessively high, due to the onset of calcium segregation above 900°C. The effect of high-temperature annealing on the surface structure remains still unclear.

## 5.2 Preparation of the MgO(100)-surface

As there is no sample cleavage mechanism inside our UHV-system, an appropriate preparation procedure for air-cleaved crystals had to be found. Contamination-free surfaces with a low number of defects and a terrace width of at least  $\approx 50$  nm for the subsequent metal deposition experiments had to be prepared. At the beginning, the MgO bar was cleaved in air by a knife or a tungsten carbide blade and the sample was introduced into the load-lock. This procedure took a few minutes until starting the pumping; after 1 hour, a pressure below  $1 \times 10^{-6}$  mbar was obtained and the sample was transferred to the UHV chamber. Macroscopically, the surface revealed a high number of curved steps with a radius of curvature larger than the radius of the sample, which started at the cleaving point. The two other  $\{100\}$  directions, apart of the one the axis of the bar was oriented to, were identified by perpendicular cleavage and used for a definite deformation direction during cleavage. Randomly oriented cleavage, however, did not significantly change the microscopic quality of the surfaces with respect to those cleavage attempts where the direction was oriented along one of the  $\{100\}$ -directions. On the microscopic scale, these surfaces showed a high number of steps (distance 10 nm to 100 nm) running mainly in one direction. Very rarely, perpendicular steps were observed. The origin of these steps is difficult to prove, but it seems reasonable that the same mechanisms as for the cleavage of KBr(100) (movement of dislocations rather than miscut steps: see chapter 4) are responsible. The by far higher step density on the MgO(100) surface can be explained due to the higher strength of MgO and the higher concentration of impurities implying a higher number of dislocations in the bulk compared to KBr. Thus, a higher stress is necessary for cleavage and the movement of dislocations is simplified.

In the contact AFM images the terraces appeared to be clean. Auger electron spectra, however, revealed a significant carbon contamination of one to several percent of a monolayer. For further examination the following

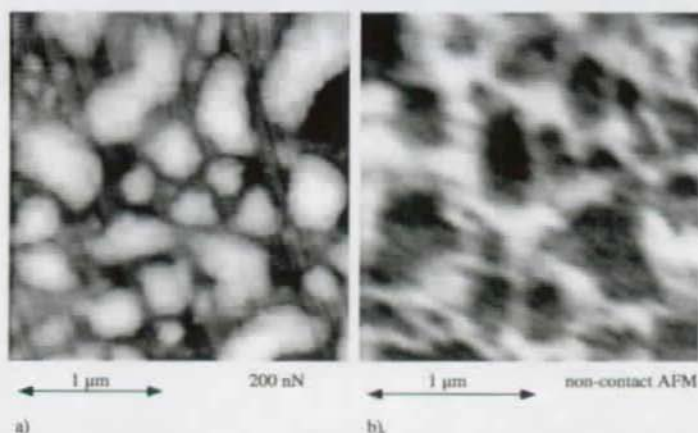


Figure 5.2: a) Heavily contaminated MgO(100) surface after several days of storage in air. b) Same surface after cleaning procedure by annealing in oxygen for 165 min ( $p_{O_2} = 1 \times 10^{-6}$  mbar).

improvements were determined: Firstly, we attempted to reduce the number of steps via high-temperature annealing, and secondly, reduction of carbon contamination by annealing in oxygen.

The first objective was approached by an *ex situ* preparation as was reported for alumina ( $Al_2O_3$ ) [41]: The sample was heated to  $1500^\circ C$  in an oven in air. Unfortunately, the surface quality did not improve, in contrary it became rougher and calcium segregation was observed by AES. The step density obtained by the cleavage hence had to be accepted for the experiment. For the second objective, at first a sample with high carbon contamination was prepared by exposure to ambient conditions for several days. This enabled us to visualize the contaminations in an AFM measurement, which was impossible at a lower contamination level. On the heavily contaminated surface, large islands are visible which are several nanometers in height and are associated with the contamination. (See 5.2a) As effective carbon removal was reported by heating the surface in an oxygen atmosphere several annealing cycles were applied. Oxygen was dosed via the gas doser at a chamber background pressure of  $1 \times 10^{-6}$  mbar. Estimating an overpressure due to the doser of about 10 - 100, the partial pressure over the sample was maintained at  $10^{-5}$ - $10^{-4}$  mbar. The sample then was heated to 750-800 K until AES confirmed complete carbon removal. For the heavily contaminated surface,

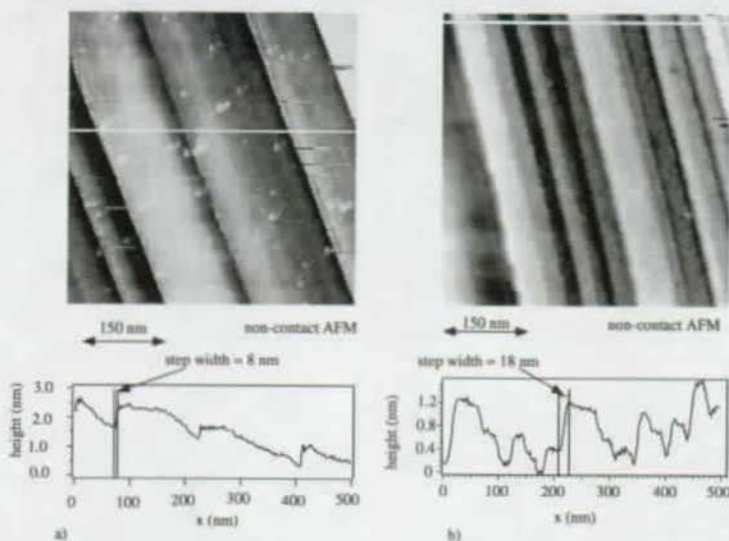


Figure 5.3: a) A  $\text{MgO}(100)$  surface after cleavage under argon imaged in non-contact mode AFM. A representative line scan is depicted at the bottom. b) Same surface after heating in oxygen atmosphere.

this procedure took 165 min. Subsequently, the sample was imaged by non-contact mode AFM to avoid removal of residual contamination by the tip. The result is shown in Fig. 5.2 b). Apparently, the large islands of carbon contamination were removed effectively. Now, depressions are visible instead and we conclude, that these grooves appeared due to an etching process while removing the carbon. Upon heating in the oxygen atmosphere, carbon was probably reactively desorbed leaving behind a clean but structurally damaged surface. As this damage is also expected, even though to a smaller extent, if the sample is less contaminated, the exposure to air has to be avoided. Thus the following crystals were cleaved in a glove bag, which was closely fit to the load-lock. Before cleaving, this bag was purged at least five times with argon gas by pumping via the load-lock. This ensured best cleanliness from ambient gases for both the glove bag and the load-lock. The sample was then introduced under argon atmosphere. This procedure resulted in a surface, where nearly no contaminations were visible in the AFM-image and the corresponding AE spectra indicate C-free surfaces (Fig. 5.3a)). As can be seen in the cross section below the image, the surface exhibits a sequence of

upward steps (from the left to the right) of several monatomic layers in height (between 3 and 5), followed by monatomic downward steps (height 2.05 Å). The average step distance is about 20-50 nm and only few contaminations are visible.

The best preparation cycle, if UHV-cleavage is not possible, thus would be to cleave samples in an inert gas atmosphere and apply a cleaning procedure in UHV. In our experiments, this cleaning was standardly performed at a temperature of 750 K in a  $10^{-5}$ - $10^{-4}$  mbar oxygen atmosphere for about 30 minutes. A sample cleaned by this procedure is shown in Fig. 5.3b). For the surfaces prepared in this manner the observation remains that the terraces do not appear to be perfectly flat, as we have seen, e.g., in the case of the KBr(100) surface. Furthermore, some of the step edges seem to be larger than would be expected due to the finite radius of the tip (10 nm - 100 nm). As mentioned above, the same effects appeared in the experiment of Abriou *et al.* [89] and Perry *et al.* [90], where monatomic steps are imaged with  $\approx 20$  nm in width, which corresponds to a tip radius of about 1000 nm, which is by far too large for a standard tip. The step enlargement was found independently from the chosen tip. The origin of this effect remains unclear, but as it appears exclusively on annealed surfaces, a structural change at the steps is suggested even at the comparably low temperature of our annealing experiments. Alternatively, the process of contamination removal can be responsible itself. Chemisorption may preferentially start at defects and step sites; the removal of these species may have an impact on the surface structure at these places. To elucidate this phenomenon, it would be helpful to compare the results obtained on an air-cleaved and a post-treated MgO(100) sample with results obtained on UHV-cleaved crystals.

### 5.3 Charge phenomena on MgO(100)

Surfaces prepared in the described manner were subsequently used for thin film deposition. Imaging of the clean surface, however, sometimes posed problems which are attributed to electrostatic effects. Immediately after cleavage and sample introduction successful AFM measurements were impossible. In non-contact mode AFM a behavior typical for long-range interaction was observed<sup>2</sup>. Presumably, charging effects due to the sample cleavage are responsible for this phenomenon. As we have seen in section 4.1, defects like

---

<sup>2</sup>The resonant frequency starts to shift at large distances before any surface features can be detected (several micrometers). The shift is very large (more than 1 kHz) in contrast to the 10-50 Hz shift typically obtained in the regime of van der Waals forces.

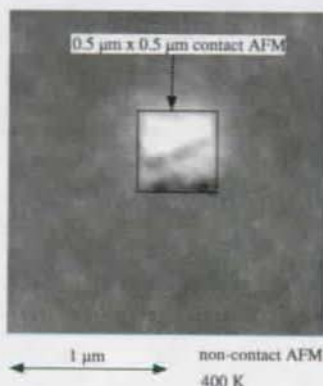


Figure 5.4: A MgO(100) surface with a charge pattern in the center.

vacancies and the emerging points of dislocations transport charges to the surface of ionic crystals. As AFM is sensitive down to single charge carriers, only a few of these defects are sufficient to make topographic imaging impossible. Due to the large bandgap of 7.8 eV of MgO decharging in ultrahigh vacuum is difficult to achieve and takes at least several hours. Under ambient conditions the water film, which is always present, accelerates the discharge as we have seen in the case of the KBr(100)-surface, where similar charging effects disappear on a timescale of minutes. A similar behavior has been observed on a ultrahigh vacuum cleaved  $\text{CaF}_2$  surface, where decay times of electrostatic charges up to 24 h were found [66]. Another way to create charges at a surface is contact electrification. This process has been described extensively by Lowell *et al.* [91]. In the case of an AFM measurement, charges are transferred from the tip to the sample simply by the contact. The capability of charging and imaging the charges by AFM has been first demonstrated by Terris *et al.* [25] on a  $\text{Si}_3\text{N}_4$  substrate. In our measurements of the clean MgO-surface, this phenomenon seems to be responsible for the following observation: After an accidental contact of the tip with the sample, the oscillation recovers quite easily, but with completely changed topography. The sample then reveals a round shaped rise which begins at the scan line of the contact. It is straightforward to interpret this rise as charges, which interact with the tip and not, e.g., deposited material, because of their shape and the fact that this phenomenon was never observed on a metal film, which provides immediate decharging of the surface. The

effect of contact electrification can be explored in a more controlled manner by scanning a certain area in the contact mode and subsequently at a larger scale in the non-contact mode. If adsorbates at the surface would play a role, creation of a depression is expected (as seen, e.g., in Fig. 3.14), but a bump is observed instead (see Fig. 5.4). In this example, in the center a  $0.5 \times 0.5 \mu\text{m}$  area was scanned in the contact mode and subsequently the whole frame image in non-contact mode AFM. Although it is plausible that, in fact, a charge effect causes this bump, the only definite proof would be to separate charge and topographical signal as described in Chap. 2.1.3. This offers the possibility of storing information e.g. via locally charging an insulating substrate like silicon oxide. On the other hand, local dielectric properties of the sample and local variations of the work functions can be measured with high lateral resolution (kelvin probe microscopy).

For the piezolever detection scheme, the most simple approach would be to oscillate the bias of the wheatstone bridge, which has not been done yet. Nevertheless, charging was not successful in every experiment and details of the responsible mechanism remain unclear.

Another way of depositing charges on MgO occurred upon evaporation of palladium. Palladium is evaporated from an  $e^-$ -beam heated rod. For this purpose, the electrons are accelerated from a filament to the rod which is biased to 1000 V. This yields about 10-20 % ions in the flux of palladium atoms, which are effectively accelerated by the electric field. In the submonolayer range, AFM non-contact measurements were thus impossible during several hours after deposition. In the multilayer range, where a continuous grounded film is deposited and upon silver deposition from a Knudsen cell, this observation was not made. This indicates that in fact the emitted ions are responsible for this phenomenon. Furthermore, by applying a positive voltage of 1250 V to an electrode at the exit tube of the evaporation source, this effect disappeared. The field effectively blocks the positively charged ions and prevents the charging of the surface.



.

## Chapter 6

# Metal nucleation and growth on MgO(100)

This chapter deals with the metal deposition in the sub-monolayer range on the MgO(100) surface, with the objective to create model systems for catalysis. Experiments realized on comparable systems to date are reviewed and the relevant basic physical processes are discussed. The comparison between palladium and silver deposition reveals a very different behavior of these metals with respect to defect nucleation due to a different interaction with the MgO substrate. This behavior offers the possibility to control the growth of metals on the nanometer scale and to create specific nanostructures.

### 6.1 Metal growth on metaloxides

An important reason for choosing the system of palladium on magnesium oxide as a model system was the quite extensive work already published for this system. From the group of C.R. Henry studies employing Helium scattering, Auger electron spectroscopy, fourier transform infrared spectroscopy, to real space examinations by transmission electron microscopy of palladium growth on bulk MgO-surfaces have been reported [92-99]. An early study of the growth of palladium on a thin film of magnesium oxide is reported as well. In this study, MgO(100) films were grown epitaxially on a cleavage face of NaCl, which was covered by LiF. They observed the size of palladium particles obtained at a certain exposure time and at different substrate temperatures. For this behalf, the sample was covered by carbon, dissolved from the substrate and subsequently analyzed in transmission electron microscopy. From the variation of the nucleation density as a function of the substrate temperature, a diffusion energy of 0.24 eV was deduced [99]. Nevertheless,

due to the MgO preparation the saturation nucleation density is comparably high, so that defect nucleation was observed in this case rather than the nucleation on a defect-free terrace.

This drawback has been circumvented by the preparation of better suited UHV-cleaved MgO surfaces and the thus obtained nucleation properties are compared to those obtained on defect-rich, air-cleaved (and UHV annealed) crystals [92]. This offers the possibility to study particle sizes from 1.6 nm to 12 nm under the different evaporation conditions, the smallest of which were grown on the air-cleaved crystals. The particle diameter distribution is comparatively sharp, varying between 0.4 nm and 2.4 nm, with the exception of low-temperature deposits on air-cleaved crystals. In this case the size distribution is quite wide due to defect nucleation. Micro-cleavages which allow the observation of the substrate and the deposit at the same time let the authors conclude that Pd grows epitaxially on MgO with parallel (100) directions. The transmission electron micrographs reveal furthermore the orientation of the particles, which exhibit a (100) surface on the top. The lateral faces show (110) and (111) faces with about 70% of the total surface of the clusters being (100)-type.

As TEM experiments always suffer from the quite complicated preparation scheme including contact with ambient conditions, the same group compares the results with helium diffraction experiments. This technique is additionally sensitive to the very first stages of nucleation and offers thus an insight to the transition from nucleation and growth to pure growth of the palladium clusters. They examined the nucleation and growth on UHV cleaved crystals and deduced a nucleation rate of  $7.6 \times 10^9 \text{ cm}^{-2} \text{ s}^{-1}$  at  $250^\circ$  and of  $4.1 \times 10^9 \text{ cm}^{-2} \text{ s}^{-1}$  at  $330^\circ \text{C}$  [100]. The island number density was measured *in-situ* by this method and a saturation density of about  $6 \times 10^{11} \text{ cm}^{-2}$  was obtained at  $160^\circ \text{C}$ ,  $2.5 \times 10^{11} \text{ cm}^{-2}$  at  $290^\circ \text{C}$ , and  $1.8 \times 10^{11} \text{ cm}^{-2}$  at  $370^\circ \text{C}$ . The results indicate nucleation at point defects, although UHV-cleaved crystals were used as substrates and the number density of clusters varies in the examined temperature range [93, 98].

Finally, fourier transform infrared spectroscopy experiments of CO adsorption on Pd clusters on MgO(100) have been reported. A saturation coverage of CO is dosed to the surface at 310 K and two absorption bands are observed, one of which represents reversely adsorbed CO, the other irreversibly adsorbed CO. In a very qualitative manner the intense band at  $1957 \text{ cm}^{-1}$  is assigned to the facets of the Pd particles and the weak band at  $2058 \text{ cm}^{-1}$  to their edges [95].

This knowledge about nucleation and growth was used to unveil the ques-

tion if cluster size effects play a role in heterogeneous catalysis [101]. Three different cluster sizes were prepared with an average diameter of 13 nm, 6.8 nm, and 2.8 nm. The reaction of CO and O<sub>2</sub> was measured in a temperature range from 400 K - 600 K by dosing CO to the sample with a molecular beam source while maintaining a background pressure of  $1.3 \times 10^{-7}$  mbar O<sub>2</sub>. The CO and CO<sub>2</sub> desorption rates were measured by a differentially pumped mass spectrometer. In the plot of the turnover number versus temperature a drastic size effect occurs between the 13 nm and the 6.8 nm sized particles, which increases the turnover number. For the 2.8 nm particles in comparison to the 6.8 nm particles the effect is less pronounced. In earlier publications, such observations have been explained by a spillover from the support to the clusters. For the data presented in this experiment, however, this explanation does not fit the experimental results satisfactorily, thus the authors concluded a real size effect occurring for the small particles.

Beneath early decoration experiments [63], which aimed at primarily the examination of the MgO surface itself, the epitaxy of gold and silver has been examined by Palmberg *et al.* [69]. The authors observed an excellent epitaxy over a wide temperature range (-195°C to 200°C) by LEED, but did not have a detailed access to nucleation and growth. However, the film became electrically continuous at an average coverage of 3 - 5 ML indicating initial 3d growth of these metals.

More recently, the growth of Ag on MgO(100) has been examined by EXAFS and XPS [81, 102]. These authors find a layer-by-layer growth mode of silver on MgO at room temperature by comparing Ag and Mg peaks in XPS. They suggest that the very clean and defect-free surface enables this layer-by-layer growth, because the presence of a few percent of a monolayer of carbon or defect features in the bandgap of the crystal drastically change the growth mode. This growth mode is metastable, because film roughening was observed upon annealing for 2 min at 500 K. This growth mode was also confirmed in the EXAFS experiment. The silver overlayer adopts the lattice constant of MgO with the silver atoms sitting atop the oxygen atoms at a distance of 2.53 Å.

A grazing incidence X-ray diffraction study of room temperature deposition confirms the registry of Ag atoms on top of the oxygen atoms, but with the smaller distance of 2.43 Å [103]. The growth mode, however, is different in this experiment. After the formation of 2d islands, 3d growth is observed (i.e. Volmer-Weber growth mode), which is explained by the higher adhesion energy of silver to silver than to magnesium oxide<sup>1</sup>. As the surface

---

<sup>1</sup>This is a thermodynamic argument which does not necessarily contradict the obser-

preparation is a crucial parameter for the growth mode, different preparation techniques may account for this observation.

A considerably different approach to metal growth on metaloxides is the preparation of thin films of these substrates. It has been demonstrated for MgO and TiO<sub>2</sub> [104, 105] on Mo(001) and for Al<sub>2</sub>O<sub>3</sub> on NiAl(110) [106, 107]. These layers, which are one to several ten monolayers thick, offer the advantage of facilitating the employment of electronic techniques including scanning tunneling microscopy and standard surface preparation techniques, because the film discharges via the underlying metal substrate. However, this is an important disadvantage, as interactions between the substrate and the thin film may interfere. Furthermore, these films exhibit usually a high number of defects.

Xu *et al.* [105] report on growth of palladium on an 8 ML MgO film investigated by STM. 1.2 ML Pd were deposited at room temperature leading to the formation of clusters with an average size of 32 Å. The width of the size distribution is about 10 Å. This value is slightly higher than that obtained in the TEM experiments on air cleaved crystals cited above, but island enlargement due to tip effects may occur. For the present system they are expected to be more pronounced, because the tunneling conditions (about 4 V tunneling bias due to the 7.8 eV bandgap of MgO) result in a large tip-sample distance compared to measurements on metal systems and the resolution is reduced. The island density is not given in this experiment and can only be estimated from the coverage and the island size. The adhesion energy is not measured, too, but tip-assisted drag of complete clusters is demonstrated, which suggests weak adhesion.

The comparable system of palladium deposited on a thin alumina film has been studied as well [108]. Apart from domain boundaries and steps, these films should be defect-free. At 300 K, 3-dimensional growth is observed after homogeneous nucleation. Typical island sizes are about 60 Å depending on the nominal film thickness and the maximum island density before coalescence sets in is  $1.25 \times 10^{12} \text{ cm}^{-2}$ . In contrast, at 90 K the island density is much higher due to defect nucleation at the domain boundaries and steps. No adhesion energy has been measured but the 3d growth mode confirms the weak interaction between Pd and alumina.

Palladium and silver interaction with MgO was also subject of theoretical studies, with the aim to determine the preferential adsorption site and the corresponding adsorption energy. This task is more complex for palladium than silver, because an interplay between the ground state and the first

---

vation of layer-by-layer growth in a kinetic growth regime.

excited state has to be accounted for and relativistic effects become more pronounced. Yudanov *et al.* [109] found an adsorption energy of 0.95 eV at the oxygen site with a bond length of 2.15 Å. The bond character is described as a hybridization between the Pd 4d and the O 2p orbitals. Stirling *et al.* [110] found an adsorption energy of 0.82 eV for Pd on top of the oxygen, whereas Ferrari and Pacchioni [111] found a substantially lower energy of only 0.11 eV for Pd on oxygen. These authors examine the role of defects as preferential nucleation sites for the growth of metals on MgO. In fact, examination of different types of defects (Mg or O vacancy) reveal the binding energy of 9.92 eV for palladium at a Mg vacancy and 1.55 eV at an oxygen vacancy. Thus both types of defects should act as very effective traps for palladium.

Silver adsorption is characterized by its low adsorption energy compared to palladium, which has been calculated to be 0.3 eV [112], 0.33 eV [109] or 0.2 eV [113, 114], with the preferred sites on top of the oxygen atom as well. The adsorption energy on defect sites has also been calculated for silver [111]. It is the Mg vacancy which causes the highest adsorption energy of 11.97 eV; on oxygen vacancies this energy is reduced to 0.99 eV<sup>2</sup>.

Thus, adsorption behavior of silver and palladium is expected to differ substantially, for nucleation on defect-free terraces as well as for defect nucleation.

## 6.2 Nucleation theory

In a molecular beam epitaxy (MBE) experiment nucleation and growth in general takes place far away from equilibrium conditions. At high temperatures, where at least conditions close to equilibrium are fulfilled, thermodynamic arguments can, however, be useful for the prediction or description of the growth mode. E. Bauer [115] defined these criteria by the interface and surface free energies. If

$$\gamma_f + \gamma_i \leq \gamma_s \quad (6.1)$$

is fulfilled for every layer ( $\gamma_f$ : surface energy of the film;  $\gamma_i$ : interface free energy;  $\gamma_s$ : substrate free energy) a two-dimensional growth mode (Frank-van der Merwe growth mode) is expected. If this condition is not fulfilled after a certain number of layers a layer plus island growth mode (Stranski-Krastanov growth mode) results. Strain energy accumulated due to lattice misfits, which

---

<sup>2</sup>In this study, silver does not bind on the defect-free MgO.

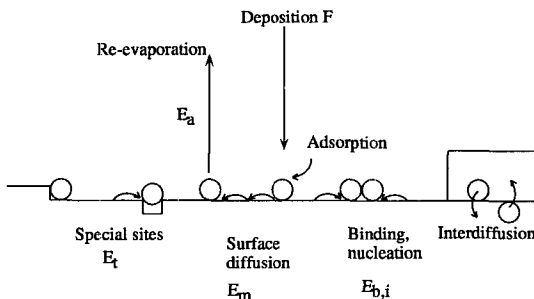


Figure 6.1: Processes involved in nucleation and growth.

is contained in  $\gamma_i$ , may be responsible for the onset of island growth<sup>3</sup>. Finally, if equation (6.1) is never fulfilled, a three-dimensional growth mode (Volmer-Weber growth mode) is obtained.

At low temperatures, however, these assumptions do not hold anymore as kinetic effects start to govern island and thin film growth with a large variety of unawaited effects [116]. In the kinetic approach of nucleation theory, diffusion of adatoms impinging onto the surface is the elementary process. They may be re-evaporated, integrated into the surface or trapped at steps or defects (See Fig. 6.1), or finally, the diffusing adatoms may encounter each other and nucleate. These nuclei then may either decay or grow further until they reach a certain size  $i$ , the critical cluster size. Upon integration of an additional atom, these clusters become stable and desorption of an atom from these stable clusters is considered to be very low on the timescale of deposition. These processes are shown in Fig. 6.2. At a certain time, the capture of single adatoms by stable clusters overcomes the nucleation of new ones, the saturation island density is obtained and the growth regime begins. The different processes are determined by energy barriers: The adsorption energy  $E_a$  determines the re-evaporation rate; the migration energy  $E_m$  determines the surface diffusion via the dependence of the diffusion constant on  $E_m$ :  $D = D_0 \exp(-E_m/kT)$ . Binding and nucleation of adatoms depends on the binding energy  $E_i$  of the cluster of size  $i$ . Enhanced nucleation may be found due to the fact that special sites like point defects and steps exhibit a higher adsorption energy than the defect-free surface ( $E_i$ : “trapping” the

<sup>3</sup>After the completion of a perfect layer in a heteroepitaxial experiment, further growth is principally homoepitaxial, thus the free energy of the film and the substrate are identical. Thus  $\gamma_i$  is crucial for the growth mode.

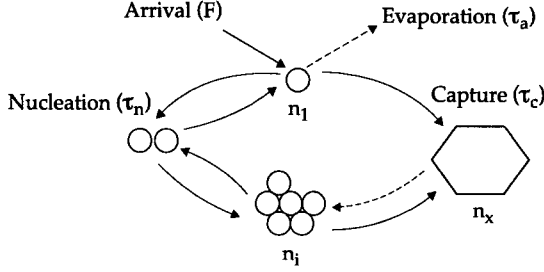


Figure 6.2: Detailed view of the interplay of atomic processes involved in nucleation and growth of clusters. The different time constants ( $\tau_n$ ,  $\tau_a$ ,  $\tau_c$ ) describe the variation of the adatom concentration  $n_1$  due to nucleation, evaporation, and capture by stable clusters. From [117].

atoms). The variation of the number of adatoms, subcritical and stable clusters can be calculated by rate equations, in a first approach excluding special sites as nucleation centers [118]:

$$\frac{dn_1}{dt} = F - \frac{n_1}{\tau_a} - \frac{dn_x w_x}{dt}, \quad (6.2)$$

$$\frac{dn_j}{dt} = 0 \quad (2 \leq j \leq i), \quad (6.3)$$

$$\frac{dn_x}{dt} = \sigma_i D n_1 n_i. \quad (6.4)$$

A decay of stable clusters ( $n_x$ ) due to coalescence and cluster diffusion (only single atoms are mobile on the surface) has been excluded. In the first equation, the number of adatoms ( $n_1$ ) increases by the flux of impinging atoms  $F$ . The time constant  $\tau_a$  describes the time an adatom stays at the surface before re-evaporation, consequently  $\frac{n_1}{\tau_a}$  is the loss of adatoms due to this process. The last term represents the loss of single atoms due to encounters with  $n_x$  stable clusters of the size  $w_x$  (average number of atoms per cluster).

The second equation is the consequence of the detailed balance argument, when a local thermodynamical equilibrium is obtained for clusters of subcritical size. In this case adsorption and desorption from a subcritical cluster



occur at equal rates and their number remains unchanged.

In the third equation the increase of stable clusters is given by integrating an adatom to a critical cluster.  $\sigma_i$  is the capture number of a cluster for single adatoms, which includes the exact distribution of adatoms on the surface. A model to treat these numbers has been proposed e.g. by Bales and Chrzan [119].

The loss of adatoms due to integration into stable clusters (Eq. (6.2)) can be expressed as follows:

$$\frac{dn_x w_x}{dt} = (i+1)\sigma_i D n_1 n_i + \sigma_x D n_1 n_x + FZ \quad (6.5)$$

$\sigma_i D n_1 n_i$  is the loss of single adatoms due to nucleation and hence the same term as in Eq. (6.4).  $\sigma_x D n_1 n_x$  is the loss due to capture by a stable cluster and  $FZ$  results from direct impingement of an incoming atom onto a stable cluster. This is the contribution that gives the dependence on growth mode either 2d-growth or 3d-growth. We will see that both palladium and silver grow in a 3-d fashion and so we restrict the following discussion to this case.

The actual number of clusters  $n_x$  as a function of the deposition time and coverage has to be calculated by computing the rate equations (6.2), (6.3) and (6.4). For the saturation density, however, which represents the maximum island density during deposition, a general equation has been obtained [120]. This equation is for 3-d islands:

$$n_x^{3/2} (1 + \sigma_x D \tau_a n_x)^i (Z_0 + \sigma_x D \tau_a n_x) \propto \left(\frac{F}{D}\right)^i \exp\left(\frac{E_i}{kT}\right) (\sigma_x D \tau_a)^{i+1}. \quad (6.6)$$

In the complete condensation regime ( $Z_0 \ll 1 \ll \sigma_x D \tau_a n_x$ ) the saturation island density can be written as:

$$n_x \propto \left(\frac{F}{D}\right)^{\frac{i}{i+2.5}} \exp\left(\frac{E_i}{kT}\right). \quad (6.7)$$

This expression can be simplified further if the critical cluster size is  $i = 1$ . Then the binding energy  $E_i$  of the cluster is eliminated from the equation and the migration barrier can be calculated from an Arrhenius plot of  $\ln n_x$  in function of  $1/T$ .

$$n_x \propto \left(\frac{F}{D_0}\right)^{2/7} \exp\left(\frac{2E_m}{7kT}\right). \quad (6.8)$$

From equation (6.7), the size of the critical cluster can be deduced as the slope of the plot  $\ln n_x$  versus  $\ln F$  in a rate dependent experiment at constant temperature.

For sufficiently low temperatures, a critical cluster  $i = 1$  is almost always obtained and equation (6.8) is applicable, then  $E_m$  is directly accessible from the slope of a plot of  $\ln n_x$  versus  $1/T$ .

## Nucleation in the presence of defects

Strong deviations from the Arrhenius type temperature dependence of  $n_x$  have been found for metal deposition on insulating surfaces [99, 121]. Typically a constant island density over a wide temperature range was observed, which cannot be reproduced by Eq. (6.7). This initiated the introduction of defects (vacancies, steps, emerging dislocations...) as additional nucleation centers [121, 122]. Hence, another term for the creation of clusters has to be introduced and modifies equation (6.4) by:

$$\frac{dn_x}{dt} = \sigma_1 D n_1 n_1 + \sigma_{1t} D n_1 n_{1t} + F n_1; \quad (6.9)$$

$n_{1t}$  is the number of adatoms located at defect sites and  $\sigma_{1t}$  is the capture number of the defect. As the defects are saturable, this number follows a Langmuir adsorption isotherm:

$$\frac{n_{1t}}{n_t - n_{xt}} = \frac{A_t}{1 + A_t}; \quad (6.10)$$

with  $A_t = n_1 \exp(E_t/kT)$  describing the activation of the traps with an energy of  $E_t$ .  $n_t$  is the total density of defects and  $n_{xt}$  the number of already occupied defects and accounts for the decrease of active defects. By these considerations, the right hand side of equation (6.6) is enhanced due to the nucleation at defects by a factor of  $(1 + A_t)$ :

$$n_x^{3/2} (1 + \sigma_x D \tau_a n_x)^i (Z_0 + \sigma_x D \tau_a n_x) \propto \left(\frac{F}{D}\right)^i \exp\left(\frac{E_i}{kT}\right) (\sigma_x D \tau_a)^{i+1} \left(1 + \frac{n_x - n_{xt}}{n_{1t}}\right) n_1 \exp\left(\frac{E_t}{kT}\right). \quad (6.11)$$

In contrast to Eq. (6.6), Eq. (6.11) cannot be simplified to yield an analytical expression of the island density  $n_x$ . In addition, the right hand side contains the time dependent functions  $n_{xt}$ ,  $n_{1t}$  and  $n_1$ . Therefore, the number density has to be deduced from a numerical integration of the rate equation and straightforward analysis of experimental data in terms of critical cluster size and migration barrier is not possible. In the presence of defects, there are additional parameters ( $E_t$ ,  $E_b$  and  $E_a$ ) that have to be adjusted in a full iterative calculation.

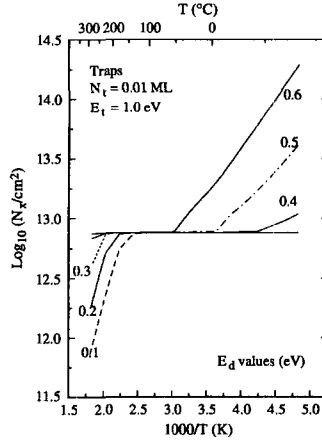


Figure 6.3: Number density of islands in the presence of point defects. Defects trap atoms with an energy of 1.0 eV and cover 0.01 ML of the substrate. Taken from [121].

Corresponding plots for the number density of islands and different parameters are given in Fig. 6.3. Depending on the different values of the diffusion barrier a pronounced plateau where the number density is constant is observed. A plateau in the Arrhenius plot hence indicates the presence of strong trapping point defects.

### 6.3 Palladium nucleation and growth

Palladium was evaporated on a MgO substrate (prepared as described in chap. 5.2) from an  $e^-$ -beam heated rod (99.99 % purity, Advent Materials, UK) by a commercial evaporator (Omicron Instruments, Germany). The flux has been calibrated in previous STM experiments of Pd growth on Pd(110) [123] and was monitored by Auger electron spectroscopy. Ions were retracted by a blocking potential to avoid charging of the surface. In the temperature dependent measurements, a substrate temperature range from 350 K to 800 K with a coverage of  $\approx 0.1$  ML evaporated at a rate of  $2.7 \times 10^{-4}$  ML/s was examined.

In the flux dependent measurement, 0.1 ML was evaporated at 475 K and 745 K at flux values between  $2.7 \times 10^{-5}$  ML/s and  $2.7 \times 10^{-3}$  ML/s. It can be

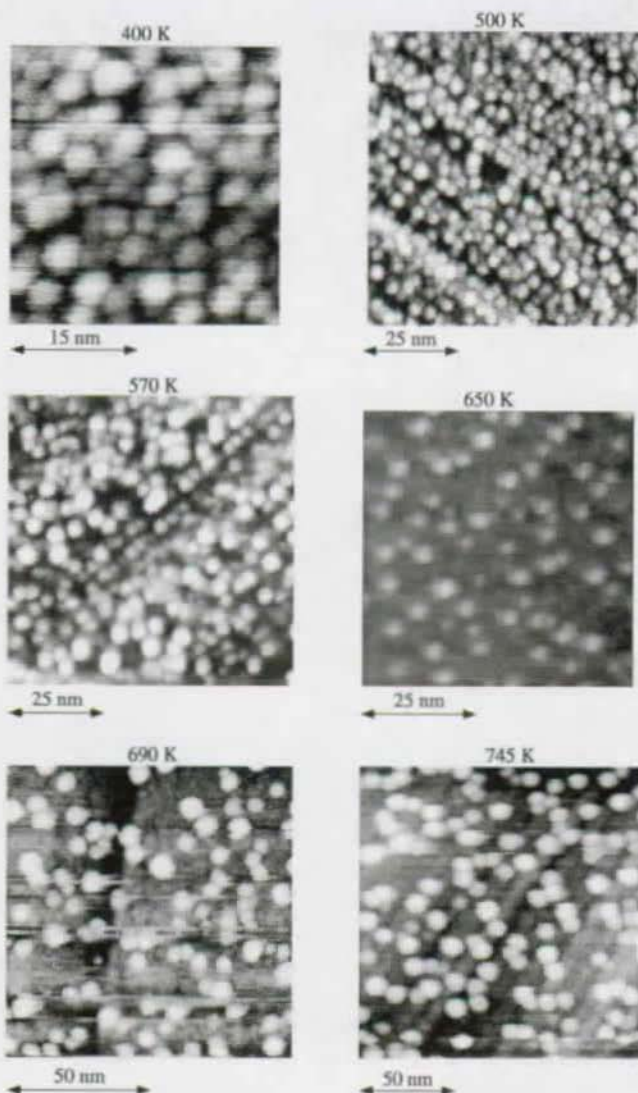


Figure 6.4: Non-contact AFM micrographs of palladium deposition (coverage 0.1 ML) on MgO(100) at the indicated substrate temperature. Images taken at room temperature.

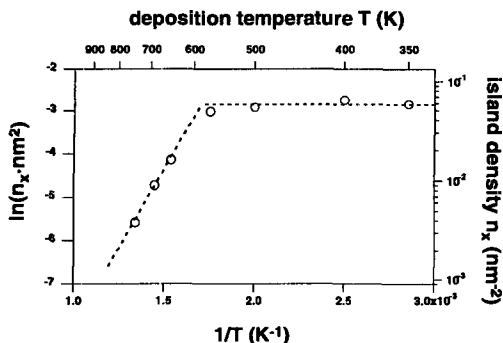


Figure 6.5: Arrhenius plot of the palladium island density versus substrate temperature (flux:  $2.7 \times 10^{-4}$  ML/s; coverage: 0.1 ML).

assumed that the saturation density is obtained under these conditions [98, 99].

A series of AFM micrographs obtained in the non-contact mode is shown in Fig. 6.4. In the complete temperature range growth of round shaped islands is observed. This shape, however, cannot merely be assigned to the actual shape of the islands, because the influence of the tip is very important for small structures. At 400 K the clusters are barely resolved and, whereas the size does not change drastically at 500 K and 570 K, they are more distinct. At these temperatures, step decoration prevails. At even higher temperatures, the island density decreases strongly and step decoration is no longer observed.

The logarithm of the island density  $\ln n_x$  versus the inverse temperature  $1/T$  is plotted in Fig. 6.5. This Arrhenius graph shows the plateau indicating the presence of defect sites in the nucleation process. If the defect nucleation is complete and no cluster mobility exists, the thus obtained island density corresponds to the defect density on the substrate. This was used e.g. in early decoration experiments of alkali halides [63]. In our experiment, the defect density can be estimated from the plateau to  $6 \times 10^{12}$  defects/cm<sup>2</sup> which corresponds to  $2.3 \times 10^{-3}$  ML (a monolayer corresponds to  $2.2 \times 10^{15}$  atoms/cm<sup>2</sup>).

In the linear regime at higher temperature the thermal energy of the impinging atoms is high enough to escape from the defects but their movement will be hindered as they rest for a longer time at the defect sites. The

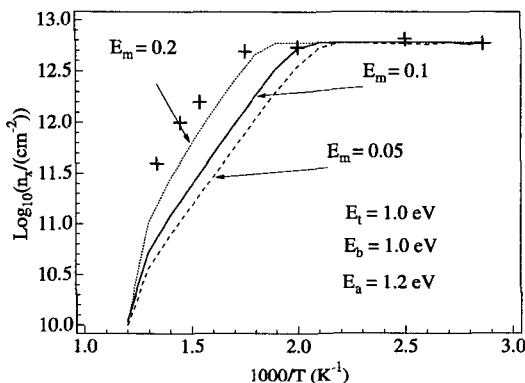


Figure 6.6: Calculation of the number density of islands in the presence of defects for the Pd/MgO(100) system with diffusion energies of 0.2 eV, 0.1 eV, and 0.05 eV respectively [124]. The crosses indicate the measured values.

slope value expressed as an energy from the linear fit is  $(0.63 \pm 0.05)$  eV. This value, however, should not directly be associated with  $E_m$ , which has been measured to 0.24 eV by TEM observation of Pd islands on MgO(100) [99]. In this experiment, no plateau was observed, because the temperature range was well above its occurrence. Nevertheless, it is more probable, that defects played a role in this experiment, too. Other metal/ionic crystal systems reveal typically diffusion energies between 0.2 and 0.4 eV [118]. The theoretical values of the adsorption energy of 0.95 eV [109] and 0.85 eV [110] are of the same order of magnitude if the diffusion energy is roughly considered to be a third of the adsorption energy.

The actual value of the migration barrier  $E_m$  has to be obtained by solving the rate equations (6.2), (6.3) and (6.4) with reasonable values of  $E_t$ ,  $E_a$  and  $E_i$ . This has been done in Fig. 6.6 [124]. The calculated plots for different migration barriers of 0.05 eV, 0.1 eV, 0.2 eV reproduce well the experimental values. By a further adjustment of the free parameters, an even better agreement of theory and experiment can be achieved. The onset temperature of the Arrhenius behavior of  $n_x$  in the experiment is e.g. basically defining the trap energy, because atoms are able to overcome the barrier of these traps. Future experiments at low temperatures, where diffusion is slow, so that atoms nucleate before they can be trapped by a defect will better define the migration barrier. This will lead, however, to an island density higher than that observed in Fig. 6.4 a) which is already close to the resolution limit

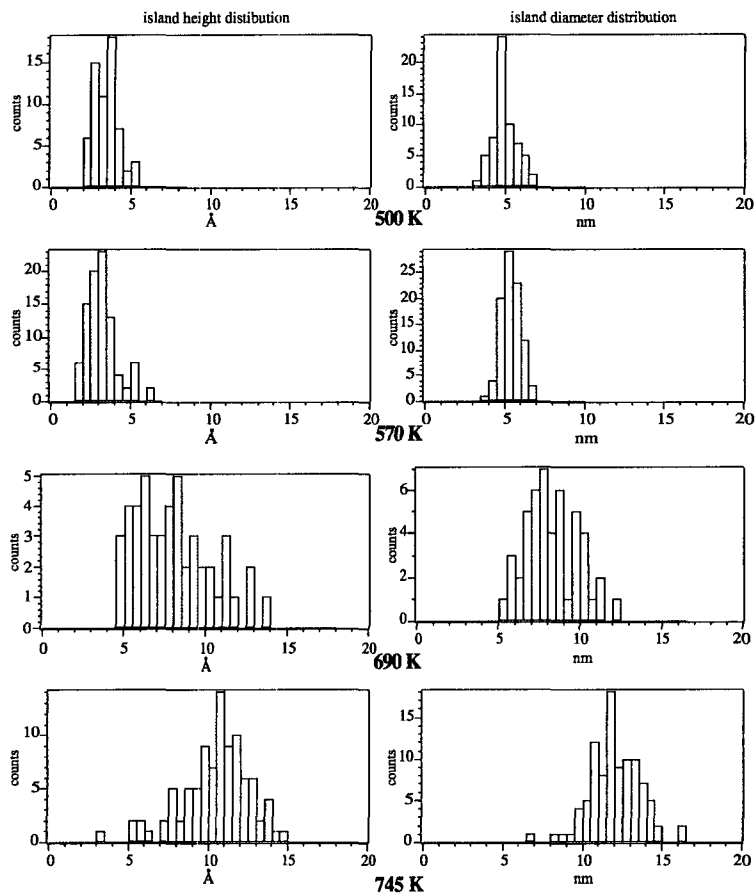


Figure 6.7: a) Island height distribution and b) island diameter distribution for Pd clusters grown at different temperatures.

in an AFM experiment.

The limited resolution is obvious in Fig. 6.4. Even if the clusters are still distinguishable at a distance of about 3-4 nm (which we will hence call the lateral resolution limit of the AFM) their size is by far overestimated. At 400 K the clusters appear to cover the entire surface; an effect which is reduced in the case of the 745 K substrate temperature to about 50%. Responsible is the finite radius of the tip as illustrated in Chap. 3. Thus, when discussing the cluster sizes in these non-contact AFM experiments, enlargement due to tip convolution has to be taken into account. Unfortunately, this artifact depends furthermore on the height of the imaged feature.

Keeping in mind these restrictions, Fig. 6.7, however, enables us to deduce some qualitative information from the cluster height<sup>4</sup> and size distribution. In these histograms, the measured heights and widths of the clusters were determined in steps of 0.5 Å or 0.5 nm respectively. The width was estimated at the base of the hemispherical clusters, and thus represents an upper limit of their actual size.

The influence of the substrate temperature is especially pronounced if we compare the temperatures in the plateau (500 K and 570 K) with those above (690 K and 745 K). At the lower temperatures, the island height histogram is centered around 3 - 4 Å with a width of about 1.5 Å. Since the single layer height of Pd is about 2.5 Å this height corresponds presumably to a palladium bilayer. At the higher temperatures, the height increases drastically, a Volmer-Weber growth mode is obtained. At 690 K the distribution becomes very broad and no clear center is visible. Height levels distanced by 2 - 3 Å are observed which presumably marks the onset of further three-dimensional growth. At 745 K the distribution is centered at about 10 - 11 Å with a width of 4 Å. The relative width is hence comparable to that obtained at lower temperatures, but the palladium islands now are four layers thick. This clearly shows that the three-dimensional growth mode is preferred for palladium growth on MgO. This agrees with the criterion defined at the beginning (Eq. (6.1)). The surface energy of MgO is lower than that of palladium, hence, regardless of the unknown interfacial energy, a three-dimensional growth mode is expected. The question if this growth is realized in an epitaxial way cannot be judged from this height information. The widths are too large to clearly resolve distinct epitaxial layers. Comparison with literature results show that epitaxy is obtained for palladium on MgO

---

<sup>4</sup>The height of the cluster should be measured correctly. If the clusters are very high and close together, however, the tip might not penetrate between them to the substrate and hence the height will be underestimated.



and the adoption of the palladium lattice to the very different MgO lattice was examined by electron microscopy [92, 125].

The island diameter distribution is marked by a clear shift in island sizes at the onset of free diffusion on the terrace. Before, the apparent island size is 4-5 nm at 500 K and only slightly larger at 570 K with a width of 1.5 nm. At 690 K the center of the distribution shifts to 8-9 nm with the width of 4 nm. At 745 K the islands are 11-12 nm in width and the distribution is sharp again ( $\approx 3$  nm). This observation compares well to those reported by Goyhenex *et al.* [97], where at low temperatures an average island size of 2 nm is observed with an increase to 7 nm at higher temperatures. For a coverage of 0.07 ML palladium a mean diameter of 6 nm with a distribution width of 4 nm was found at a temperature of 400° C comparing well to our observations [99]. Another paper, however, does not report a systematic dependence of the island size on the temperature, presumably due to the variation in total coverage imposed at the same time [125].

From these distributions it can be estimated to what extent the AFM tip overestimates the island size. In the low temperature deposit, the islands cover apparently nearly the entire substrate (c.f. Fig. 6.4). Weighting the total number of clusters with their mean size the coverage is  $\approx 0.9$  ML in the 500 K deposit. Assuming a bilayer growth the apparent coverage is 1.8 ML, thus a factor of 18 too high. For circular islands the diameter has consequently to be corrected by  $\sqrt{18} \approx 4.2$ . The real diameter of the island would then be slightly more than 1 nm. Another approach is the calculation what a tip radius of 10 nm would add to the edges of a cluster, which is 5 Å in height. This added distance  $d$  is given by

$$d = \sqrt{r^2 - (r - h)^2}$$

with  $h$  the height of the (vertical) edge and  $r$  the radius of curvature of the tip. For the given values  $d \approx 3$  nm. Thus a 1 nm bilayer island is imaged at least 7 nm in width. Taking into account the large error margins in this estimation, this compares well to the observed values.

The quantitative values concerning nucleation have to be read with care as we simplified the rate equations by several assumptions whose justification has still to be performed. The critical cluster size has to be determined in the flux dependent experiment, the dimensionality of the deposit is, however, more probably 3 than 2. Furthermore, the question of complete condensation occurs. It is reported that sticking of Pd on MgO(100) is incomplete over the entire temperature range from 160°C to 400°C [92]. As we do not have a possibility to compare the number of incoming atoms to those resting on the

surface it is difficult to prove whether complete condensation occurs or not. AES, however, proves that sticking, even if incomplete, does not decrease with increasing temperature in the range from 300 - 745 K.

From the deposition experiment at 800 K we know that reevaporation occurs at that temperature. Evaporation at the same flux yielded in a coverage reduced by a factor of  $\approx 10$  as monitored by AES. Longer deposition time at this temperature then enables the growth of a more twodimensional film as shown in 3.15.

A crucial parameter needed to interpret the slope of the graph 6.5 is the size of the critical cluster. This size can be deduced from a flux dependence measurement of the saturation island density. In the complete condensation regime, the exponent  $2/7$  in Eq. (6.8) in general is given by  $\chi = \frac{i}{i+2.5}$  with  $i+1$  the smallest stable cluster. Thus, from a double-logarithmic plot of the island density versus flux, this value can be obtained.

## Flux dependence

As we have seen above, Eq. (6.7) allows the measurement of the critical island size. At a constant temperature, the saturation density has to be measured as a function of the flux of incoming atoms. In the case of defect nucleation on MgO(100), the critical island size cannot be obtained straightforwardly, because there is no analytic equation describing the dependence of  $n_x$  on the flux. Nevertheless, the flux dependence measurement in the regime of defect decoration and in the Arrhenius part of the plot gives additional information on the system. In the plateau, where complete defect decoration is obtained, the flux dependence of  $n_x$  is by far weaker than its temperature dependence. Therefore at temperatures in the center of the plateau a variation of the flux should not affect the defect nucleation and hence yield a constant island density. At temperatures above the defect nucleation regime, the flux should influence the island density. It is expected, that all islands nucleate now at defects and the additional nucleation rate at these defects lowers the apparent adatom density compared to a defect-free surface. This results in an effective rate dependence in between a critical cluster size of  $i = 0$  (the single atom trapped in a defect represents a stable cluster of the size 1) and the actual critical cluster on a defect-free substrate. The obtained island density for the case of defect nucleation is shown in Fig. 6.8. The substrate temperature was maintained at 475 K during evaporation, while the flux was varied between  $2.7 \times 10^{-3}$  ML/s and  $2.7 \times 10^{-5}$  ML/s. The nucleation density is constant indeed, even for a variation of two orders of magnitude,

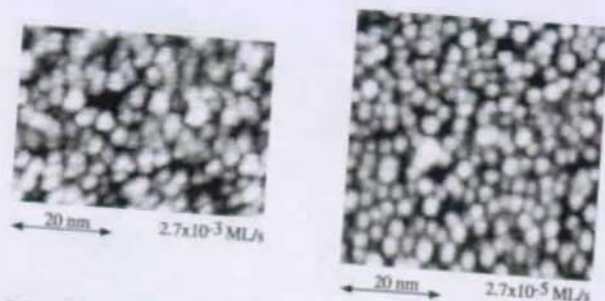


Figure 6.8: Non-contact AFM images of Pd deposition at the flux of  $2.7 \times 10^{-3}$  ML/s and  $2.7 \times 10^{-5}$  ML/s (substrate temperature 475 K; coverage 0.1 ML).

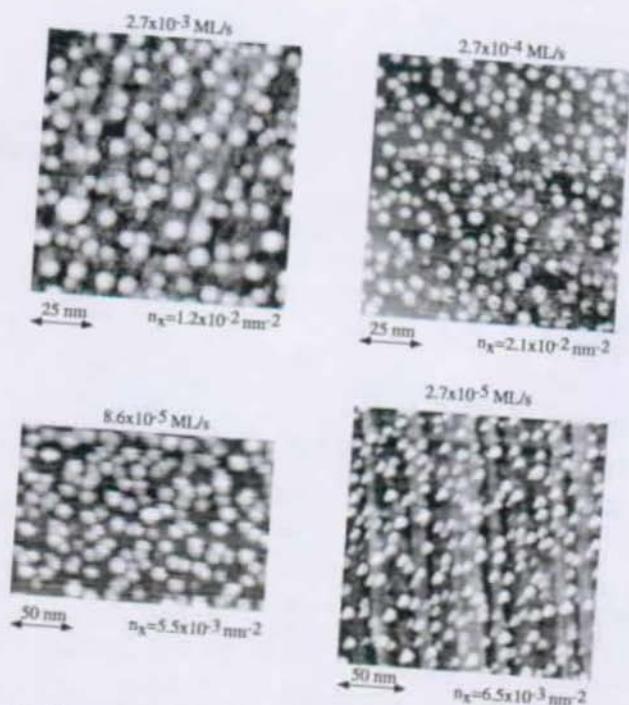


Figure 6.9: Non-contact AFM images of Pd deposition in the flux range between  $2.7 \times 10^{-3}$  ML/s and  $2.7 \times 10^{-5}$  ML/s (substrate temperature 745 K; coverage 0.1 ML).

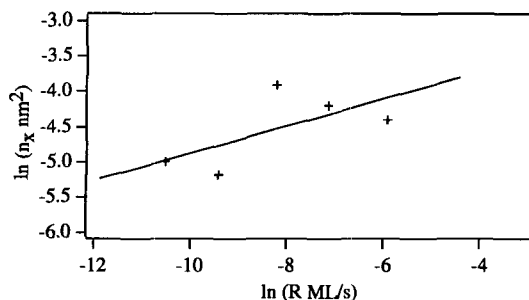


Figure 6.10: Double-logarithmic plot of the saturation island density versus deposition flux at 745 K and fixed coverage (0.1 ML)

0.08 islands/nm<sup>2</sup> ( $2.7 \times 10^{-3}$  ML/s) and 0.084 islands/nm<sup>2</sup> ( $2.7 \times 10^{-5}$  ML/s). This value, however, is slightly higher than the one observed in the plateau of the Arrhenius plot (0.06 islands/nm<sup>2</sup>) (Fig. 6.4). It is concluded that on this plateau the island density is governed by defect nucleation. While the surface preparation remained unchanged, a new crystal has been used for these experiment. Hence the increased island density can be understood as a result of the higher defect density of this crystal. If this is the case, however, the defect density is an intrinsic characteristic of the crystal and is less sensitive to the surface preparation technique.

Upon deposition at a higher temperature in the linear regime of Fig. 6.5, the influence of the evaporation flux becomes visible. In Fig. 6.9, the island density is varied over two orders of magnitude as well. The island density is given in the image. The value obtained from Fig. 6.4 again does not scale with these values, which indicates that the graph of Fig. 6.5 has to be shifted due to the higher defect density. From the double-logarithmic plot of the island density versus the deposition flux (Fig. 6.10) at constant temperature, the exponent in Eq. (6.8) can be deduced. In our case a value of  $0.2 \pm 0.13$  is obtained.

Equation (6.8) for the 3d-growth of clusters without defects on the surface and a critical cluster  $i = 1$  would result in an exponent of  $2/7$ . The critical cluster size  $i = 1$  seems to be reasonable due to the high bond energy of the free palladium dimer of 1.69 eV [126]. The value we obtained is actually slightly lower, which supports the interpretation of a mixed nucleation of critical cluster size  $i = 0$  at defects and  $i = 1$  without the presence of defects.

## 6.4 Silver nucleation and growth

As we have seen above in various theoretical and experimental studies, silver is expected to behave quite differently upon deposition on MgO(100) compared to palladium. The adsorption energy is by far lower, which facilitates the diffusion on the surface. We deposited silver on the MgO(100) surface from a Knudsen cell. The deposition flux was fixed by the cell temperature. At a temperature of 900°C the resulting flux was  $8.6 \times 10^{-4}$  ML/s, and the total coverage of 0.1 ML was deposited as verified by Auger electron spectroscopy. Substrate temperature during deposition was varied between 300 K and 550 K. Figure 6.11 shows the resulting silver deposit at three different temperatures. It is immediately obvious that the clusters formed by silver

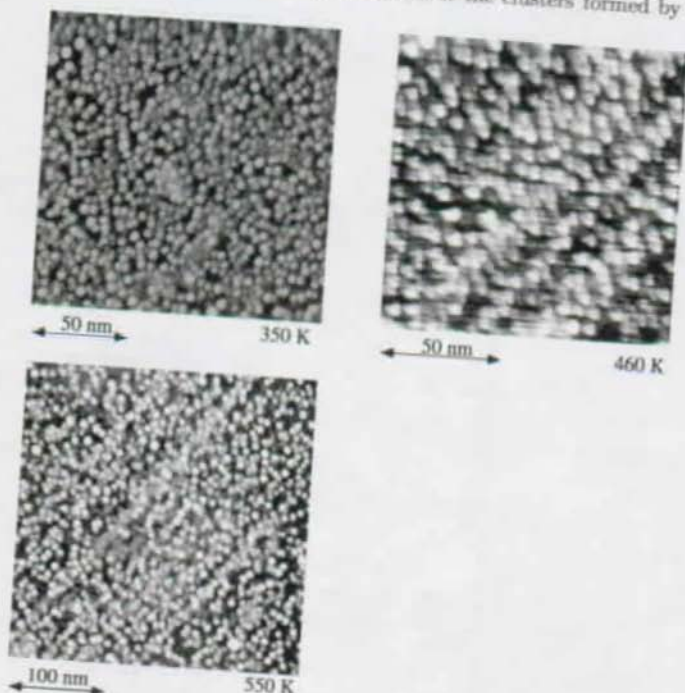


Figure 6.11: Non-contact AFM micrographs of silver deposition (coverage 0.1 ML) on MgO at the indicated substrate temperature. Images taken at room temperature.

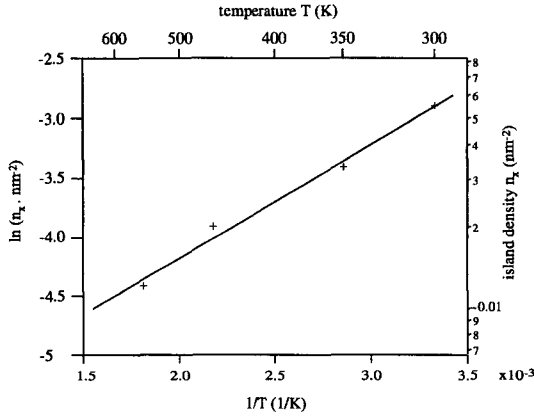


Figure 6.12: Arrhenius plot of the silver island density versus substrate temperature (flux:  $8.6 \times 10^{-4}$  ML/s; coverage: 0.1 ML)

on MgO(100) are larger than the Pd clusters, which enables better imaging conditions (for the 460 K deposit an asymmetric tip prevents better resolution). Nevertheless, the influence of the tip remains, because the surface coverage is overestimated as for palladium deposition.

From the images it is obvious, that in contrast to the palladium case, silver island density changes in this temperature range. This is shown in the logarithmic plot of the island density versus  $1/T$ . A straight line is now observed, thus an Arrhenius behavior is obtained. The slope of the graph expressed as an energy is  $(83 \pm 7)$  meV. The absence of a plateau may have two different reasons: Either the nucleation of Ag on MgO(100) is not influenced by the defects or we already observe the high temperature onset of nucleation.

If there is no influence, the diffusion energy can be calculated from the slope. As the dimer bond energy is high for the free silver dimer (1.65 eV [126]), the assumption of  $i = 1$  seems to be reasonable. Applying Eq. (6.8), a diffusion energy of  $(0.29 \pm 0.02)$  eV is obtained. This value has to be compared to the theoretical values for the adhesion energy of Ag on MgO(100), which is about 0.2 - 0.3 eV [109, 112–114]. In general, the diffusion energy is 1/5 of the adhesion energy or less, hence the value of 0.29 eV is by far too high (also compared to the palladium diffusion energy). Therefore it can be concluded that the defects also influence the mobility of silver even if there is no plateau in the Arrhenius plot. The reason is that island densities obtained in the silver deposition experiment are always lower than

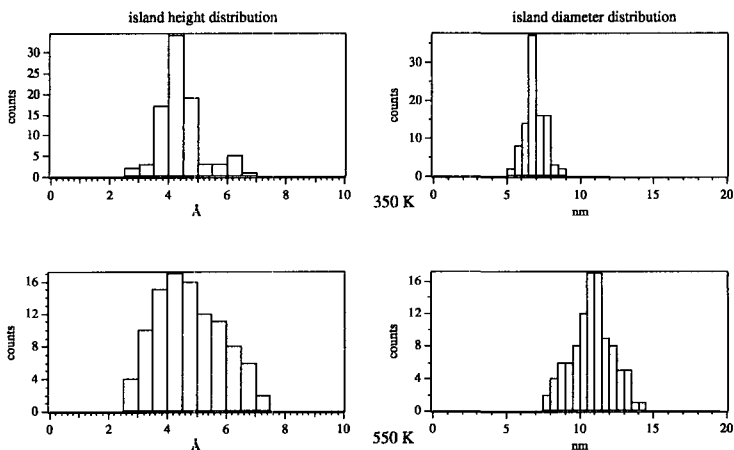


Figure 6.13: a) Island height distribution and b) island diameter distribution for Ag clusters grown at the indicated temperatures.

the defect density revealed in the palladium deposition experiment, therefore the plateau will appear at lower temperatures. The actual diffusion energy of silver on MgO then has to be calculated numerically from the rate equations (6.2), (6.3) and (6.4). As we have seen in Fig. 6.6, in the case of defect nucleation the actual diffusion energy is by far lower than the slope of the Arrhenius plot.

Histograms for the island height and size distributions have been established at 350 K and 550 K (Fig. 6.13). In the height distribution, the center is 4 - 4.5 Å in the case of 350 K and 550 K. But whereas the 350 K distribution reveals a quite sharp peak with a width of 1.5 Å, at 550 K the peak is by far broader. This might indicate that the clusters start to pile up further at that temperature. The change of the distribution is more pronounced in the island diameter distribution. The relative width is now comparable for both temperatures, but at 350 K about 6.5 nm wide clusters grow while at 550 K the average island size is about 11 nm. Thus the lower island density at higher temperatures leads directly to the growth of larger, but only partially higher, clusters.

These very different observations for the growth of silver on MgO compared to the growth of palladium may give insight in the nature of defects we deal with. Ferrari and Pacchioni calculated the adsorption energy on point defects, either missing O (F-centers) or missing Mg (V-centers) atoms [111].

They distinguished additionally the ionization state of these defects - either singly or doubly charged or uncharged. The adsorption energy at a magnesium defect site is very high (up to 12 eV) and even higher for silver than for palladium. It can be thus excluded from our results. The situation is different for the O vacancies. At the uncharged  $F_s$  center (which corresponds to a missing oxygen atom) the palladium is bound by 1.55 eV whereas silver atoms are virtually unbound. This agrees with our observation that palladium is more influenced by the defects than silver.





# Chapter 7

## Outlook

In this thesis, we have reported a nanometer-scale study of defect formation on the (100)-face of KBr and metal growth on MgO(100), which is also strongly influenced by the presence of defects. For the first experiment, an atomic force microscope of the beetle-type with the beam deflection detection technique was employed. For the latter experiment, which was performed in ultrahigh vacuum, an AFM using the piezolever detection scheme was designed allowing sample heating and cooling (variable temperature AFM, VT-AFM).

In the experimental setup combined with a fourier transform infrared spectrometer in the newly adapted transmission geometry. The next step in the future will be the correlation of nanometer-scale structural information with surface chemical analysis. From vibrational spectroscopy of adsorbed reactants, the catalytic activity of the metal/MgO model catalysts can be examined in detail. The correlation between particle size and reaction characteristics of the surface will be very interesting.

The nucleation and growth of palladium and silver on MgO examined by VT-AFM revealed a three-dimensional island growth of both metals in the examined temperature range. The temperature is, however, a crucial parameter for the actual size and density of these islands. Very high densities were found at room temperature in the case of silver or at a temperature range where defect nucleation takes place in the case of palladium (300 - 570 K). These clusters are very small; due to the limited resolution of the AFM their size can be determined to be less than 4 nm. These systems can provide good models for the small particles dispersed on the surface of a real catalyst. A better understanding of the palladium and silver growth mechanisms has been obtained and can be used now for controlled growth of metal/metaloxide nanosystems.

From the technical point of view, future work will focus on further improvement of the already good resolution of the instrument by a better control of the piezolever quality and tip properties. A promising approach is e.g. the growth of nanotubes, which provides very well defined and stable tips for atomic force microscopy enabling a better resolution of image sizes for very small clusters.

The installation of a UHV-cleavage facility would be a further refinement of the experiment, which may enable the preparation of samples with a lower defect density, offering presumably the control of defect densities via reactive attack similar to those occurring under ambient conditions.

Finally, the AFM/FTIR combination is particularly appropriate to work at elevated pressures. Ultimately, the surface can be visualized while reactions take place and it may be examined if reversible modifications of the morphology play a role in catalytic activity.

The growth of magnetic metals (Co, Fe, Ni) would be a very different possibility to benefit from the thus gained control of metal growth on insulators and the capability of the AFM to measure a great variety of forces. In contrast to integral techniques (e.g. surface magneto-optical Kerr effect (SMOKE)), the application of magnetic force microscopy (requiring only tips covered with a magnetic thin film) would allow to probe the magnetic properties of small clusters on a nanometer scale.

# References

- [1] M. Haruta, *Catalysis Today* **36**, 153 (1997).
- [2] S. Ogawa and S. Ichikawa, *Phys. Rev. B* **51**, 17231 (1995).
- [3] G. Somorjai, in *Introduction to Surface Chemistry and Catalysis* (Wiley, New York, 1994), Chap. 7.
- [4] F. Besenbacher and J. Nørskov, *Science* **279**, 1913 (1998).
- [5] E. Hahn, Ph.D. thesis, École polytechnique fédérale de Lausanne, 1994.
- [6] G. Binnig and C. F. Quate, *Phys. Rev. Lett.* **56**, 930 (1986).
- [7] S. Horch, P. Zeppenfeld, R. David, and G. Comsa, *Rev. Sci. Instrum.* **65**, 3204 (1994).
- [8] H. Brune, H. Röder, C. Romainczyk, C. Boragno, and K. Kern, *Appl. Phys. A* **60**, 167 (1995).
- [9] E. Meyer, *Prog. in Surf. Sci.* **41**, 3 (1992).
- [10] F. J. Giessibl, *Science* **267**, 68 (1995).
- [11] L. Howald, R. Lüthi, P. Güthner, and H.-J. Güntherodt, *Z. Phys. B* **93**, 267 (1994).
- [12] S. Ciraci, A. Baratoff, and I. P. Batra, *Phys. Rev. B* **42**, 7618 (1990).
- [13] F. London, *Z. Phys.* **63**, 245 (1930).
- [14] H. Casimier and D. Polder, *Phys. Rev.* **73**, 360 (1948).
- [15] F. O. Goodman and N. Garcia, *Phys. Rev. B* **43**, 4728 (1991).
- [16] D. van Labeke, B. Labani, and C. Girard, *Chem. Phys. Lett.* **162**, 399 (1989).

- [17] F. J. Giessibl and G. Binnig, *Ultramicroscopy* **42-44**, 281 (1992).
- [18] G. Meyer and N. M. Amer, *Appl. Phys. Lett.* **57**, 2089 (1990).
- [19] H. Haefke, E. Meyer, L. Howald, U. Schwarz, G. Gerth, and M. Krohn, *Ultramicroscopy* **42-44**, 290 (1992).
- [20] J. Hu, X.-D. Xiao, D. F. Ogletree, and M. Salmeron, *Science* **268**, 267 (1995).
- [21] J. Hu, X.-D. Xiao, and M. Salmeron, *Appl. Phys. Lett.* **67**, 476 (1995).
- [22] M. Binggeli and C. M. Mate, *J. Vac. Sci. Technol.B* **13**, 1312 (1995), 95.
- [23] N. A. Burnham and R. J. Colton, *J. Vac. Sci. Technol. A* **7**, 2906 (1989).
- [24] B. D. Terris, J. E. Stern, D. Rugar, and H. J. Mamin, *Phys. Rev. Lett.* **63**, 2669 (1989).
- [25] B. D. Terris, J. E. Stern, D. Rugar, and H. J. Mamin, *J. Vac. Sci. Technol.A* **8**, 374 (1990).
- [26] C. Schönenberger and S. F. Alvarado, *Phys. Rev. Lett.* **65**, 3162 (1990).
- [27] Y. Martin and H. K. Wickramasinghe, *Appl. Phys. Lett.* **50**, 1455 (1987).
- [28] C. M. Mate, G. M. McClelland, R. Erlandsson, and S. Chiang, *Phys. Rev. Lett.* **59**, 1942 (1987).
- [29] G. Binnig and D. P. E. Smith, *Rev. Sci. Instrum.* **57**, 1688 (1986).
- [30] M. Tortonese, Ph.D. thesis, Stanford University, 1993.
- [31] M. Tortonese, R. C. Barrett, and R. C. Quate, *Appl. Phys. Lett.* **62**, 834 (1993).
- [32] G. T. Gillies and R. C. Ritter, *Rev. Sci. Instrum.* **64**, 283 (1993).
- [33] G. Meyer and N. M. Amer, *Appl. Phys. Lett.* **53**, 1045 (1988).
- [34] S. Alexander, L. Hellemons, O. Marti, J. Schneir, V. Elings, and P. K. Hansma, *J. Appl. Phys.* **65**, 164 (1989).

- [35] J. Colchero, Ph.D. thesis, Universität Konstanz, 1993.
- [36] O. Marti, J. Colchero, and J. Mlynek, *Nanotechnology* **1**, 141 (1990).
- [37] L. Howald, E. Meyer, R. Lüthi, H. Haefke, R. Overney, H. Rudin, and H.-J. Güntherodt, *Appl. Phys. Lett.* **63**, 117 (1993).
- [38] M. Hipp, Ph.D. thesis, Universität Konstanz, 1994.
- [39] T. Müller, T. Kässer, M. Lambardi, M. Lux-Steiner, O. Marti, J. Mlynek, and G. Krausch, *J. Vac. Sci. Technol. B* **14**, 1296 (1996).
- [40] S. Behler, M. K. Rose, D. F. Ogletree, and M. Salmeron, *Rev. Sci. Instrum.* **68**, 124 (1997).
- [41] J. Wiechers, Ph.D. thesis, Ludwig-Maximilian-Universität München, 1993.
- [42] J. Brugger, R. Buser, and N. de Rooij, *J. Micromech. Microeng.* **2**, 218 (1992).
- [43] T. Itoh and T. Suga, *J. Vac. Sci. Technol. B* **12**, 1581 (1993).
- [44] R. Linnemann, T. Gotszalk, I. W. Rangelow, P. Dumania, and E. Oesterschulze, *J. Vac. Sci. Technol. B* **14**, 856 (1996).
- [45] J. Israelachvili, *Intermolecular and Surface Forces* (Academic Press, London, 1991).
- [46] G. Binnig, C. Gerber, E. Stall, T. R. Albrecht, and C. F. Quate, *Europhys. Lett.* **3**, 1281 (1987).
- [47] F. J. Giessibl, *Jpn. J. Appl. Phys.* **33**, 3726 (1994).
- [48] T. R. Albrecht, P. Grütter, D. Horne, and D. Rugar, *J. Appl. Phys.* **69**, 668 (1991).
- [49] K. Besocke, *Surf. Sci.* **181**, 145 (1987).
- [50] J. Frohn, J. F. Wolf, K. Besocke, and M. Teske, *Rev. Sci. Instr.* **60**, 1200 (1989).
- [51] Q. Dai, R. Vollmer, R. W. Carpick, D. F. Ogletree, and M. Salmeron, *Rev. Sci. Instr.* **66**, 5266 (1995).

- [52] M. Hipp, H. Bielefeldt, J. Colchero, O. Marti, and J. Mlynek, *Ultra-microscopy* **42-44**, 1498 (1992).
- [53] W. T. Thomson, *Theory of Vibrations with Applications* (Allen and Unwin, London and Sydney and Wellington, 1988).
- [54] K. Bromann, Ph.D. thesis, École polytechnique fédérale de Lausanne, 1997.
- [55] R. David, K. Kern, P. Zeppenfeld, and G. Comsa, *Rev. Sci. Instr.* **57**, 2771 (1986).
- [56] A. Hirstein, Ph.D. thesis, École polytechnique fédérale de Lausanne, 1998.
- [57] G. Liu, private communication.
- [58] L. Huang, P. Zeppenfeld, and G. Comsa, *Verhandl. DPG (VI) 31* (Physik-Verlag, Weinheim, 1996).
- [59] W. Burton, N. Cabrera, and F. Frank, *Phil. Trans. R. Soc. A* **243**, 299 (1951).
- [60] R. W. Whitworth, *Adv. Phys.* **24**, 203 (1974).
- [61] S. Amelinckx, *The direct observations of dislocations* (Academic Press, New York and London, 1964).
- [62] S. Amelinckx, *Dislocations in Crystals* (North-Holland Publishing Company, Amsterdam, New York, Oxford, 1979).
- [63] G. A. Bassett, *Phil. Mag. Ser. 3*, 1042 (1958).
- [64] Y. Wei, L. Li, and I. S. T. Tsong, *J. Vac. Sci. Technol.* **13**, 1609 (1995).
- [65] M. Munschau, E. Bauer, and W. Teliëps, *Phil. Mag. A* **61**, 257 (1990).
- [66] R. Bennewitz, Ph.D. thesis, Freie Universität Berlin, 1997.
- [67] H. Shindo, M. Ohashi, O. Tateishi, and A. Seo, *J. Chem. Soc. Faraday Trans.* **93**, 1169 (1997).
- [68] C. Kittel, *Einführung in die Festkörperphysik* (R. Oldenbourg, München and Wien, 1976).
- [69] P. Palmberg, T. Rhodin, and C. Todd, *Appl. Phys. Lett.* **11**, 33 (1967).

- [70] M. Welton-Cook and W. Berndt, *J. Phys. C* **15**, 5691 (1982).
- [71] J.-W. He and P. J. Möller, *Surf. Sci.* **178**, 934 (1986).
- [72] T. Urano, T. Kanaji, and M. Kaburagi, *Surf. Sci.* **134**, 109 (1983).
- [73] H. Nakamatsu, A. Sudo, and S. Kawai, *Surf. Sci.* **194**, 265 (1988).
- [74] K. Rieder, *Surf. Sci.* **118**, 57 (1982).
- [75] M. Mahgerefteh, D. Jung, and D.R.Frankl, *Phys. Rev. B* **39**, 3900 (1989).
- [76] C. Duriez, C. Chapon, C. Henry, and J. Rickard, *Surf. Sci.* **230**, 123 (1990).
- [77] J. Heidberg, E. Kampshoff, M. Kandel, R. Kühnemuth, D. Meine, O. Schönekäs, M. Suhren, and H.Weiss, *React. Kinet. Catal. Lett.* **50**, 123 (1993).
- [78] J. Heidberg and D. Meine, *Ber. Bunsenges. Phys. Chem.* **97**, 211 (1993).
- [79] H. Onishi, C. Egawa, T. Aruga, and Y. Iwasawa, *Surf. Sci.* **191**, 479 (1987).
- [80] R. Echterhoff and E. Knözinger, *Surf. Sci.* **230**, 237 (1990).
- [81] A. Flank, R. Delauney, P. Lagarde, M. Pompa, and J. Jupille, *Phys. Rev. B* **53**, R1737 (1996).
- [82] P. Crozier and M. Gajdardziska-Josifovska, *Ultramicroscopy* **48**, 63 (1993).
- [83] M. Gajdardziska-Josifoskva, P. Crozier, M. McCartney, and J. Cowley, *Surf. Sci.* **284**, 186 (1993).
- [84] R. McCune and P. Wynblatt, *J. Am. Cer. Soc.* **66**, 111 (1983).
- [85] H. Ota, K. Sakai, R. Aoki, N. Ikemiya, and S. Hara, *Surf. Sci.* **357-358**, 150 (1996).
- [86] Y. C. Lee, P. Tong, and P. A. Montano, *Surf. Sci.* **181**, 559 (1987).
- [87] E. Perrot, M. Dayez, A. Humbert, O. Marti, C. Chapon, and C. Henry, *Europhys. Lett.* **26**, 659 (1994).



- [88] R. Sum, H. Lang, and H.-J. Güntherodt, *Physica C* **242**, 174 (1995).
- [89] D. Abriou, F. Creuzet, and J. Jupille, *Surf. Sci.* **352**, 499 (1996).
- [90] S. Perry and P. B. Merrill, *Surf. Sci.* **383**, 268 (1997).
- [91] J. Lowell and A. Rose-Innes, *Advances in Physics* **29**, 947 (1980).
- [92] C. Henry, C. Chapon, C. Duriez, and S. Giorgio, *Surf. Sci.* **253**, 177 (1991).
- [93] C. Henry and M. Meunier, *Mat. Sci. Eng.* **A217/218**, 239 (1996).
- [94] C. Goyhenex, M. Meunier, and C. Henry, *Surf. Sci.* **350**, 103 (1996).
- [95] C. Goyhenex, M. Croci, C. Claeys, and C. Henry, *Surf. Sci.* **352-354**, 475 (1996).
- [96] C. Duriez, C. Henry, and C. Chapon, *Surf. Sci.* **253**, 190 (1991).
- [97] C. Goyhenex, C. Henry, and J. Urban, *Phil. Mag. A* **69**, 1073 (1994).
- [98] M. Meunier and C. Henry, *Surf. Sci.* **307-309**, 514 (1994).
- [99] C. Chapon, C. Henry, and A. Chemam, *Surf. Sci.* **162**, 747 (1985).
- [100] C. Henry, M. Meunier, and S. Morel, *J. Cryst. Growth* **129**, 416 (1993).
- [101] C. Becker and C. Henry, *Surf. Sci.* **352-354**, 457 (1996).
- [102] F. Didier and J. Jupille, *Surf. Sci.* **307-309**, 587 (1994).
- [103] P. Guénard, G. Renaud, and B. Villette, *Physica B* **221**, 205 (1996).
- [104] M.-C. Wu, J. Corneille, C.A., J.-W. He, and D. Goodman, *Chem. Phys. Lett.* **182**, 472 (1991).
- [105] C. Xu, S. Oh, G. Liu, D. Kim, and D. W. Goodman, *J. Vac. Sci. Technol. A* **15**, 1261 (1997).
- [106] R. Jaeger, H. Kuhlbeck, H.-J. Freund, M. Wuttig, W. Hoffmann, R. Franchy, and H. Ibach, *Surf. Sci.* **259**, 235 (1991).
- [107] J. Libuda, F. Winkelmann, M. Bäumer, H.-J. Freund, T. Bertrams, H. Neddermayer, and K. Müller, *Surf. Sci.* **318**, 61 (1994).
- [108] H.-J. Freund, *Angew. Chem. Int. Ed. Engl.* **36**, 452 (1997).

- [109] I. Yudanov, G. Pacchioni, K. Neyman, and N. Rösch, *J. Phys. Chem. B* **101**, 2786 (1997).
- [110] A. Stirling, I. Gunji, A. Endou, Y. Oumi, M. Kubo, and A. Miyamoto, *J. Chem. Soc. Faraday Trans.* **93**, 1175 (1997).
- [111] A. Ferrari and G. Pacchioni, *J. Phys. Chem.* **100**, 9032 (1996).
- [112] Ch.Li, R. Wu, A. Freeman, and C. Fu, *Phys. Rev. B* **48**, 8317 (1993).
- [113] E. Heifets, E. Kotomin, and R. Orlando, *J. Phys. Condens. Matter* **8**, 6577 (1996).
- [114] E. Heifets, Y. Zhukovskii, E. Kotomin, and M. Causa, *Chem. Phys. Lett.* **283**, 395 (1998).
- [115] E. Bauer, *Z. Kristallogr.* **110**, 372 (1958).
- [116] H. Brune, *Surf. Sci. Rep.* **31**, 121 (1998).
- [117] J. Venables, *Phys. Rev. B* **36**, 4153 (1987).
- [118] J. Venables, G. Spiller, and M. Hanbücken, *Rep. Prog. Phys.* **47**, 399 (1984).
- [119] G. Bales and G. Chrzan, *Phys. Rev. B* **50**, 6057 (1994).
- [120] M. Stowell, *Philos. Mag.* **26**, 361 (1972).
- [121] K. Heim, S.T.Coyle, G. Hembree, J. Venables, and M. Scheinfein, *J. Appl. Phys.* **80**, 1161 (1996).
- [122] J. Venables, *Physica A* **239**, 35 (1997).
- [123] N. Waechli, Ph.D. thesis, École polytechnique fédérale de Lausanne, 1997.
- [124] J. Venables (private communication).
- [125] S. Giorgio, C. Henry, C. Chapon, and C. Roucau, *J. Catal.* **148**, 534 (1993).
- [126] M. Morse, *Chem. Rev.* **86**, 1049 (1986).



# Curriculum vitae

## Personal

Name: Alexander Menck  
Date of birth: 29.06.1969 in Bonn, Germany

## Education

1978–1987	Gymnasium at Borghorst and Hilchenbach
1987	Abitur
1987–1988	Compulsory military service
1988–1990	Study of physics at the Universität-Gesamthochschule Siegen
1990–1994	Continuation at the Universität Konstanz
1994	Diploma thesis on “Untersuchung des Reibungsverhaltens an Stufen auf HOPG unter elektrochemischer Potentialkontrolle”
1994–1998	PhD-student at the Ecole Polytechnique Fédérale de Lausanne, Institut de physique Expérimentale, under the supervision of Prof. Dr. K. Kern
1998	PhD-thesis on “Defects and growth processes at ionic and oxide crystal surfaces studied by atomic force microscopy”

